Biophysics of Synthetic Model Cells:
The Membrane Transformative Functions of Essential Proteins and Molecules

By

CHRISTOPHER F. CARNAHAN
DISSERTATION

Submitted in partial satisfaction of the requirements for the degree of

DOCTOR OF PHILOSOPHY

in

Biophysics

in the

OFFICE OF GRADUATE STUDIES

of the

UNIVERSITY OF CALIFORNIA

DAVIS

Approved:

Atul N. Parikh, Chair

John Voss

Matthew Coleman

Committee in Charge

2025

Acknowledgements

Of course, it goes without saying how thankful I am for my advisor, Atul Parikh. Without his guidance, I would not be the researcher I am today, nor would I have achieved that which I have. Atul is, without a doubt, the best academic communicator I have had the pleasure of learning from and has instilled in me an appreciation for investigating the interdisciplinary fields of biomedical engineering and membrane biophysics. And above all, I am thankful for our shared appreciation of espresso-based coffee, and the experiences we shared as a result.

I thank my committee members, Professor Voss and Dr. Coleman, for their guidance and collaboration throughout my doctoral research. I thank them for their contributions to our manuscripts, for their reviews and suggestions, furthering my own intellectual boundaries.

I'd like to express my gratitude to those in my lab, Daniel, Pallavi, Archan, Michael & Roanna for your comradery, shared interests, and for our mutual aid in research and academia. These thanks are extended to those at LLNL – including Dr. Carpenter, Dr. Noy, Dr. He, Dr. Ozturk, and Dr. Wang who treated me as their peer and friend. I sincerely hope we have the opportunity to work together in the future.

Finally, to my wife and son – Rosie and Sage. Thank you for supporting me as I burdened you with such a change in lifestyle over the last four to achieve my own academic interests. I will be forever thankful for having you with me in life. Sage, I hope that someday you will appreciate the time and effort it once took to further the edge of humanities understanding of the world, before the inevitable intellectual offload of exploratory research onto artificial intelligence.

Abstract

Despite being one of the smallest subunits of life, biological cells are immensely complex. Establishing clear causality requires significant effort and energy on the part of researchers, many of whom choose to synthesize models that include only the aspects relevant to a current research question–often referred to as synthetic cells. This thesis aims to present a perspective of the bottom-up approach to biology that utilizes synthetic cells to model biophysical interactions between molecules and membranes. Furthermore, my dissertation seeks to develop methods to reconstitute asymmetries of shapes, structures, molecular composition, and morphologies of minimal synthetic cells. In pursuit of this goal, we utilize and develop methods of giant unilamellar vesicle (GUV) synthesis, as well as image and model the membrane transformative effects of various molecules and proteins. Chapter 1 introduces the reader to the fundamentals of cell membranes, describing the properties of lipids and presenting methods of synthesizing these into GUVs, used as models in membrane biophysical research.

In Chapter 2, we employ GUVs as a model to characterize the membrane transformative effects of a commonly used molecule for drug delivery - methyl-β-cyclodextrin (mβCD). We utilized fluorescence microscopy techniques to image the generation of membrane structures following GUV incubation with mβCD, whose leaflet-specific interactions led to a buildup of a differential stress within the membrane, responsible for the membrane deformations we observe.

In Chapter 3 we examine the membrane remodeling effect of apolipoproteins (A class of protein that makes up a majority of what is commonly referred to as, “good cholesterol”) as they undergo complex, cooperative, and dynamic self-assembly with membrane lipids, producing nascent, discoidal high-density lipoproteins (nHDLs). We reveal the formation of nHDLs from

GUVs is concomitant with significant morphological changes to the vesicle membrane, including transient poration, solute and solvent leakage, and phase separation, before ultimately lysing the cell into a collection of smaller, more stable, daughter cells.

Finally, in Chapter 4, we will discuss the convergence of the previous two chapters, and the future direction of this experimental narrative. This includes the application of mβCD in the synthesis of artificial, tailor-made membrane asymmetry in synthetic cells, followed by the reconstitution of HDL particles that maintain this engineered asymmetry. We will discuss the preliminary experimental results and the practical applications of tailored compositional asymmetry in nanodiscs as a tool for studying integral membrane proteins in their native-like environment.

Table of Contents

Chapter 1

Introduction

1.1 Lipids, Membranes and Biological Cells

Phospholipids, cholesterol and glycolipids are the fundamental building blocks of biological cell membranes, the outermost shell encompassing most living cells. Phospholipids constitute a majority, numbering 5×10^6 lipids per square micron of a cell's membrane. Amphipathic in nature, phospholipids have a polar, phosphate "headgroup" and two hydrophobic, hydrocarbon "tails", typically between 14 and 24 carbons in length (**Fig. 1.1**). These distinct, "head" and, "tail" regimes differ in hydro-activity, rendering a lone phospholipid in an aqueous environment insoluble and energetically unfavorable. As a response, phospholipids often spontaneously organize into a micelle structure – grouping together to minimize surface contact with the water by aligning polar headgroups and burying their hydrophobic tails inward (**Fig. 1.1**). Alternatively, phospholipids will form monolayer sheets in which headgroups are aligned in parallel, and tails sandwiched within another monolayer to form a lipid bilayer (**Fig. 1.2**). While much more favorable, a bilayer structure has shortcomings: the tail groups at the edge of the bilayer sheet

remain exposed, still in contact with the aqueous environment. Solving this problem is a matter of geometry – through a reorganization of the bilayer mesophase into an enclosed sphere. This stable structure, known as a vesicle, is the basis of all biological cell membranes (**Fig. 1.2**).

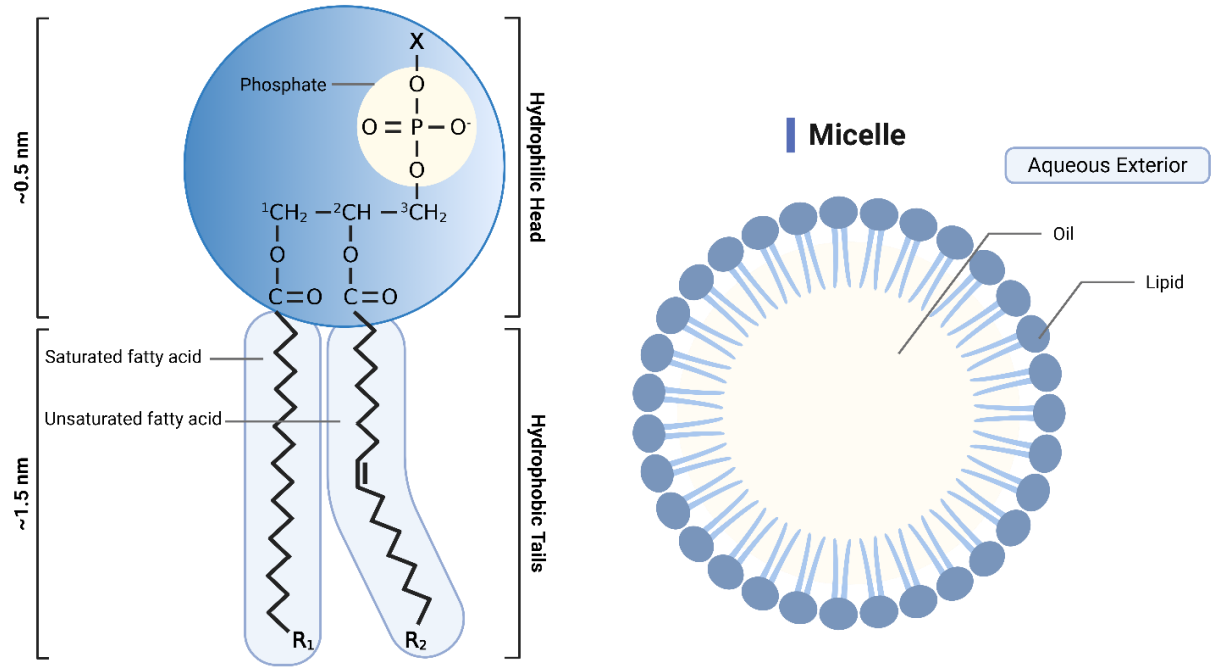

***Figure 1.1**: Diagram of the chemical structure of the phospholipid 1-Stearoyl-2-Oleoyl-sn-glycero3-PhosphoCholine depicting the phosphate headgroup, saturated, and unsaturated fatty acid chains. The approximate length and amphipathic aspects of the phospholipid are indicated. Diagram of phospholipids organized into a micelle structure in an aqueous environment enclosing an oily solution. Created in BioRender. Carnahan, C. (2025) https://BioRender.com/dborwrf*

In addition to enclosing the cell, the membranes of eukaryotic cells are semi-permeable and allow for the selective diffusion of water, oxygen, or other small polar molecules. This selective behavior is what separates "inside" from "outside" of living cells – facilitating cell recognition, communication, and transport while maintaining a charge gradient by selective passage through specific ion transport proteins from within the membrane. In addition to ion transport, membrane

proteins have a vast range of functionality, from mediating cell-cell interactions to maintaining membrane shape and composition; These proteins are classified into two distinct classes: peripheral and integral membrane proteins. Peripheral membrane proteins associate with the cell membrane but are not composed of the necessary structure to fully integrate with the membrane. These proteins assist in both support and communication through membrane remodeling signal transfer to the cell. In contrast, integral proteins are permanently embedded in the cell membrane, often spanning their entire width or extending into the hydrophobic core from one side. Integral proteins perform a wide range of functionality for the cell including transport of cargo across the membrane, catalyzing enzymatic activity, or adhesion between cells or the extracellular matrix.

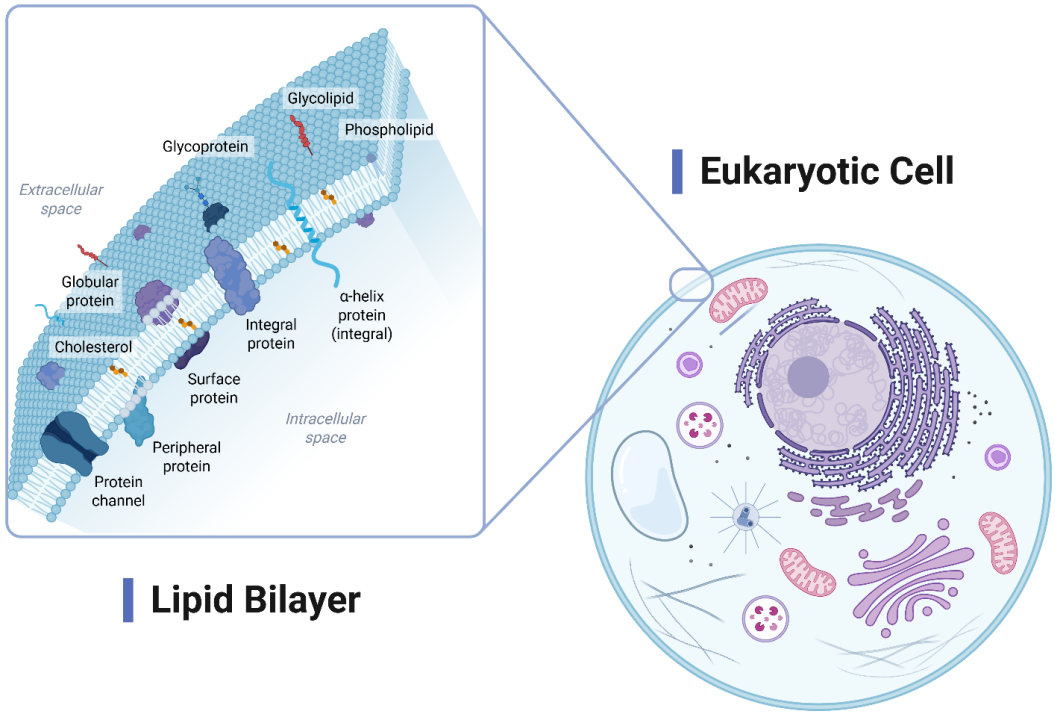

Figure 1.2*: Diagram of a eukaryotic cell with inset depicting a typical component of a cell's plasma membrane. A collection of membrane-related components and proteins are shown in their typical location within a membrane bilayer. Created in BioRender. Carnahan, C. (2025) https://BioRender.com/gan1lja.*

Cell membranes are complex, crowded (~50% protein by mass), and still a highly active area of biophysical research. Additionally, the outermost plasma membrane is far from the only membrane of the cell. Subcellular structures – organelles – within eukaryotes are often membrane-bound, with varying functional differences. Notably, the interconnected, membrane-enclosed tubules within the endoplasmic reticulum that form a continuous network involved in several physiological processes such as lipid metabolism, calcium dynamics, and protein-lipid or lipid-lipid signal transductions (*1-4*).

Whether acting as a barrier or a transport network, lipid bilayers are effectively a two-dimensional fluid – freely rotating and diffusing laterally (5) – highly dependent upon temperature and lipid composition. For a membrane composed of lipids with substantial difference in lengths of their fatty acid, hydrocarbon chains will experience a phenomenon called hydrophobic mismatch. Hydrophobic mismatch occurs when a lipid species with longer hydrophobic chains will have some exposure to the surrounding, aqueous environment, incurring an energetic cost. As a result, lipids reorganize by forming aggregations of similar lipid-types, reducing the overall interfacial aqueous contact (6). Lipids aggregate into domains of liquid-liquid phase separated regions. Several membrane characteristics are known to induce such phase domains within lipid membranes, such as lipid saturation (an unsaturated chain will kink, taking up more physical space), lipid charge, or presence of sterols. Each of these characteristics affect a membranes energetic boundary in the phase space, quantified by an intrinsic measurement - characteristic melting temperature (Tm).

Each lipid's characteristic melting temperature is a measurement of the energy required to reach a phase transition. Temperature is the driving force necessary to induce phase separation from a mixed membrane, for example: A membrane composed of two distinct lipid species – one with a high Tm and the other with low Tm – will exist in a homogeneous, mixed state at a temperature above the melting temperature of the higher Tm lipid, whereas in the case when temperature falls between the Tm of the two lipid species, the membrane will demix and exist in a 2-phase state (6). In this state, the temperature as fallen past the transition point for the higher Tm lipid, which now exists in a gel-like state, while the other remains melted. Adjustments to the lipid characteristics, such as chain length, charge, or sterol presence, that increase the difference in melting temperature between any two lipid species increases the temperature range at which phase emergence occurs.

1.2 Synthetic Membranes as Model Cells

Despite being one of the smallest subunits of life, cells are immensely complex. The traditional depiction of a eukaryotic cell typically shown in biology textbooks, while informative, does not fully capture the true chaos that takes place within. Figure 3 depicts an artist's rendering of what the crowded nature of a cell realistically might look like. It is for this reason that many challenges exist in cell research – an arduous process must take place to establish clear cause and effect.

To eliminate redundancy, increase clarity, and overall simplify the system, many researchers opt to synthesize artificial cells – models containing purely aspects relevant to a current research question. Notably, giant unilamellar vesicles (GUV) are commonly used platform modeling a compartment bound by a lipid bilayer. This is the simplest, and most faithful representation of

cellular membranes. Typically, between 10-20 μm in diameter (resembling our own cells), GUVs are an ideal model for light microscopy, highly compatible with membrane-associated or integral proteins, capable of encapsulating relevant a wide range of solvent or solutes and can be produced in high volume, making GUVs popular for large sample screening. Furthermore, these micro-compartments can be synthesized from a desired lipid mixture to produce model membranes for studies interested in lipid-dependent behavior in protein-membrane interactions, cell fusion (8) or transport processes. In all applications, synthetic cells are bottom-up approach to biology (7), made to mimic essential functions with a goal to build cell-like objects from individual components.

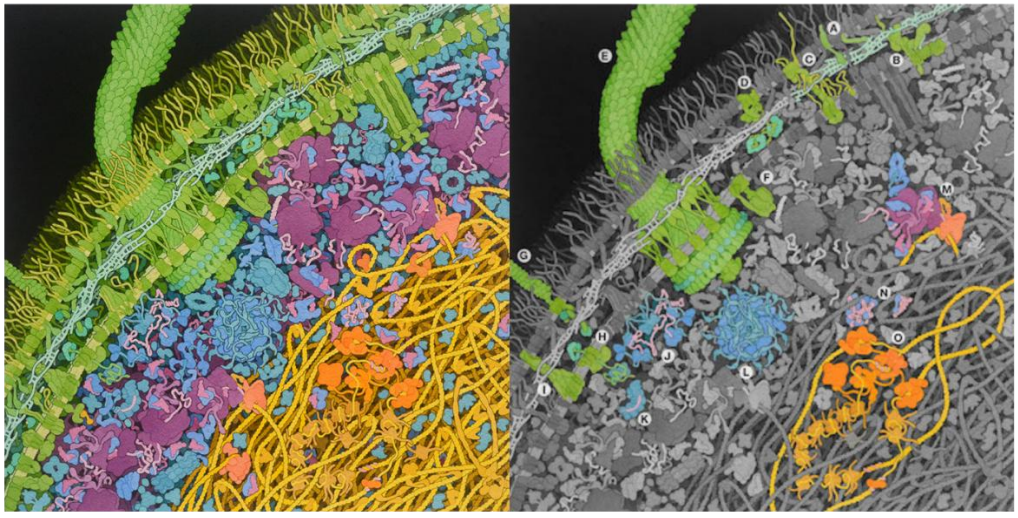

Figure 1.3*: Painting of a cross-section through an Escherichia coli cell. The right panel labels the following: A) Lipoprotein; B) Protein complex, including penicillin-binding proteins; C) The lipopolysaccharide transport system; D) Protein chaperone system for outer membrane folding proteins (BAM system); E) Flagellum and flagellar motor; F) ATP synthase; G) Fimbria and fimbrial usher; H) Secretory translocon, being assisted by chaperones; I) AcrAB/ToIC bacterial efflux pump; J) Degradosome, protein complex that degrades obsolete RNA; K) Cascade and CRISPR; L) Pyruvate dyhydrogenase complex; M) Expressome, that helps to coordinate binding of tRNA and elongation factors; N) sRNA with associated proteins; O) Replisome including several DNA polymerases. Figure reproduced from Ref. (9).*

Reproducing biological function with synthetic cells is becoming more advanced. The bottom-up approach to biology has revealed fundamental principles of how cells are built and function, as well as revealing mechanisms behind beginning-of-life formation. Currently, this bottom-up approach has yet to fully recreate synthetic cellular functionality, however, recent advancements in the field showcase emergence of biohybrids – the junction of engineered cells with synthetic cell subsystems (*10*). This conjunction of bottom-up and top-down approaches may also offer unique insights and practical applications to the field of biomedical research. In essence, synthetic vesicles function as a platform that enable visual characterization of biophysical interactions that serve as a means to deepen our understanding of biology, at a fundamental level, while also providing practical applications in the development of drug delivery techniques, vaccine carriers, carbon fixation (*11*), and more therapeutic applications (*12*).

1.3 Preparation of Giant Unilamellar Vesicles

Vesicular membrane synthesis has many well-established methods, with complexity ranging from simple freeze-thaw cycles, exploiting free-energy minima, to cutting-edge microfluidic approaches curated for tailor-made, leaflet-specific composition. With such a wide array of synthetic vesicle-related disciplines, methods and practices to preparation are tailored to each one's needs. The following techniques were utilized, adapted, or established during my doctoral research.

1.3.1 Electroformation

GUV preparation via electroformation is a relatively approachable technique (*13*, *14*). A hydrated lipid cake spontaneously swells, forming single-bilayer (unilamellar) vesicles in the presence of an electric field (**Fig.**

1.4). This effect depends heavily on the lipid composition, temperature, osmolarity and AC parameters. GUVs prepared using electroformation result in a large population of polydisperse liposomes, ranging in diameter between 1-100 μm. The high throughput of vesicle production is ideal for large-sample assay studies; however, this preparation is generally limited to non-saline solutions as a solvent with high ionic strength interferes with the separation of lamellae and increases the force required to swell the lipid film (*15*).

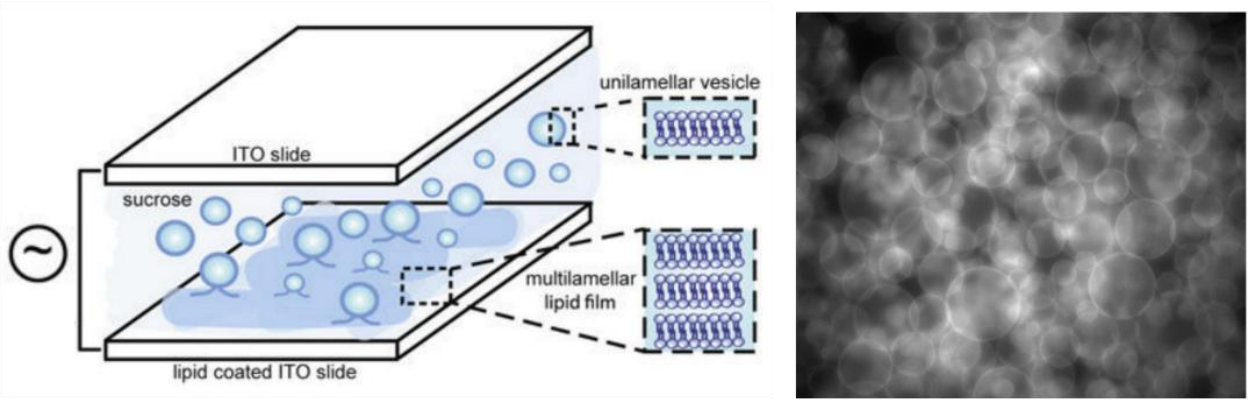

***Figure 1.4**: **Left:** Diagram of GUV synthesis through electroformation. An AC current is passed between two, conductive ITO-slides with a hydrated lipid cake coating (16). **Right:** A widefield microscopy image of GUVs taken immediately following electroformation.*

It is possible be overcome this limitation by utilizing addition plasma coated ITO electrodes and substantial adjustments to function generator parameters (*17*), however, vesicle diameter seemingly varies with increase in salt concentration, while increasing with temperature. Additionally, studies dependent on vesicle size, electroformation can be beneficial for observing how varying radius of a GUV affects an interaction, or detrimental in studies requiring consistency. Furthermore, integral protein reconstitution into GUVs through electroformation is possible, relying on protein-lipid interactions. GUVs production via electroformation can be used to address a wide range of fundamental questions regarding membrane special organization as well as a versatile tool for studying a bottom-up approach to cell biology.

1.3.2 Octanol-Assisted Liposome Assembly (OLA)

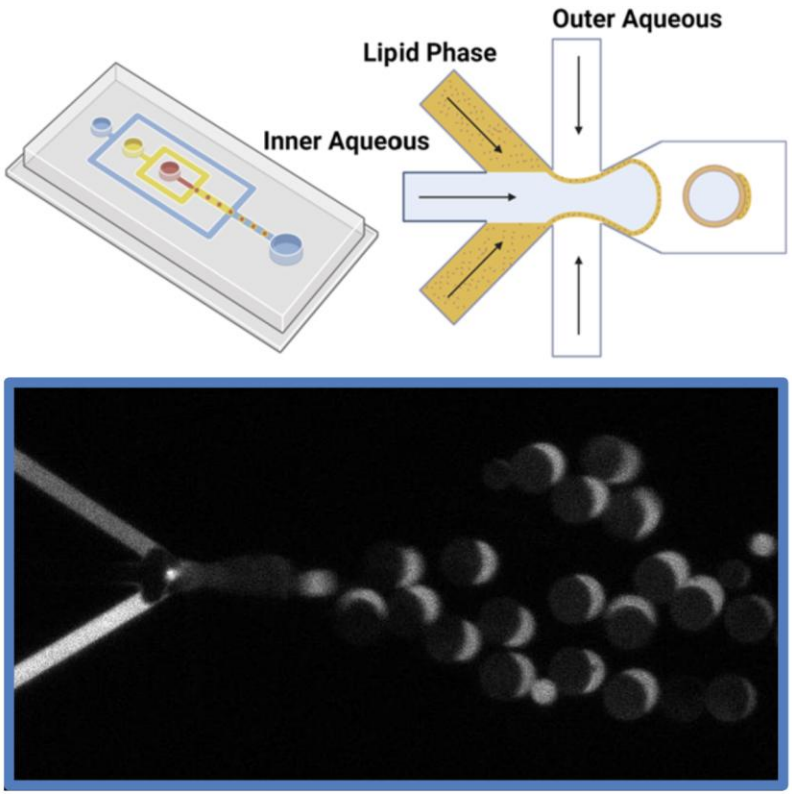

***Figure 1.5**: **Top:** Depicts a diagram of a double-emulsion microfluidic chip and the junction in which liposomes are produced. **Bottom:** A fluorescence brightfield image of the OLA technique rapidly producing liposomes. The labeled lipids are seen within the middle, oil-phase and a pocket of excess oil remains on the formed vesicles. This excess pocket spontaneously detaches with shear force from a viscous, outer aqueous phase or when heat is applied to the system.*

OLA is a recent advancement in microfluidic technology developed to produce giant unilamellar vesicles (*18*). Sometimes compared to bubble-blowing, an inner aqueous phase is encapsulated by a lipid-carrying 1-octanol phase, forming a single emulsion, water in oil droplet. The outermost oil phase is pinched off by a third channel carrying an exterior aqueous solution – forming a double emulsion of water in oil in water droplets (**Fig. 1.5**). This advanced technique requires high-precision pressure control along with cutting-

edge microfluidic chip manufacturing capabilities, due to the requirement of a partial polyvinyl alcohol coating in the outermost and exit channels. As a benefit, these vesicles are remarkably polydisperse (radii dependent on pressure and chip variations) with excellent encapsulation efficiency of the inner aqueous phase.

This technique has been utilized by researchers to analyze complex encapsulation studies. I have implemented this method of GUV production into our research group, which has published research utilizing OLA to precisely encapsulate polymer components to induce multiple liquid-liquid phase separations (LLPS) events (associative and segregative) in the cytoplasmic space of a synthetic vesicle (19), mimicking membraneless organelles and how interplay between multiple LLPS might affect one another.

1.3.3 Rehydration of Engineered Lipid Nano constructs

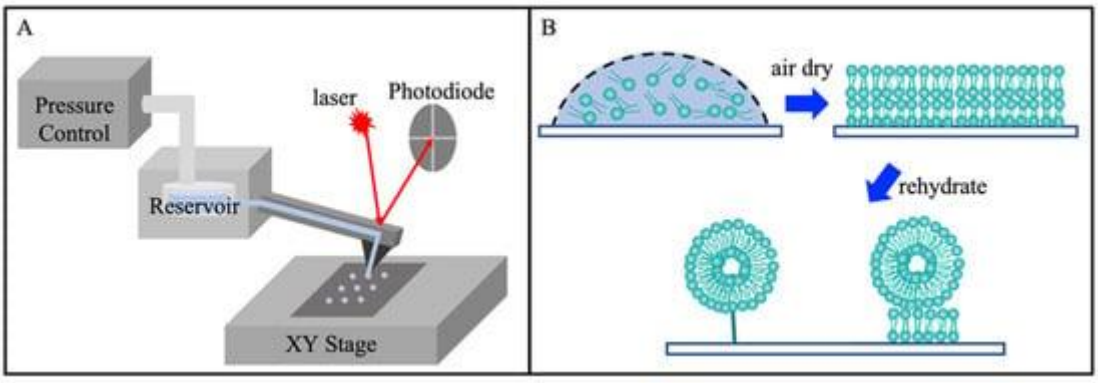

***Figure 1.6**: **A)** Schematic diagram of an AFM combined with a microfluidic delivery. **B)** Schematic diagram illustrating the key steps, following the delivery in (A), in forming liposomes via the rehydration of lipid nanostructures. Reproduced with permission from Ref. (20).*

An emerging concept in the preparation of giant unilamellar vesicles, rehydration of lipid constructs produced with a microfluidic delivery probe is a method of liposome production established through a collaborative effort between our research group and the Gang-Yu Liu lab

([20](#)). This particular technique generates GUVs that often remain adhered to the substrate – anchored and easily manipulatable for subsequent experimentations. Furthermore, liposome diameter and hierarchical structure are tunable, allowing for the regulation of lipid construct dimensions and compositions – variables benefiting numerous applications, such as proto-cell development, multiplexed bio-composite materials, and the engineering of local bio-environments.

1.4 The Role and Importance of Membrane Deformation

Possibly the most critical function of the cell membrane is the ability to deform and divide, allowing cells to internalize or externalize substances within a membrane-bound vesicle. In addition to endo- and exocytosis, mitosis and meiosis are essential functions for cell division, facilitating an organism's development and repair. The cell has several extrinsic mechanisms to apply a force onto a membrane as a means to deform, most notably the cytoskeletal scaffold structure that forms a network around the cell. Actin networks or microtubule motors physically pull on the membrane to form tubules or buds ([21](#), [22](#)), participating in the formation of cell-surface microvilli through the extension of the actin filaments against the plasma membrane.

Osmotic pressure (Π) is a measurement of water molecules passing through the semi-permeable plasma membrane because of an imbalance of solute concentration between the space separated by the membrane. Often, this results in a substantial change in membrane tension and curvature while playing a variety of critical roles in the physiological functions of the cell ([23](#), [24](#)). An osmotically deflated GUV generates substantial membrane deformations ([25](#)), while osmotically inflating a GUV can induce enough membrane tension to both lyse the membrane to form transient

pores and stretch the membrane enough to energetically favor the appearance of phase domains (26). A critical function of biological cells is to maintain osmotic control through the regulation of electrolytes through ion channels, pumps or the synthesis of osmolytes. Bacteria have been shown to utilize an osmotic shock in the process of forming the cell envelope (27), showing just how powerful this simple concept of membrane deformation can be in biology.

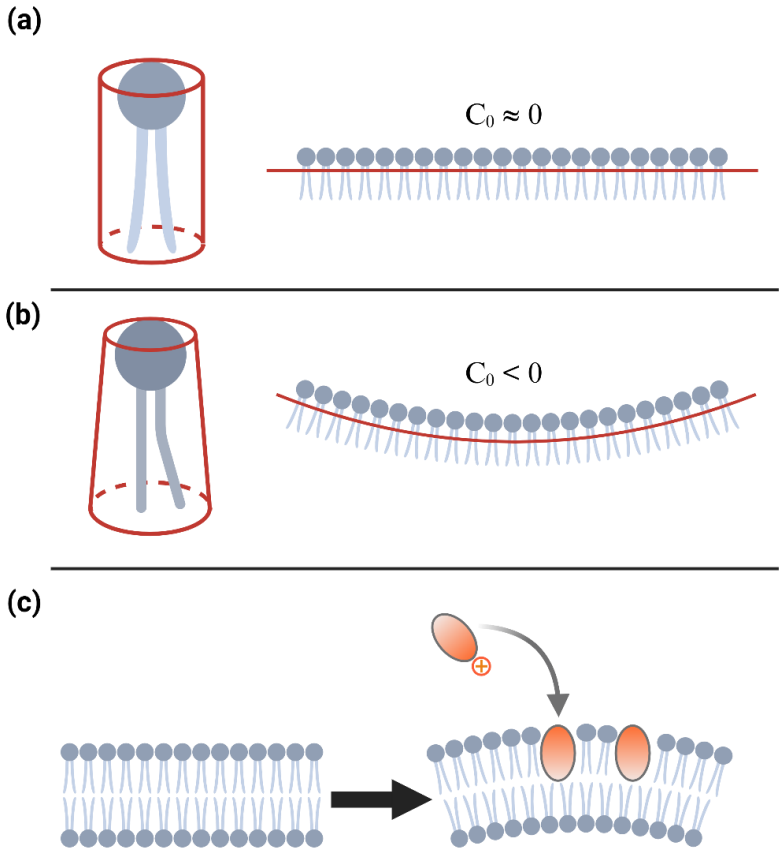

***Figure 1.7**: Diagram depicting differences in lipid geometry resulting in the generation of spontaneous curvature, including **a)** cylindrically shaped lipids with resting spontaneous curvature ($C_0 \approx 0$), and **b)** conically shaped lipids with negative spontaneous curvature ($C_0 < 0$). **(c)** Diagram of tensionless membrane undergoing shape deformation and positive curvature generation upon insertion of amphipathic protein into the outer leaflet of the membrane, causing area mismatch.*

The formation process of membrane deformation from organized lipid mesophases, such as planar or spherical membranes, often is initiated by an external and cooperative protein-mediated interaction (28). Many proteins have this capability, such as BAR domains (28, 29), GTPases (30), annexin B12, α-synuclein (31), clathrin (32), endophilin (33) and amphithecium (34), which have shown to generate membrane structures or tubules from liposomes both *in vivo* and *in vitro*. Bar domains drive curvature through polymerization with an intrinsic curvature to form either spheres or spirals, while amphipathic peptides such as α-synuclein partition into the membrane–water interface, acting as a wedge altering the packing and organization of the lipids within the membrane (35, 36); and induce an area mismatch (37) between the two individual leaflets that make up the phospholipid bilayer. These mechanical deformations synergistically serve to reduce the energy cost for the creation of curvature generation (38) and thus promote membrane remodeling.

Lipid-specific dynamics play an important role in generating membrane curvature (39, 40). Lipids have an intrinsic geometry (spontaneous curvature) that favor membrane curvature. Conical shaped lipids, such as phosphatidylethanolamine lipids, adopt a wedge-like geometry capable of inducing an overall membrane deformation when asymmetrically present in one leaflet of the bilayer. In general, membrane asymmetry is a driver of membrane curvature – in both a difference in lipid species (as in the case of the aforementioned geometrical differences) or lipid density between the leaflets of a bilayer. In fact, asymmetry in leaflet compression – despite an overall tensionless membrane – poses unique thermodynamic challenges, and is referred to as *differential stress* (41, 42). A typically hidden variable – as there is no easy method to experimentally measure individual leaflet tension – differential tension is regulated by the cell through enzymatic trans-bilayer lipid transport (43) (e.g., translocases). These integral proteins must overcome a significant

energy barrier (nearly 80 kJ/mol) to maintain an energetically unfavorable membrane asymmetry. *In vitro* differential stress can be spontaneously induced in vesicular membranes through leaflet-specific molecules, such as cyclodextrin lipid exchange – discussed in detail in Chapter 2.

Understanding the mechanisms of generating membrane deformation is a crucial aspect within the field of cell biology. Membrane deforming capabilities of diseases that penetrate our cell's defenses rely on complex protein-membrane interactions, and therefore, in order to develop effective therapeutics to combat them, humanities collective understanding must keep evolving.

1.5 A Case Study of Osmotic & Laplace Pressures at Equilibrium

The following derivation describes the complementary relationship, in a vesicular membrane, between the removal of lipid, Laplace Pressure, shrinkage of the GUV, increase in local concentration and the osmotic influx of water.

What is the equilibrium GUV radius as a function of % decrease in lipids from the membrane? This is the main question, modeled around the opposing pressures acting on the membrane, Laplace pressure and Osmotic pressure.

$$\Delta P_L = \Delta P_O \tag{1.1}$$

Where Laplace pressure is defined by,

$$\Delta P_L(r) = \frac{2\sigma}{r} \tag{1.2}$$

Here σ is the lateral membrane tension and r is the radius of the vesicle. Membrane tension can be described as a partial derivative of the membrane elastic energy, $E(R,r)$, with respect to surface area, A (44):

$$\sigma = \frac{\delta E(R,r)}{\delta A} \tag{1.3}$$

Therefore,

$$\frac{\delta E(R,r)}{\delta A} = \frac{\delta}{\delta A}\left(\frac{1}{2A_0}k(A-A_0)^2\right) = \frac{k(A-A_0)}{A_0} \tag{1.4}$$

Where k is the area expansion modulus (~241.3 dyn/cm for DOPC Lipids (45)). Here, $\frac{(A-A_0)}{A_0}$ is a unitless term, describing the difference in membrane surface area between the initial and final membrane conditions. Reddy Et. al, utilized this function to describe the relationship between lipid density and membrane tension. They replace $\frac{(A-A_0)}{A_0}$ with area per lipid $\left(\frac{A}{L}\right)$, to find the % change in area per lipid, per dyn/cm increase in lateral membrane tension, (~0.45%) resulting in the expansion modulus of 241.3 ± 24. With this precedent, we also replace $\frac{(A-A_0)}{A_0}$ with area per lipid $\left(\frac{A}{L}\right)$ to rewrite lateral membrane tension as a function of r (Note: $\frac{A_0}{L_0}$ is not "equilibrium area/lipid", just the **initial** area per lipid):

$$\sigma = \frac{k\left(\frac{4\pi r^2}{L} - \frac{A_0}{L_0}\right)}{\frac{A_0}{L_0}} = k\left(\frac{4\pi r^2 L_0}{LA_0} - 1\right) \tag{1.5}$$

Therefore,

$$\Delta P_L(r) = \frac{2k}{r}\left(\frac{4\pi r^2 L_0}{LA_0} - 1\right) \tag{1.6}$$

Now, Osmotic pressure can be written as:

$$\Delta P_O(r) = RT\Delta C(r) \tag{1.7}$$

Where $\Delta C(r)$ is difference in concentration between the inside of the GUV, and the surrounding bath. The GUV concentration can be further written as a function of r:

$$\Delta C(r) = (C_{in} - C_{out}) = \left(\frac{m}{1e^{-3}\left(\frac{4}{3}\pi r^3\right)} - C\right) \tag{1.8}$$

Where m is the moles of solute encapsulated within the vesicle and C is the concentration of the surrounding bath. Now, when ΔP_L and ΔP_O equated:

$$\frac{2k}{r}\left(\frac{4\pi r^2 L_0}{LA_0} - 1\right) = \left(\frac{m}{1e^{-3}\left(\frac{4}{3}\pi r^3\right)} - C\right) \tag{1.9}$$

Solving for L:

$$L(r) = \frac{8\pi r k L_0}{A_0\left(RT\left(\frac{m}{1e^{-3}(\frac{4}{3}\pi r^3)} - C\right) + \frac{2k}{r}\right)}$$

And,

$$L(r) = L_0 + \Delta L(r)$$

Reorganized as,

$$\Delta L(r) = L_0 \left(\frac{8\pi r k}{A_0 \left(RT\Delta C(r) + \frac{2k}{r} \right)} - 1 \right) \tag{1.10}$$

Where Lo is the initial lipid count, k is the expansion modulus for DOPC lipids, Ao is the initial GUV surface area, and ΔC(r) is the change in concentration as a function of radius. **Figure 1.8** visualizes plotting this function with the initial conditions, $r_0 = 10\mu m, T = 298°k, C = 100mM \; and \; k = 241.3 \; dyn/cm$.

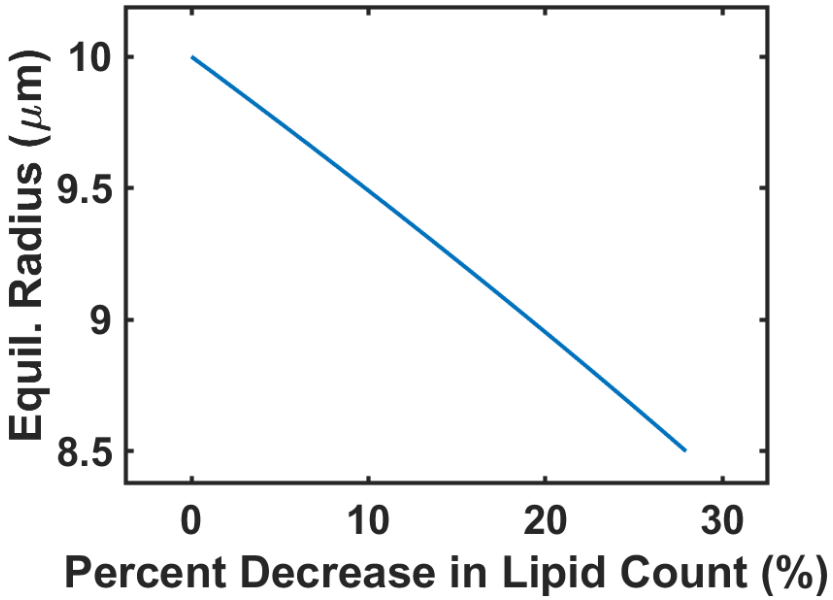

Figure 1.8*: Graph of the theoretical relationship between the reduction in lipid and vesicle radius when osmotic and Laplace pressures are at equilibrium for the initial conditions of r = 10μm, T = 298°k, C = 100 mM and k = 241.3 dyn/cm.*

Each point on **Figure 1.8** shows GUV radius as a function of % decrease in lipids, when Laplace pressure and Osmotic pressure are at equilibrium. For example, a 10% decrease in lipid (Far more than would be expected to occur under normal circumstances), would result in a change of equilibrium GUV radius from 10 to ~9.5. Recall that poration occurs radially when $\Delta r/r > 8.6 \pm 0.2 \times 10\text{-}3$ (*46*), or a change of radius from 10 to 9.9 um.

1.6 Protein-Membrane Interactions in Synthetic Cells

Now that we have established the structure and function of lipid membranes, as well as the importance of synthetic biology, we are now equipped with the understanding necessary to appreciate the impact of the subsequent chapters of this thesis, outlined here:

In Chapter 2, we characterize and quantify the previously unappreciated, membrane remodeling ability of a commonly used molecule for therapeutic applications - methyl-β-cyclodextrin (mβCD). Here, we employ advanced fluorescence microscopy techniques to observe the formation of phase-specific tubule generation, quantify changes in lipid fluidity, and model structural parameters of the regional deformations key to unveiling the processes behind their formation. The ability of mβCD to selectively interact with- and remove lipids and sterols from specific domains within a single leaflet of a vesicular membrane are what enable it to induce a differential stress on the membrane. A clear understanding of the conditions under which this molecule is capable of gross membrane remodeling is critical to mβCD's safe and continued usage as a therapeutic tool for drug delivery.

In Chapter 3, we examine how the complex membrane deformative effects of Apolipoproteins. Apolipoproteins make up ~70% of the protein mass of high-density lipoprotein (HDL), responsible for reverse cholesterol transport and commonly referred to as, “good cholesterol”. Apolipoproteins undergo complex, cooperative, and dynamic self-assembly with membrane lipids, producing nascent, discoidal HDL. Despite its importance, the kinetic pathways of assembly remain incompletely understood. Here, we monitor the dynamics of Apolipoprotein-membrane interactions through real-time monitoring of the morphological changes that occur once incubated with synthetic cell models. We reveal the formation of discoidal HDL particles while remodeling the parent membrane in discrete stages involving membrane poration, solute leakage, vesiculation and lipid-lipid phase separation. These findings depict key steps in the protein-lipid interactions, which guide the assembly of mesoscopic reconstituted lipoproteins and nanodiscs.

Finally, in Chapter 4, we will discuss the convergence of the previous chapters and the future direction of this experimental narrative. This includes the application of mβCD in the synthesis of artificial, tailor-made membrane asymmetry in synthetic cells, followed by the reconstitution of HDL particles that maintain this engineered asymmetry. We will discuss the preliminary experimental results and the practical applications of tailored compositional asymmetry in nanodiscs as a tool for studying integral membrane proteins in their native-like environment.

Chapter 2

Cyclodextrin lipid exchange induces phase specific membrane remodeling

Christopher F. Carnahan[1], Atul N. Parikh[1,2]

1. Biophysics Graduate Group, University of California, Davis, CA
2. Department of Biomedical Engineering, University of California, Davis, CA

2.1 Abstract

Cyclodextrins (CDs) are a class of cyclic oligosaccharide composed of D-glucose units forming a non-polar cavity that acts to house suitable molecules – including lipids and sterols. CD integration into pharmaceutical applications has already shown promise, utilizing this molecule as a vehicle for drug delivery, as biosensors, or a mechanism for material coating. While already commercially available in 20-30 therapeutic oral products, there still exist some concerns regarding their safety – as our understanding of potential side-effects, *in vitro*, remains incomplete. Here, our fluorescence microscopy images reveal that, under certain circumstances, methyl-β-cyclodextrin (mβCD) interaction with minimal giant unilamellar vesicles (GUVs) result in significant tubule generation, lipid phase separation, and membrane domain specific remodeling that occur due to mBCD's leaflet-specific behavior. This study quantifies and characterizes the complex interactions between mβCD and membranes of closed topologies, critical for safe CD utilization as a therapeutic or as a vehicle for drug delivery.

2.2 Introduction

Cyclodextrins (CDs) are a class of cyclic oligosaccharides composed of D-glucose units bound by *α-1,4*-glucosidic bonds. These subunits form a water-soluble ring, within which exists a slightly non-polar cavity, an unfavorable environment for the surrounding water molecules. This cavity readily and spontaneously acts to house capable molecules, such as sterols or lipids – a unique mechanism utilized for some pharmaceutical applications, including as a vehicle for drug delivery, material coating, or as bio-sensors (47-49). CD nomenclature is dictated by the number of glucopyranose sugars, commonly hexamers, heptamers or octamers identified as α-, β-, and γ-CD,

respectively (50). Modifications to the inner aliphatic chain, such as the substitution of a methylene group, influence the properties of cargo molecule association (51, 52). Methyl-β-cyclodextrin (mβCD), and more recently methyl-α-cyclodextrin (mαCD), have a large body of literature reporting their ability to readily exchange lipid and sterols from organized mesophases (i.e. supported bilayers and vesicles). This exchange is limited to the leaflet in direct contact with CD and is relatively low for lipids with long acyl chains (53, 54). Despite these caveats, preparation of compositional membrane asymmetry utilizing mβCD and mαCD is readily achievable (55-59).

Pharmaceutical applications of CDs are widespread, forming drug-CD complexes (60) capable of enhancing drug solubility (60), stability (61) and bioavailability (62). Most notably, CDs have been utilized as a vehicle for drug delivery, commercially used worldwide in 20-30 oral products, currently (63). Clearly, the beneficial applications of CDs are already being implemented, however, there still exist some concerns regarding their safety (64). While modern advances have helped to stave off many of these concerns, there still exist unknown effects of CD usage, including reports of nephrotoxicity in some studies, particularly when administered in high doses (65). Both mβCD and mαCD have shown to interact with, and even modulate, the composition of plasma membranes. Changing membrane composition has further potential implications – mechanistically through the generation of spontaneous curvature or compositionally as a shift in phase energetics. The interaction between membrane and protein relies on a lipid-mediated curvature that yields attraction or repulsion of membrane proteins (66-69). Some integral proteins critical to biological function have altered or reduced efficacy in highly curved membranes, such as ATG3 promoting lipidation of GL1 (70), reduced activity of human Atg8 (71), and positive curvature inhibition of SNARE-mediated membrane fusion (72). Knowing that CD interaction occurs in a single leaflet

raises the question: Can CDs initiate a spontaneous curvature in the plasma membrane, potentially capable of interfering with the cell's natural protein-membrane interaction?

Biological membranes are dynamic, complex and compositionally diverse. Advances in biotechnological and biomedical applications rely on the understanding between molecules and membranes, particularly in models of organized lipid mesophases mimicking our own eukaryotic cells. Intrinsic to the liquid nature of the plasma membrane, the role of deformation and curvature is vitally important to membrane-protein interactions. Curved structures, formed from the membrane, are broadly classified into buds, pearled structures and tubules (*73*, *74*). The formation process of these structures from organized lipid mesophases, such as planar or spherical membranes, can be initiated by a cooperative protein-mediated interaction (*28*). Many proteins have this capability, such as BAR domains (*28*, *29*), GTPases (*30*), annexin B12, α-synuclein (*31*), clathrin (*32*), endophilin (*33*) and amphithecia (*34*), which have shown to generate membrane structures or tubules from liposomes *in vitro*. Membrane deformation and structure generation – similar to observations of the above proteins – is unexpected as a result of mβCD activity.

In the work reported here, we show that that mβCD has the capability to produce membrane deformation by inducing a spontaneous curvature in topologically enclosed membranes (GUVs). We monitor and characterize membrane structures generated in this process, providing a basis for the conditions under which mβCD produces nanotubules. Understanding these potential effects of CD-membrane interaction is key to its safe usage as a therapeutic, as a vehicle for drug delivery and its effective usage in the production biosensors or compositional membrane asymmetry.

2.3 Results

This study aims to quantify the membrane structural effect of mβCD on a suspension of protein- and cytosol-free model phospholipid membranes of closed topologies i.e., giant unilamellar vesicles (GUVs, typically 15-30 μm diameter) (*13*). We synthesize membranes of both single- and multicomponent compositions. Our single component GUVs consist of the common, unsaturated phospholipid, 1-palmitoyl 2-oleoyl-*sn*-1-glycero-3-phosphocholine (POPC). Multicomponent GUVs are reconstituted including cholesterol, POPC, and egg-sphingomyelin (SM) in either equimolar (1:1:1) or cholesterol poor (2:2:1) ratios. This mixture of lipids and cholesterol are known to form either a uniform single phase or exhibit phase separation based on composition ratio and temperature (*75*). Cholesterol poor GUVs (2:2:1) are characterized by co-existing lipid domains: a dense phase enriched in cholesterol and primarily composed of SM, designated as the liquid-ordered (L_o) phase, and a domain composed of POPC and poor in cholesterol, the liquid-disordered (L_d) phase. We incubate multi-component GUVs with a mixture mβCD and cholesterol, in a ~6:1 ratio – cholesterol-loaded cyclodextrin (CLC) – typically used with cholesterol containing acceptor vesicles in the preparation of membrane asymmetry (*56*, *57*). The addition of cholesterol into CD solution promotes interaction with cholesterol containing GUVs and produce observably similar result seen with POPC GUVs and pure mβCD.

Utilizing fluorescence microscopy, we distinguish the complimentary regions of POPC:SM:Chol GUVs with the inclusion of small concentrations of the phase sensitive probes, N-lissamine rhodamine dioleoyl phosphatidylethanolamine (Rho-DOPE, Ex/Em, 560/583 nm) (*76*) and N-7-Nitrobenz-2-Oxa-1,3-Diazol-4-yl-1,2-Dihexadecanoyl-sn-Glycero-3-Phosphoethanolamine, Tri ethyl ammonium Salt (NBD-PE, Ex/Em 463/536nm) which preferentially associate with the L_d

and L_o domains, respectively. At equimolar composition (1:1:1) and room temperature (20-22°C), the absence of phase domain formation at optical length scales is predicted by the phase diagram (75) but does not rule out existence of nanoscale domains (77). As expected, these GUVs appear optically homogenous when encapsulating 100 mM sucrose in a medium of 100 mM glucose. These GUVs model our own eukaryotic cells in size and membrane composition, acting as a basis for interactions one might expect when utilizing mβCD for pharmaceutical applications. We monitor these interactions using spinning disc confocal and wide-field fluorescence microscopy and document the ensuing morphological and topological transformations, below.

2.3.1 mβCD interaction produces inward tubules in POPC GUVs

Introducing small concentrations (0.5-5 mM) of methyl-*β*-cyclodextrin (mβCD) to a collection of giant unilamellar vesicles (GUVs) composed of POPC results in a gross change in the membrane's structure. **Figure 2.1** (**Supplementary Video 2.1**) depicts these structural changes after the addition of 1 mM mβCD. The GUV initially appears optically uniform and continuous across the equatorial plane with a clear interior. Around 2 minutes following the addition of mβCD, small structures begin to appear within the lumen of the vesicle. In the following minute, these structures grow in number and in length until the entirety of the vesicle's interior is dense and saturated. These characteristics can be straightforwardly attributed to the appearance of membrane tubules, presumably formed as a response to the interaction between mβCD and the vesicle bilayer.

Throughout the process of tubule generation, the intensity of the mother membrane diminishes by ~60%, as the tubules translocate the labeled lipid to within the vesicle's lumen. The persistence length of these tubules are obtained by rendering the confocal image in FIJI (78). The external

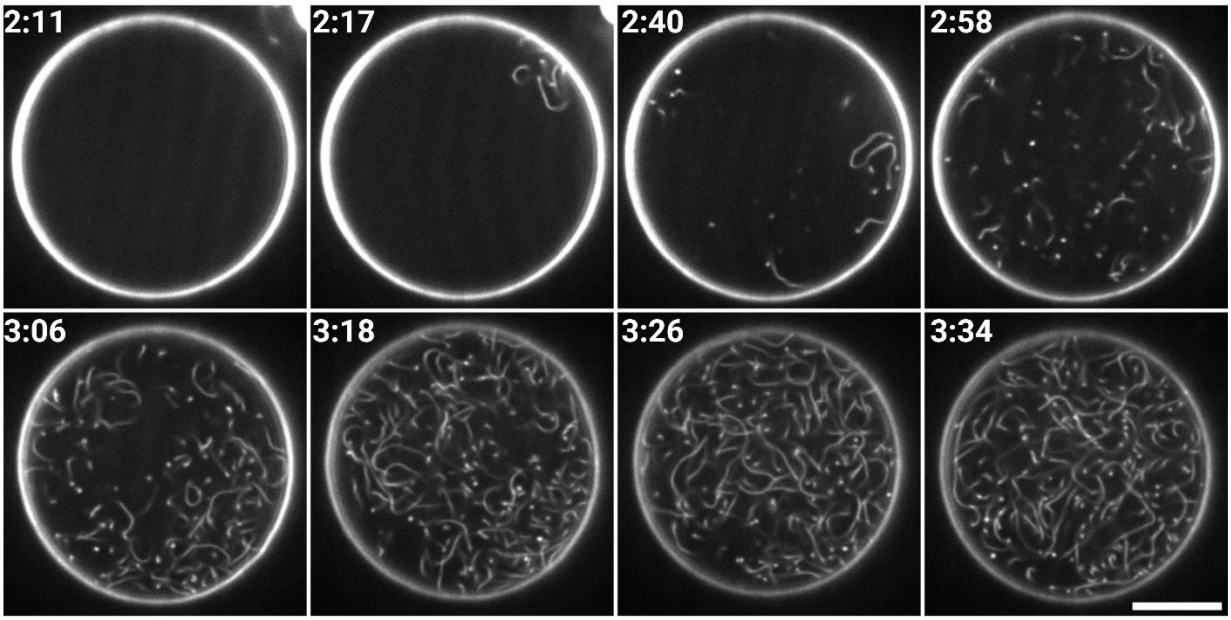

Figure 2.1*: Montage of confocal, xy-scan of a POPC GUV doped with 1 mol % Rho-B-DOPE following the addition of 1 mM mβCD. Images depict the formation of membrane tubules within the lumen of the vesicle over the course of a few minutes. Scale bar = 10µm.*

plugin FibrilJ (*79*) is used to deterministically vectorize each tubule in 2 dimensions (**Fig. 2.2d**). The vector data is imported into MatLab, where a series of internally written scripts calculate the tangent vectors along the nanotube. The persistence length of the tubules, L_p, correlates to the angle between vector segments by (*80*):

$$\langle t(s) \cdot t(s+x) \rangle = e^{\frac{-x}{2L_p}} \tag{2.1}$$

Where $\langle t(s) \cdot t(s+x) \rangle$ represents averaging the dot products of two vectors $t(s)$ and $t(s+x)$ separated by the difference in segments between them, x. The slope of the linear relationship between the natural log of these vectors as a function of x correlates to L_p (**Fig. 2.2a**). For tubules

formed from GUVs composed of pure POPC, a persistence length of 3.5 ± 0.1 μm is measured. Vesicles including cholesterol have a higher persistence length, 5.9 ± 0.3 μm and 7.4 ± 0.3 μm for POPC:SM:Chol = 1:1:1 and 2:2:1, respectively.

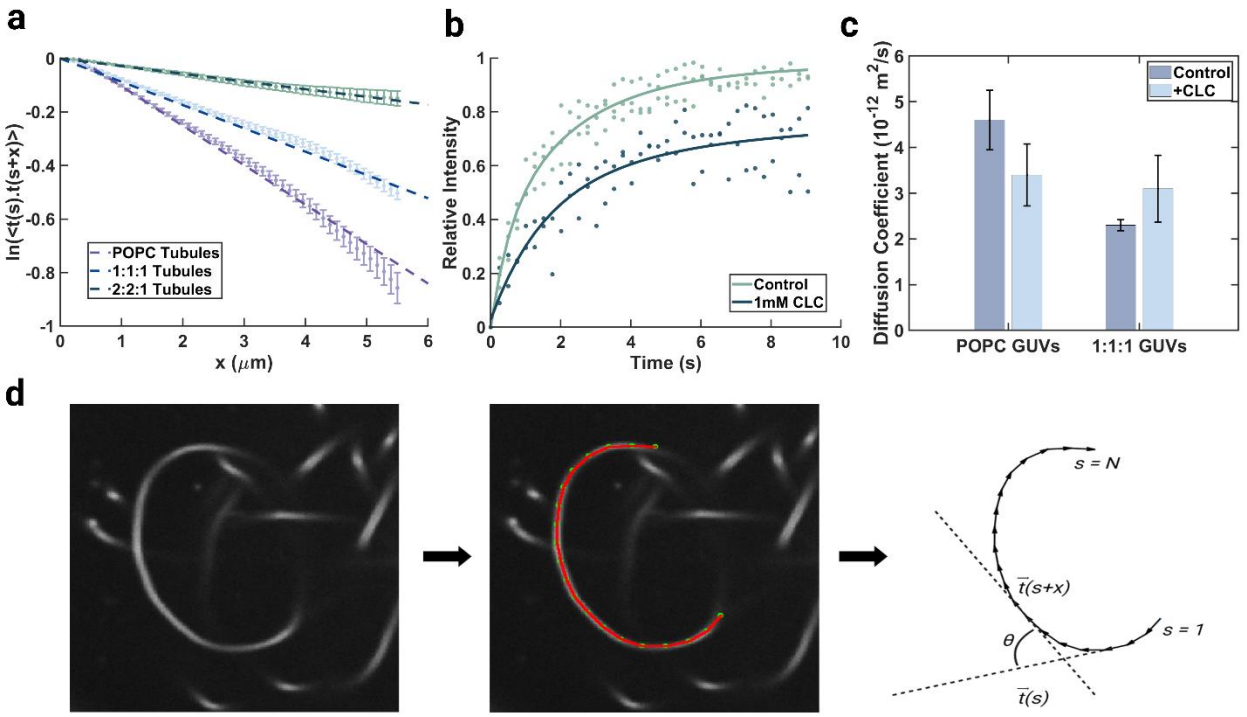

***Figure 2.2**: **a)** Quantification of persistence length measurements for GUVs composed of POPC or POPC:SM:Chol in 1:1:1 or 2:2:1 molar ratio. **b)** Fluorescence intensity recovery photobleaching of POPC GUVs before and after the addition of 1 mM Cholesterol loaded cyclodextrin (CLC) (~6:1). **c)** Comparison of the membrane diffusion coefficient of POPC and 1:1:1 GUVs determined by FRAP before and after the addition of 1 mM CLC (~6:1). **d)** Illustration of membrane tubule parameterization. Tubules are isolated and vectorized in FIJI, imported into MatLab and used in the quantification of persistence length.*

Considering these membrane tubules to be hollow cylinders of negligible wall thickness (typical membrane thickness of 3-5nm (81)), the radius of the tubules can be roughly estimated (**Table 1**)

by relating the experimentally determined persistence lengths with the force balance relationship between membrane tension σ and rigidity κ (82):

$$r_{tubule} = \frac{L_p(K_B T)}{2\pi\,\kappa} = \sqrt{\frac{\kappa}{2\sigma}} \tag{2.2}$$

The change in lateral diffusion of the membrane is quantified through the analysis of fluorescence recovery after photobleaching (FRAP) (**Fig. 2.2b**), before and after the addition of 0.5 mM cholesterol loaded cyclodextrin (CLC). The relative intensity recovery of the membrane following bleaching is used to estimate the diffusion of the membrane lipids, *D*:

$$D = \frac{r^2}{4\tau_{½}} \tag{2.3}$$

Where *r* is the radius of the bleached area and $\tau_{½}$ is the characteristic time of the relative intensity at which $I = I_{½}$. The membrane diffusion of POPC GUVs in an isomolar environment is initially measured to be $4.5 \pm 0.7 \times 10^{-12}\ m^2/s$, followed by the introduction of 1 mM CLC and subsequent FRAP

Membrane composition	L_p **(**μm**)**	**Tubule Radius** ***r*** **(*nm*)**	κ **(**K_bT**)**
POPC	3.5 ± 0.1	~30	18.5 ± 0.6 (83)
POPC:SM:Chol (1:1:1)	5.9 ± 0.3	~14	65.8 ± 4.9 (84)
POPC:SM:Chol (2:2:1)	7.4 ± 0.3	~18	78.0 ± 9.8 (L_d) (84)

measurement, resulting in a final diffusion coefficient of $2.7 \pm 0.2 \times 10^{-12}\ m^2/s$ (**Fig. 2.2c**). A marked drop in the fluidity of the membrane. In contrast, multi-component GUVs (1:1:1) show an increase in diffusion coefficient after the treatment of 0.5 mM CLC. An initial diffusion coefficient of $2.3 \pm 0.1 \times 10^{-12}\ m^2/s$ results in a significant increase to $3.1 \pm 0.7 \times 10^{-12}\ m^2/s$ following introduction of CLC. Both Rho-B-DOPE and NBD-PE were photobleached, separately and with an insignificant difference in diffusion measurements within the same experimental set.

2.3.2 mβCD induced phase separation and selective tubule composition in multi-component GUVs

Multicomponent GUVs are prepared from a mixture of cholesterol, POPC and egg-sphingomyelin (SM) and are prepared in either equimolar (1:1:1) or cholesterol poor (2:2:1) molar ratios. As expected, equimolar GUVs initially appear homogeneous (**Fig. 2.3b, t = 0**), as the compositional phase diagram predicts (75). Here, 0.5 mM of CLC is introduced to a collection of 1:1:1 GUVs, doped with 1 mol% of Rho-B-DOPE. After some time (<1min) the uniform membrane intensity of the equatorial plan becomes decorated by regions of contrasting high and low intensities (**Fig. 2.3b, t = 1:01**). The regions of higher intensity grow in size and appear circular on the surface of the membrane. By 2 minutes, inward tubules can be observed, primarily originating from the regions of high membrane intensity (**Fig. 2.3b, t = 2:17**). Over the next few minutes these tubules continue to form, depleting the regions of high intensity from the GUV's membrane. These regions of high intensity forming within the membrane are consistent and straightforwardly attributed to instances of phase separation. The membrane, doped with 1 mol% of Rho-B-DOPE, labels the liquid-disordered domain primarily composed of POPC and is cholesterol depleted. In this

composition, this domain is known to contain lipids of lower bending rigidity ($\frac{\kappa^{L_o}}{\kappa^{L_d}} \approx 1.25 \pm 0.60$ (85)).

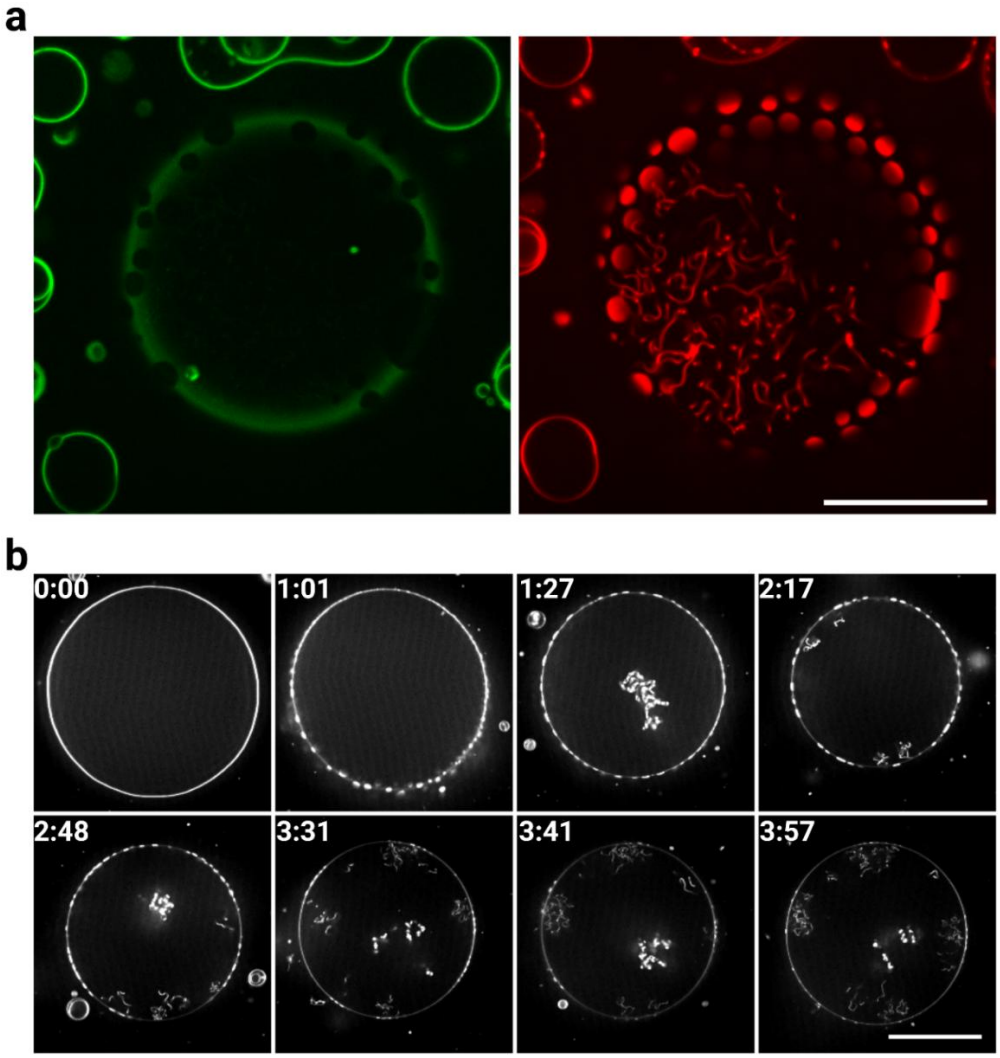

Figure 2.3*: X-Y confocal scans of POPC, SM and cholesterol GUVs, doped with 1 mol% of Rho-B-DOPE (red) and 3 mol% NBD-PE (green).* ***a)*** *Complimentary images of a 2:2:1 GUV depicting phase separation and tubulation. The left image captures the SM L_o domain, enriched with cholesterol and labeled with NBD-PE. The right image captures the POPC L_d domain, with clear preference in tubule formation.* ***b)*** *Montage of the Rho-B-DOPE channel of a 1:1:1 GUV, initially appearing homogenous. After the addition of 1 mM CLC, phase separation and tubule generation are observed. Tubules are primarily generated from the labeled domain (L_d) and deplete this domain from the membrane as they form.*

Cholesterol poor GUVs (2:2:1) initially appear phase separated. Similar to POPC and 1:1:1 GUVs, tubules are observed to appear following the introduction of CLC or mβCD. **Figure 2.3a** depicts complimentary phase separated domains of a 2:2:1 GUV following the treatment of 1 mM CLC. This GUV is doped with both 1 mol% of Rho-B-DOPE (red) and 3 mol% NBD-PE (green), preferentially labeling the liquid-disordered (L_d) and the liquid-ordered (L_o) domains, respectively. Tubules forming in this GUV appear to be overwhelmingly composed of the L_d domain.

2.4 Discussion

2.4.1 Membrane deformation as a response to leaflet asymmetry induced by mβCD

The diverse functionality of mβCD is attributed to its solubility in aqueous environments despite housing a hydrophobic cavity within its lumen. This non-polar cavity has been widely used as a means of solubilizing various hydrophobic molecules, namely sterols (*86*). Additionally, at high concentrations, mβCD was observed to bind and solubilize lipids (*87*), modifying the composition of a membrane through a lipidic exchange with individual leaflets within the bilayer (*59*). Observation of this behavior led researchers (such as Erwin Londen, et al.) to utilize cyclodextrin in a creative way, by modulating the lipid composition of a membranes extracellular leaflet to create tailored compositional asymmetry in synthetic vesicles (*55*, *57*), transforming minimal model cells into vesicles maintaining a compositional or chemical gradient across the membrane – a crucial factor for living cells.

A variation of what London proposes, we show that – as opposed to compositional asymmetry – mβCD selectively solubilizes POPC lipids from the outer leaflet of the GUV, inducing a differential stress across the membrane. This generates axial tension within the membrane – which

is maintained as a result of minimal phospholipid transversal diffusion (flip-flop, 10^{-15} s^{-1} (88)) – generating spontaneous curvature and forming nanotubules (89). Tubule membranes are ubiquitously found in plasma membranes and are crucial to a variety of cellular functions. Neurite growth relies on membrane filopodia, while cellular trafficking (90), embryo development and organelle membranes (ER & Golgi) all have molecular functions dependent on tubular mechanisms.

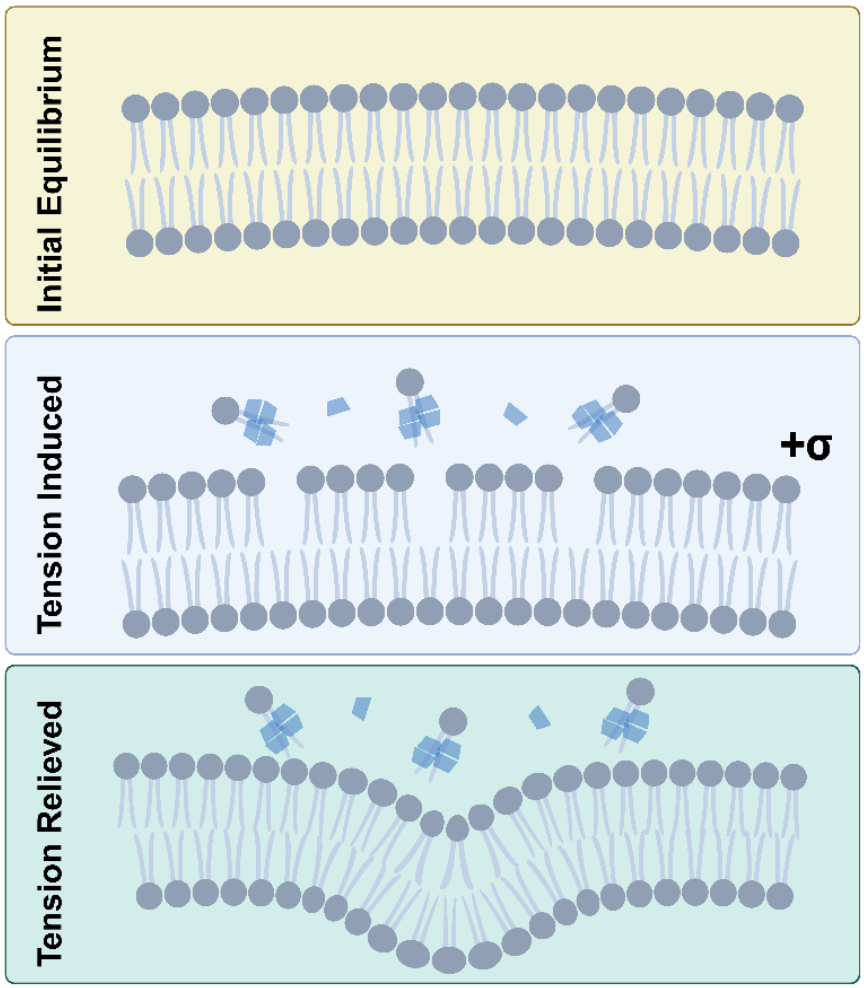

***Figure 2.4**: Cartoon depiction of how lipid removal causes a leaflet area mismatch, leading to membrane invaginations. An initially tensionless membrane experiences removal of lipids from the upper leaflet by mβCD, inducing an area mismatch and differential stress. This deformation and generation of curvature is generated to relieve this stress.*

Tubule formation as a result of protein-membrane interaction typically involve motor proteins (82), steric repulsion (91), or crowding induced curvature generation (92). Alternatively, non-protein sources of tubule generation are commonly a result of an osmotic pressure gradient (93), and also the cyclic oligosaccharide, cyclodextrin, reported here. The cylindrical nanotubes formed by CD are characterized by a constant mean curvature $M = -\frac{1}{2} * r_{tubule}$ and a vanishing stress in the radial direction perpendicular to the membrane.

The area-difference elasticity (ADE) model is one of many different ways to mathematically describe the membrane deformation in vesicular membranes (94):

$$W \equiv \frac{\kappa}{2}\oint dA\,[C_1(r) + C_2(r) - C_0]^2 + \frac{\overline{\kappa}}{2}\frac{\pi}{AD^2}(\Delta A - \Delta A_0)^2 \qquad (2.4)$$

The first term is the energy functional model, initially proposed by Canham (95) and Helfrich (96), described by the principle curvatures C_1 & C_2, spontaneous curvature C_0, and the elastic modulus κ integrated over the surface of the membrane. Accounting for the energetics of a leaflet mismatch is the second term, by a "nonlocal" bending rigidity $\bar{\kappa}$ – reflecting the fact that bending any bilayer of nonzero thickness expands one side while compressing the other – the distance between the bilayers D and the leaflet area difference, $\Delta A \equiv A^{out} - A^{in}$. This model is subject to constraints on the enclosed volume *V*, total surface area *A*, and the initial area difference between membrane leaflets, $\Delta A_0 \equiv A_0^{out} - A_0^{in}$.

The manner in which lipids are removed from the outer leaflet of the GUV membrane by mβCD produces lateral tension in the membrane (measured by a 40% decrease in POPC lipid diffusion), in addition to a differential stress induced by a reduction in the outer leaflet surface area. The relationship between L_p, σ and κ, depicted in equation (3), dictates the energetic balance between the reduction in tubule radius by the surface tension and how membrane rigidity acts against it (*82*), meanwhile, the ADE model describes a diminishing energetic cost of tubule formation through a mismatch in leaflet area. The consequence of these factors is the generation of the inward nanotubes, which we observe.

The usage of cyclodextrins as therapeutic, biosensor or as an effective vehicle for drug delivery relies on this clear understanding of the mechanisms of its membrane interaction. We have shown that mβCD has the capability to cause gross membrane deformation under the reported circumstances, a previously unappreciated side-effect in its typical usage.

2.4.2 Phase separation and tubule generation in cholesterol-containing GUVs

mβCD's high affinity for cholesterol raises an interesting question: By selectively binding and removing a specific sub-class of lipid molecule, does there remaining lipid pool within the membrane both undergo phase transitions and shape deformation? To begin to answer this question, we incubate mβCD with vesicles reconstituted in ternary lipid mixtures composed of POPC, sphingomyelin, and cholesterol in equimolar proportions. In this ratio, the phase diagram predicts the absence of domain formation at optical length scales (*75*). As expected, these GUVs initially appear homogeneous under isotonic conditions and at room temperature (**Fig. 2.3b, 0:00**) yet produce phase domains upon the introduction of 1mM CLC (**Fig. 2.3b, 1:01**).

It is notable that the formation of phase domains appears within a membrane of this composition. As previously discussed, we predict POPC GUVs form tubules as a response to both lateral tension and differential stress generated by the removal of lipids from the outer leaflet of the membrane. It is possible that these observations of phase separations might arise from these factors, as membrane tension is known to result decrease the energetic cost of forming membrane domains in GUVs of this composition (*26*). To address this possibility, we quantify membrane fluidity through a series of fluorescence-recovery after photobleaching (FRAP) measurement (**Fig. 2.2b**). The diffusion of both POPC and 1:1:1 GUVs is obtained before and after the addition of 0.5 mM CLC. Here, POPC GUVs undergo a reduction of membrane fluidity, as the diffusion drops from $4.5 \pm 0.7 \times 10^{-12}\ m^2/s$ to $2.7 \pm 0.2 \times 10^{-12}\ m^2/s$ (**Fig. 2.2c**). Generally, membranes under tension increase in membrane fluidity (*45*). Instead, the reduction in diffusion likely arises from the increase in cholesterol content (*86*, *97*). In contrast, 1:1:1 GUVs increase in fluidity, from a low of $2.3 \pm 0.1 \times 10^{-12}\ m^2/s$ to $3.1 \pm 0.7 \times 10^{-12}\ m^2/s$ (**Fig. 2.2c**). A significant increase, typically seen as a response to a reduction of cholesterol content by β-CDs (*86*).

With the above considerations we propose the following steps to describe phase separation and nanotubule generation seen in multi-component GUVs: (i) CLC is introduced to an initially homogeneous membrane. mβCD participates in the preferential removal of cholesterol (*98*, *99*) from the outer leaflet of the membrane. (ii) Cholesterol undergoes rapid transverse diffusion (10^3-10^4 s^{-1}) (*100*, *101*) acting to counteract the generation of leaflet density asymmetry across the membrane. (iii) The removal of primarily cholesterol from the membrane of the GUV leads to a shift of the membrane composition towards a two-domain state (*75*). (iv) Upon the appearance of

phase separation, the L_o domain has transitioned into a gel-like ordering of lipids, suppressing the ability for cholesterol to readily flip-flop. (v) Without cholesterol counteracting differential stress, continued removal of lipid, sphingomyelin (*102*) or cholesterol results in the generation leaflet asymmetry. This asymmetry generates spontaneous curvature within the fluid domain (L_d), resulting in tubule formation composed of primarily POPC (**Fig. 2.3a & 2.3b**).

2.5 Materials and Methods

Materials

1-Palmitoyl-2-oleoyl-sn-glycero-3-phosphocholine (POPC), 1,2-dioleoyl-sn-glycero-3-phosphocholine (DOPC), 1-palmitoyl-2-oleoyl-sn-glycero-3-phospho-L-serine (sodium salt) (POPS), egg-sphingomyelin, Cholesterol, and lissamine rhodamine B 1,2-dioleyl-sn-glycero-3-phosphoethanolamine (Rho-B DOPE) were acquired from Avanti Polar Lipids (Alabaster, AL). Glucose was obtained from Sigma-Aldrich (St. Louis, MO), and 2-deoxy2-[(7-nitro-2,1,3-benzoxadiazol-4-yl) amino]-D-glucose (2-NBDG) was obtained from Cayman Chemical (Ann Arbor, MI). Sucrose was obtained from EMD Chemicals (Philadelphia, PA). Chloroform, head-labeled N-(7-nitrobenz-2-oxa-1,3-diazol-4-yl)-1,2-dihexadecanoyl-sn-glycero-3phosphoethanolamine, triethylammonium salt (NBD-PE) and head labeled Texas Red™ 1,2-Dihexadecanoyl-sn-Glycero-3-Phosphoethanolamine, Triethylammonium Salt (Texas Red™ DHPE) was obtained from Thermo Fisher Scientific (Waltham, MA).

Glass-bottom, 96-well plates were obtained from Cellvis (Mountain View, CA). Indium tin oxide (ITO)-coated glass slides (5-25 Ω) were obtained from Delta Technologies, LTD (Loveland, CO). Manual Teflon-tipped syringes were obtained from Agilent Technologies (Santa Clara, CA).

2.5.1 Preparation of synthetic model membranes

GUVs

GUV preparation via electroformation is a well-established process (*13*, *103*). A lipid stock of a desired composition at a concentration of 2mg/mL is prepared in chloroform. For single component synthetic membranes, POPC (99 mol %) is dissolved with a Rho-B DOPE label (1 mol %). Cholesterol containing membranes are prepared with a combination of POPC, egg-Sphingomyelin, and Cholesterol with the fluorescent labels of Rho-B DOPE (L_d domain) and NBD-PE (L_o Domain) at a molar ratio of either 32:32:32:1:3 or 38.4:38.4:19.2:1:3, respectively. DOPC:POPS or DOPC:DOPS lipid mixtures are doped with prepared with Rho-B DOPE label at a molar ratio of 79:20:1. For all lipid stock, 15uL is deposited onto the conductive side of two ITO-coated slides and spread evenly on half of the slide as it evaporates. These slides are further dried inside a vacuum desiccator from anywhere from 2 – 24 hrs. Once dry, a chamber is formed using a 1-mm-thick rubber O ring (Ace Hardware, Davis, CA) and sealed with high-vacuum grease (Dow Corning, Midland, MI). After the O ring is adhered to the conductive side of the ITO-slide, the chamber is hydrated with ~1 mL of a 100 mM Sucrose solution. The chamber is sealed with the second, inward facing lipid cake, ITO-slide ensuring no trapped air bubbles. The two slides form the chamber in a way that the halves without dried lipid are facing in opposite directions to avoid the alligator clips from the function generator from touching both slides, effectively forming a less resistant pathway for any current. A 2.2 V(pp) AC Sine wave is applied across the two slides at a frequency of 10 Hz for 1 hour, followed by another 2.2 V(pp) AC Sine wave at a frequency of 2 Hz for 30 minutes. Vesicles containing egg-SM undergo this step at a temperature of 55°C.

All samples undergo this step covered to protect from light. After GUV formation, the chamber is disassembled, and the solution is pipetted into a small centrifuge tube and stored at 4°C. Vesicles prepared are either used or discarded within a week of preparation.

2.5.2 Preparation of mβCD and mβCD:chol Complex Solutions:

Cholesterol-water soluble (~6:1 CD:cho) (Sigma-Aldrich (St. Louis, MO)) was hydrated in DI to prepare 100 mM mβCD (~951mg mβCD per gram). The solution was sonicated for 5 minutes at room temperature until completely dissolved. Pure mβCD solutions were prepared in the same manner.

Alternate mβCD:chol ratios were prepared by dissolving the desired molar ratio of mβCD and cholesterol in methanol. For 0.5 mL of 100 mM mβCD:chol = 3:1, 66mg of mβCD and 0.323 mL of 20 mg/ml cholesterol were used. The solution was evaporated by nitrogen and placed in a desiccation chamber overnight. The film was rehydrated with DI to bring the final concentration to 100 mM and sonicated for 5 minutes. The final solution should be slightly turbid.

Chapter 3

Apolipoprotein interaction induces shape remodeling and lipid phase separation in giant unilamellar vesicles

This chapter has been adapted from:

> Carnahan, Christopher Fjeld, et al. "Apolipoprotein interaction induces shape remodeling and lipid phase separation in giant unilamellar vesicles." *bioRxiv* (2025): 2025-04.

3.1 Abstract

Apolipoprotein A-I (ApoA-I) – a 243-residue amphipathic protein containing an N-terminal globular domain and a primarily helical C-terminal lipid binding domain – is a principal protein component of high-density lipoprotein (HDL) or "good" cholesterol, which is an important component of lipid homeostasis in humans. Synthesized in the liver and intestine and excreted in the blood, ApoA-I undergoes complex, cooperative, and dynamic self-assembly with membrane lipids producing unlipidated (or weakly lapidated), nascent discoidal, and mature HDL states. *In vitro* studies establish that the recombination of purified protein and lipids reconstitutes this cooperative self-assembly. However, the kinetic pathways by which these mesoscopic, proteolipidic assemblies form remain incompletely understood. Here, we monitor the dynamics of ApoA-I-membrane interactions through real-time monitoring of morphological changes, which ensue when ApoA-I is incubated with minimal giant unilamellar vesicles (GUVs) composed of single phospholipids or phase-separating phospholipid-cholesterol mixtures. Our fluorescence and atomic force microscopy measurements reveal that the interaction produces discoidal particles while remodeling the parent vesicle in discrete stages involving membrane poration, solute leakage, vesiculation, and lipid-lipid phase separation. We find that the qualitative phenomenology is robust and fully reproducible for different protein mutants and alleles (WT APOA-1, Δ49ApoA-I, ApoE-3, and ApoE-4) and different lipid mixtures (PC, PC+PS), we tested. Our molecular simulations recapitulate the essential shape changes and further reveal the composition dependence of the interactions. Together, these findings depict key steps in the

protein-lipid interactions, which guide the assembly of mesoscopic reconstituted lipoproteins and nanodiscs.

3.2 Introduction

Lipids are an amphiphilic molecule that play essential roles in membrane synthesis, energy storage, and cell signaling. The ability to transport them from the sites of absorption (or syntheses) to other cells and tissues – as a means to distribute metabolic energy – represents a critical step in the evolution of multicellular organisms (*104*). In animals, this function is enabled by the collective transport of lipids in the form of micelle-like, colloidal nanoparticles through the aqueous circulatory system.

Collectively termed lipoproteins, these circulating nanoparticles are supramolecular, mesoscopic complexes consisting of mixtures of several different classes of lipids (e.g., triglycerides, cholesterol, and phospholipids) and one or more proteins called apolipoproteins (*105*). Morphologically, they are organized into spheroidal particles consisting of an outer layer of phospholipids, unesterified cholesterol, and proteins, encapsulating the central core made up of neutral lipids, predominately cholesteryl ester, and triacylglycerols (*106*). Although most lipoproteins share these structural features, they also exhibit considerable structural, compositional, and morphological variations. An early basis for the classification and fractionation of the lipoprotein diversity was the particle density: different lipoproteins floated differentially in repeated ultracentrifugations with progressively increased densities (*107*). Subsequent efforts revealed additional criteria for classifying lipoprotein diversity (*108*, *109*), including sizes, electrophoretic mobilities, lipid and protein compositions, and metabolic functions. Currently, the

most common classification recognizes six different classes of human lipoproteins (105). These classes include (i) *chylomicrons*, which are >100 nm in diameter and commonly synthesized in intestine; (ii) *chylomicron remnants*, which form after lipoprotein lipase hydrolyze the triglycerides of the source chylomicrons; (iii) *very-low-density lipoproteins* (VLDL, d < 1.006 g/mL and diameter, 30-90 nm), produced in the liver; (iv, v) *intermediate-density lipoproteins* (IDL, d = 1.006-1.019 g/ml) and *low-density lipoproteins* (LDL, d = 1.019-1.063 g/mL).), produced by the lipase activity on VLDLs; and (6) *high-density lipoproteins* (HDL, d = 1.063-1.21 g/mL), which have the smallest sizes of 8-12 nm in diameter. Within each of these classes, a significant compositional variability exists, making lipoproteins one of the most compositionally heterogeneous classes of particles in blood.

In addition to being the smallest (~8-12 nm in diameter) and the densest (d = 1.063-1.21 g/mL), HDLs are also compositionally and functionally distinct (110). Metabolically, they play a major role in reverse cholesterol transport, a mechanism by which circulating HDLs draw cholesterol from the cells of the peripheral tissues and return it to the liver for excretion (111, 112). This role in mediating macrophage cholesterol efflux is thought to be primarily responsible for the inverse correlation between their concentrations in plasma levels and the risk for coronary artery disease (113, 114), rendering HDLs uniquely atheroprotective. HDLs are also compositionally distinct from their lipoprotein counterparts. Their lipids are not solubilized by apolipoprotein B. Instead, they are bounded, most dominantly, by ApoA-I – a single polypeptide of 243 amino acids secreted in the intestine and liver (115, 116) – which accounts for ~70% of the total protein mass of HDL particles (110).

In vivo, HDL assembly begins with the activity of ATP-binding cassette transporter ABCA1, a membrane protein. According to the alternating access mechanism, an activated ABCA1 flips phospholipids from the cytoplasmic to the outer, exocytoplasmic leaflets of plasma membranes (*117*). The resulting excess lipid density (and area) in the outer leaflet promotes vesiculation and efflux of phospholipids and cholesterol to the extracellular space in the form of vesicles. A recent computer simulation (*118*) proposes an alternate view. It suggests that upon activation, ABCA1 acts as a phospholipid translocase, extracting lipids from the outer exocytoplasmic leaflet to form a luminal structure, that migrates into the extracellular space as vesicles. In both cases, lipid-poor ApoA-I activates ABCA1 and interacts with the vesicles produced by the ABCA1 activity in the extracellular space, leading to the formation of nascent HDLs. These newly formed HDLs are discoidal in morphology. Subsequent esterification of cholesterol by the enzyme lecithin: cholesterol acyltransferase (LCAT) initiates the formation of the hydrophobic core and induces the shape transformation from the discoidal to the spheroidal morphology (*119*).

As discrete nanoscale compartments transporting lipids and membrane proteins through aqueous environments, HDLs and their synthetic counterparts are appealing for many biomolecular technologies (*120*). Reconstituted *de novo* by incubating pre-determined mixtures of lipids with apolipoprotein (as well as their truncated variants called membrane scaffold proteins or MSPs) or synthetic polymers (e.g., styrene-maleic acid, SMA) (*121*, *122*), these reconstituted HDLs (rHDLs) – also called nanolipoproteins (NLPs) and nanodiscs – mimic an intermediate discoidal state of ApoA-I found *in vivo* (*123*). These constructs are proving valuable for solubilizing membrane proteins (*124-127*), tailoring membrane compositions (*128*), and screening membrane-protein targeting drugs and therapies (*129*, *130*).

For both the biotechnological and biomedical applications of HDLs, understanding molecular mechanisms by which ApoA-I disrupts topologically closed lipid vesicles is important. Much of our current knowledge is obtained from computer simulations and *in vitro* reconstitution studies. Two limiting modes of protein-lipid association in the formation of discoidal rHDLs have been proposed: (i) the picket fence model, where two ApoA-I molecules wrap around a disc of a single lipid bilayer with adjacent alpha-helices in antiparallel orientation, parallel to the acyl chain of the phospholipids (*131*, *132*) and (ii) the double-belt model, where two antiparallel ApoA-I are oriented perpendicular to the lipid tails (*133*). The bulk of the experimental evidence currently favors the belt model, but the hybrid conformations in HDL subpopulations where some of the ApoA-I helices are perpendicular to the lipid tails have not been fully ruled out.

For either model, the dynamics of the alpha-helical segments of ApoA-I play important roles. ApoA-I is an amphipathic protein that contains a globular N-terminal domain (residues 1-43) and a lipid-binding C-terminal domain (residues 44-243). As secreted, lipid-poor ApoA-I features five amphipathic helices spanning residues 7-44, 54-65, 70-78, 81-115, and 147-178. Together, these helices make up approximately 50% of the protein content (*134*). The free energies of stability for these helices in the lipid-free state are estimated to be in the range of 3-5 kcal/mol (~5-9 k_bT), sufficient to provide stable helical segments, however, these values are lower than 5-10 kcal/mol (~9-17 k_bT) typically observed for globular proteins, suggesting that the protein is highly conformationally dynamic. Together, these features allow ApoA-I to unfold and refold readily. This structural plasticity is essential to its function, allowing for the stability of both the discoidal and spheroidal assemblies with varied lipid stoichiometries. Specific protein conformational

changes – specifically the increase in the alpha-helical content of the protein (135, 136) – that accompany HDL assembly are now well-understood (137).

Still, our understanding of how ApoA-I interacts with organized lipid mesophases, such as membranes, vesicles, and liposomes, remains incomplete. Computer simulations and *in vitro* reconstitution studies suggest roles of packing density (138), packing defects (139), and local membrane curvatures in driving the assembly (140). However, the kinetic pathways and structural intermediates – how ApoA-I invades a topologically closed membrane, disrupts its structure, assembles lipoproteins, and what remains of the parent membrane – remain incompletely understood. To begin to address these questions here, we probe the real-time interactions between a truncated isoform of ApoA-I and lipid bilayers organized as giant unilamellar vesicles. By employing a platform that enables visual characterization, we identify previously unappreciated previously unrecognized biophysical steps – including poration, vesiculation, and phase separation – which mark the ApoA-I – membrane interactions *en route* to the formation of HDL-like particles.

3.3 Results and Discussion

We begin by investigating the interaction between ApoA-I and single lipid bilayers. For our study, we used a N-terminally truncated isoform of ApoA-I in which the first 49 amino acids are removed: Δ49ApoA-I. This modification has been previously shown to preserve the essential lipoprotein-lipid interactions (141). Our lipid source for reconstituting HDL-like particles is a suspension of protein- and cytosol-free, model phospholipid membranes of closed topologies, i.e., giant unilamellar vesicles (GUVs, 15-30 μm diameter) (13). We used both single-component and multicomponent GUVs. Our single component GUVs consist of the mono-unsaturated

phospholipid, 1-palmitoyl 2-oleoyl-*sn*-1-glycero-3-phosphocholine (POPC). Our multi-component GUVs are reconstituted using ternary lipid mixtures composed of POPC, egg-sphingomyelin (SM), and cholesterol (Chol) in equimolar (1:1:1) and cholesterol poor (2:2:1) proportions. Depending on composition and temperature, these lipid mixtures are known to organize as a singular, uniform phase or exhibit phase separation (*75*), forming two co-existing liquid phases: a dense phase enriched in SM and Chol, designated as the liquid-ordered phase (L_o) and a second, less dense liquid-disordered phase (L_d) consisting primarily of POPC. Differentiation between the L_o and L_d phases through fluorescence microscopy is achieved by doping the GUVs with small concentrations (1 mol %) of a phase sensitive probe, N-lissamine rhodamine dioleoyl phosphatidylethanolamine (Rho-DOPE, Ex/Em, 560/583 nm) (*76*). At the equimolar (1:1:1) composition, the phase diagram predicts the absence of domain formation at optical length scales (*75*) but does not rule out existence of nanoscale domains (*77*). Consistent with this prediction, GUVs encapsulating 100 mM sucrose appear optically homogeneous at room temperature in an osmotically balanced, isotonic medium containing 100 mM glucose. Monitoring the temporal changes using spinning disc confocal and wide-field fluorescence microscopy allows us to follow the morphological and topological transformations of these GUVs.

Introducing Δ49ApoA-I to a suspension of single component, POPC GUVs (decorated with 1 mol % Rhodamine PE and encapsulating 100μM of an NBD-labeled glucose (NBD-G, Ex/Em, 475/550 nm) in the interior) triggers gross membrane remodeling (**Supplementary Video 3.1**) characterized by a well-defined sequence of structural, morphological, and topological transformations (**Fig. 3.1**).

3.3.1 Δ49ApoA-I-membrane interactions produce microscopic pores

The first major event involves a transient, short-lived appearance of an intensity modulation at the membrane surface. Here, the uniform fluorescence intensity decorating the equatorial plane in the confocal fluorescence images of single GUVs is replaced, transiently, by a Janus binary pattern of fluorescence (**Fig. 3.1a - 17s**) consisting of (i): a dominant segment with the fluorescence intensity comparable to that prior to the change and (ii) a smaller arc or a domain, roughly 2 μm in width, with the vanishingly low fluorescence intensity comparable to the background value ($I_{membrane}$ / I_{arc} = 1,400 %). This intensity perturbation lasts less than 2 seconds before homogenizing. Comparing across multiple experiments, we find that the event is reproducible; it also exhibits considerable variability in the lag time (10-500 s), time after the introduction of protein that we witness the event, and the lifetime (200 ms – 2 s), the time over which patterned intensity persists (**Figure S3.1**). In all cases, these short-lived arcs of low fluorescence are of microscopic (2 - 5 μm in diameter) dimensions, reminiscent of a transient microscopic pore in the GUV membrane. The variable lag time we observe is consistent with the stochastic nature of the pore formation.

The appearance of microscopic pores following ApoA-I interaction begs a question: Are the observed pores related to the known phenomenon of peptide-induced membrane poration? It is now well established that many proteins and antimicrobial peptides (e.g., defensin, magainin 2, mellitin, almethicin, protegrin, nystatin and actinoporins to name a few) – in particular, those that adopt amphipathic α-helical conformation upon interaction with lipid or cellular membranes – disrupts membrane integrity either by forming transmembrane pores (*142-148*) or by mechanochemically altering membrane permeability through interfacial activity (*149*). In all cases, AMP-mediated poration involves the formation of spatially localized, nanoscopic pores. typically

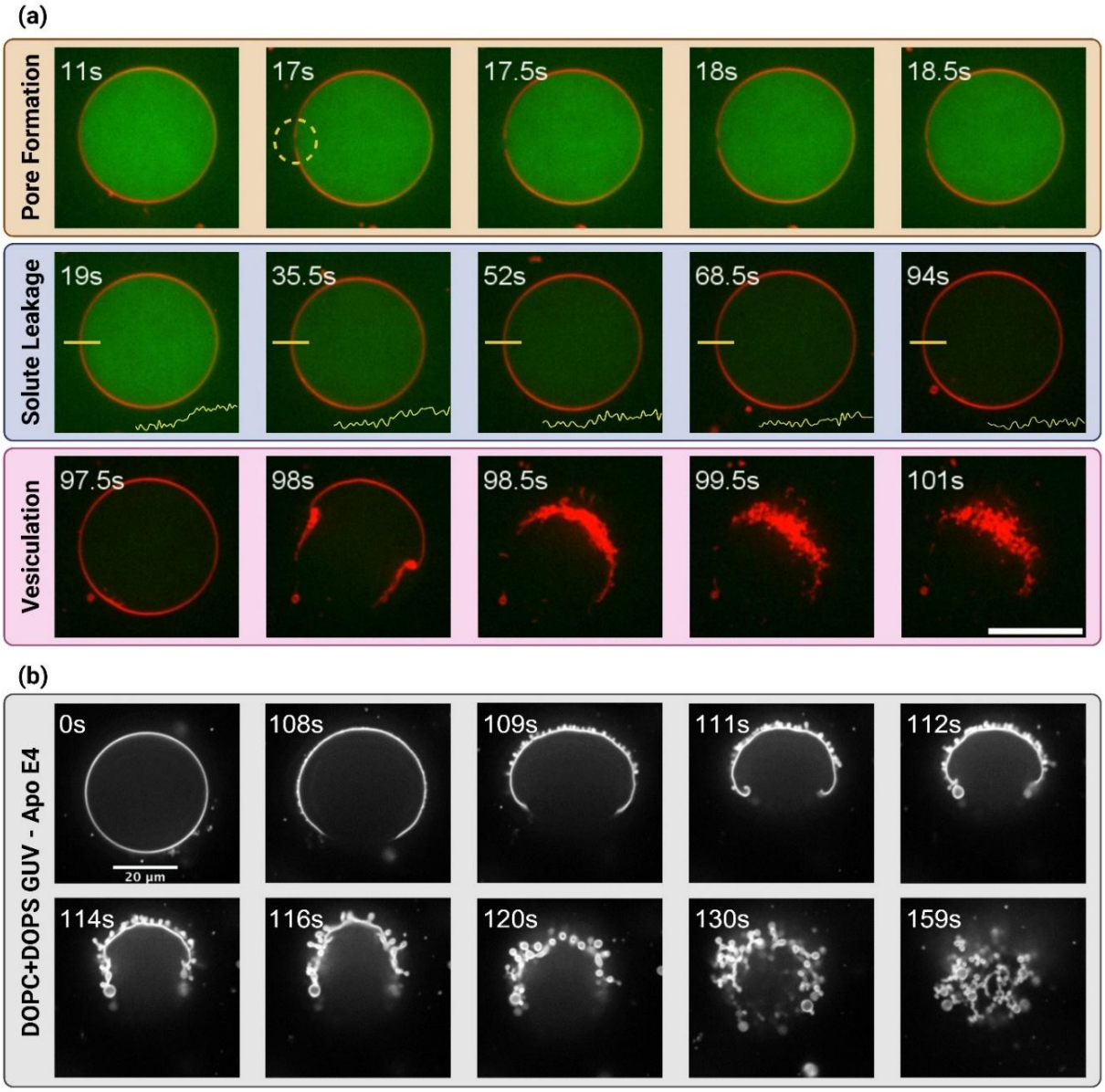

***Figure 3.5**: **(a)** Confocal xy-scan montage of a POPC GUV doped with 1 mol % Rho-B-DOPE (red) and encapsulating 100µM of a soluble, membrane impermeable dye NBD-G (green). The GUV is exposed to 0.88µM Δ49ApoA-I (Supplementary Video 4). At 17 seconds, a pore formation event can be seen (circled in yellow) and persists for ~2 seconds. Leakage of the encapsulated fluorophore depicted in the second row. Intensity characterized by the yellow line. Vesiculation depicted in the third row, occurring rapidly within 1 second. Scale bar 10µm. **(b)** Montage of a DOPC-DOPS-Rho (79:20:1) GUV exposed to 20µM ApoE4. Vesiculation occurs over several minutes and results in clearly spherical daughter vesicles.*

1-3 nm (*146*, *147*, *150*, *151*). The transient microscopic pores, we witness, by contrast, are orders of magnitude larger, suggesting that they are unlikely to be related to peptide-induced membrane poration. The most likely explanation is that the pores appear because of a cumulated loss of membrane area caused by ApoA-I-mediated lipid removal and concomitant formation of rHDL or NLP particles (Further discussion of this scenario is deferred to a later section in the chapter).

To directly test whether the incubation of GUVs with Δ49ApoA-I produces NLP particles, we investigated the GUV bathing medium using high-speed atomic force microscopy (HS-AFM). Scanning the deposits of the solution on planar substrates (see experimental methods), we find evidence for the appearance of a population of discrete disk-shaped structures even when GUVs are nominally intact (**Fig. 3.2a**). These structures have an average height of 4.5 ± 1.1 nm and an average diameter of 14.0 ± 4.0 nm (**Fig. 3.2b & 3.2c**) – in excellent agreement with the formation of NLPs (*152*, *153*). Consistent with earlier reports of lipid exchange between Δ49ApoA-I NLPs and supported bilayers occurring in 15 minutes (*154*), our results support the picture that Δ49ApoA-I stochastically binds the membrane, extracts lipids, and produces NLPs concomitantly rendering the parent GUV tense, yet nominally intact.

These observations of NLP formation can be readily reconciled with those of transient pore formation (see above). The formation of NLPs requires that the lipids be drawn stochastically from the GUV membrane. With each peptide-promoted lipid loss the residual GUV membrane experiences a reduced lipid density, which, in turn, raises the membrane tension (*45*). Of course, this view presumes that the vesicular integrity is not compromised and that the isotonic conditions within the bath ensure the constant volume [Note that the difference in solute concentration (Δc)

between the bath and the encapsulated solvent is initially isotonic. Thus, the osmotic pressure acts to maintain the encapsulated volume, as prescribed by Van't Hoff's equation ($\Delta\Pi = RT\Delta c$), where R is the gas constant and T the absolute temperature]. Beyond a threshold lateral tension, the membrane ruptures through the well-known phenomenon of tension-induced membrane poration (*26*, *46*, *155*, *156*). Specifically, it is now known that when membrane tension exceeds ~6 mN/m, energetics favor pore formation (*46*). This, in turn, sets the stage for additional morphological changes: (*157*) (i) the open pore permits the redistribution of lipids, allowing the membrane to relieve lateral tension (σ) , and (ii) the encapsulated liquid (solute and solvent) leaks through the open pore due to the excess of Laplace pressure, ($\Delta P = 2\sigma/R$) decreasing the radius of the vesicle, R. These changes culminate with the healing of the pore and the resealing of the membrane. With the continued removal of lipids by ApoA-I, the process can be repeated multiple times.

3.3.2 Solute leakage through a cascade of pore formation events

A key consequence of the formation of transient pores is the accompanying mixing of the encapsulated solution with the external bath. To track this leakage, we monitor a membrane-impermeable (permeation constant, ~6-25 x 10^{-9} cm/s) (*158*) fluorescent marker, NBD-glucose (green, 100 μM), encapsulated within a GUV. Images shown in **Fig. 3.1a** reveal that the fluorescence intensity of the dye diminishes gradually, until optical homogeneity is achieved with the surrounding bath. Observing several different GUVs of different sizes (r = 3-23 μm), we find that the intensity follows a sigmoidal decay (**Fig. 3.2d**) with variable lag time (~10-700 s) and persists over a broad window of time (5-94 s) before reaching a homogeneous plateau (averaging ~20 ± 7 s (**Fig. 3.2e**)).

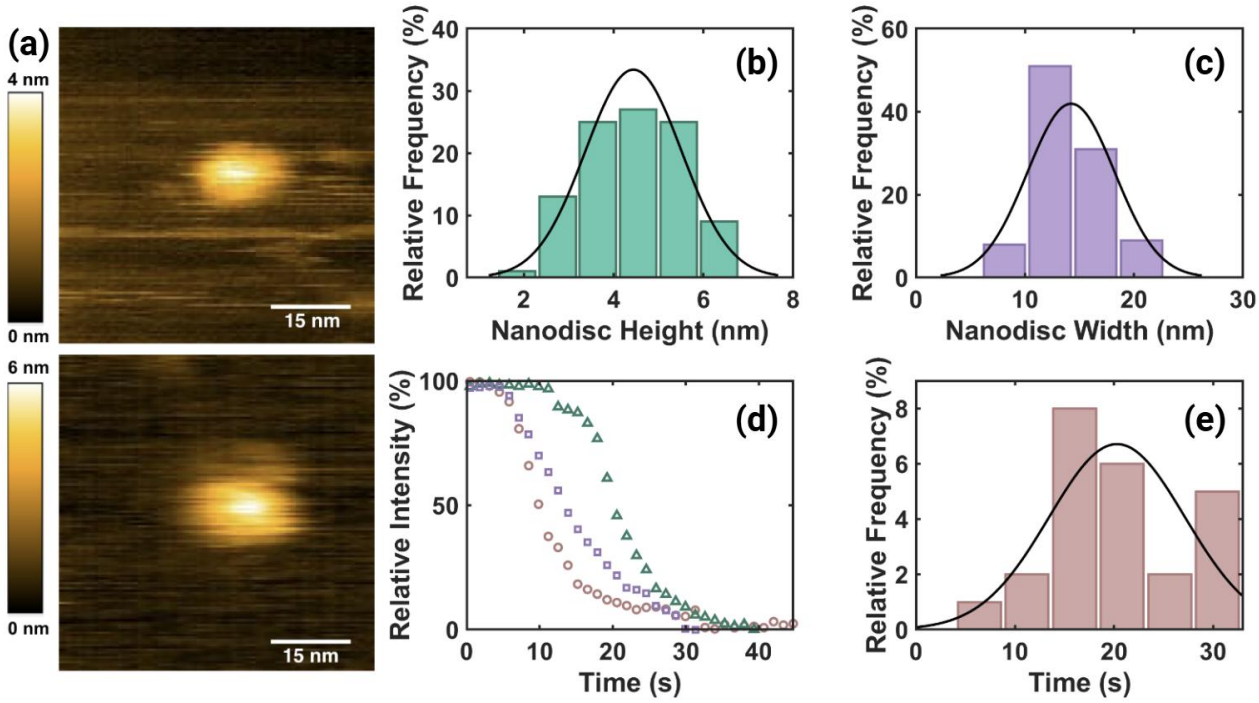

***Figure 3.6**: **(a)** AFM images depicting nanodisc appearance. **(b)** Histogram of NLP height and **(c)** NLP width collected using HS-AFM. **(d)** Three examples of NBD-G intensity leakage profiles from POPC GUVs following the addition of ~0.88 μM Δ49ApoA-I (supplementary video 2) **(e)** Relative frequency histogram for full leakage of NBD-G from POPC GUVs (24 GUVs) ($\bar{t} = 20.3s$).*

The time taken for the encapsulated intensity of NBD-G to homogenize to the background intensity (~20 ± 7 s) (**Fig. 3.2e**) is significantly longer than the lifetime of any pore formation events we observe (0.2 – 2 s). Stochastic pore nature and optical limitations of confocal microscopy limit our direct observations of transient pores to, at most, a single pore per GUV, however, we often observe secondary evidence of multiple pore formation events through fluctuations in membrane radius (**Supplementary video 3.2**). It seems reasonable that the leakage of the dye occurs through multiple pore formation events: multiple rounds of lipid removal and tension generation, because of the continued Δ49ApoA-I activity (**Fig. S3.2**). In a striking parallel, this behavior resembles that of membrane equilibration under hypotonic stress. Here, repeated cycles

of elemental biophysical processes – including osmotically-mediated water influx, generation of membrane tension, membrane failure through pore formation, solute efflux through open pore, and pore healing – led to osmotic equilibration (*26*).

3.3.3 Vesiculation and lysis of single-component GUVs

The observations of membrane poration, solute, and solvent exchanges above precede the most consequential structural remodeling leading to large-scale morphological and topological transformations because of the interactions of GUVs with Δ49ApoA-I. Beginning at ~98 s (**Fig. 3.1a**), the epifluorescence images at the equatorial plane of this POPC GUV show a dramatic membrane restructuring. The optically uniform and continuous circle of fluorescence at the equatorial perimeter is replaced by an open arc terminating into a string of closely spaced, smaller circular features with diameters of less than one micrometer (< 1 μm). These features form abruptly over 2 - 3 frames (< 1 s). The fluorescence emission from these clusters is more intense (I_{small}/I_{mother} = 200%) than that of the surrounding mother membrane. **Supplementary video 3.2** depicts an example where similar topological change occurs in nearly all POPC GUVs during the observed period (17 min).

These observations are reproducible (**Supplementary Videos 3.1-3.6**) across multiple independent experiments. Previous studies report slow spontaneous formation of rHDL by WT ApoA-I from POPC LUVs at 37°C (*159*). Additionally, membrane curvature generation in response to ApoA-I has been previously observed (*140*), without significant elaboration. To understand whether our observations were unique to ApoA-I, we carried out additional experiments utilizing wildtype ApoA-I, ApoE-4, and ApoE-3. When these peptides were

introduced to GUVs composed of 4:1 DOPC-DOPS, qualitatively similar results observed. As an example, the breakdowns of a 4:1 DOPC-DOPS GUV exposed to 20 μM and 0.44 μM ApoE-4, respectively, are depicted in **Figure 3.1b** and **Figure S3.3**. Another example in **Figure S3.4** presents a montage of a 4:1 DOPC-DOPS GUV vesiculation in response to exposure to 7.4 μM ApoE-3. Together, these observations indicate that these instances of membrane restructuring are not limited to the WT ApoA-I isoform or its Δ49 variant. Instead, they reflect a consistent pattern of membrane deformations characterizing the interaction between apolipoproteins and lipid membranes.

These large-scale membrane deformations are consistent with a known aspect of ApoA-I-membrane interactions, namely conformational change. It is now well-established that the membrane binding induces a significant conformational shift in ApoA-I increasing the helical segment from ~50% to ~80% (*135*, *136*). The increase in the helical segment population then triggers enhanced "interfacial activity (*149*)," which reflects the increased ability of the protein to (i) bind the membrane; (ii) partition into the membrane–water interface, acting as a wedge altering the packing and organization of the lipids within the membrane (*35*, *36*); and induce an area mismatch (*37*) between the two individual leaflets that make up the phospholipid bilayer. These mechanical deformations synergistically serve to reduce the energy cost for the creation of curvature generation (*38*) and thus promote vesiculation, such as we observe.

3.3.4 Coarse-grained molecular dynamics simulations with WT and Δ49ApoA-I

To further characterize the ApoA-I-mediated membrane deformations, we carried out coarse-grained molecular dynamics simulations. We studied interactions of both the **WT and Δ49ApoA-**

I with lipid bilayers composed of 100% POPC, 4:1 POPC:POPS, 1:1:1 POPC:DPSM:Chol and the PM8 lipid mixture (See Methods). For all bilayer compositions, we pre-assembled the double-belt and placed it 4 nm away from the bilayer surface. For each membrane condition, three independent simulations demonstrate that, without any restraints, the double-belt protein collapses into an 8-shape within the first 35-100 ns of the simulations and this conformation remains stable for the rest of the simulations regardless of the membrane composition (**Fig S3.5. a-d, the first three rows**).

With restraints, we ensure that the double-belt conformation remains as an open ring that is still able to undergo significant conformational changes (**Fig S3.5. a-d, the last three rows**). In 100% POPC membranes (**Fig. S3.5a**), the WT ApoA-I interacts with the surface, either continuously or intermittently, without significant perturbation in all simulations except for one, in which a small portion of POPC lipid is captured by the protein and remains deformed throughout the rest of the simulation. For membranes composed of 4:1 POPC:POPS (**Fig. S3.5b**), at least some parts of the WT ApoA-I continuously interact with the membrane. In 4 of 6 independent simulations containing a 4:1 POPC:POPS membrane, membranes show mild deformations due to interactions with the protein. In 1:1:1 POPC:DPSM:Chol membranes (**Fig. S5c**), the WT ApoA-I intermittently interacts with the membrane,

without significant morphological defects. Finally, in the PM8 membranes (**Fig. S3.5d**), it takes about 300 ns to 1 μs for the WT ApoA-I to fully sit on the PM8 membrane surface (**Fig. 3.3a**) in all independent simulations and afterwards, stable protein-membrane interactions are maintained. These stable interactions cause significant deformations on the surface of PM8 membranes in all

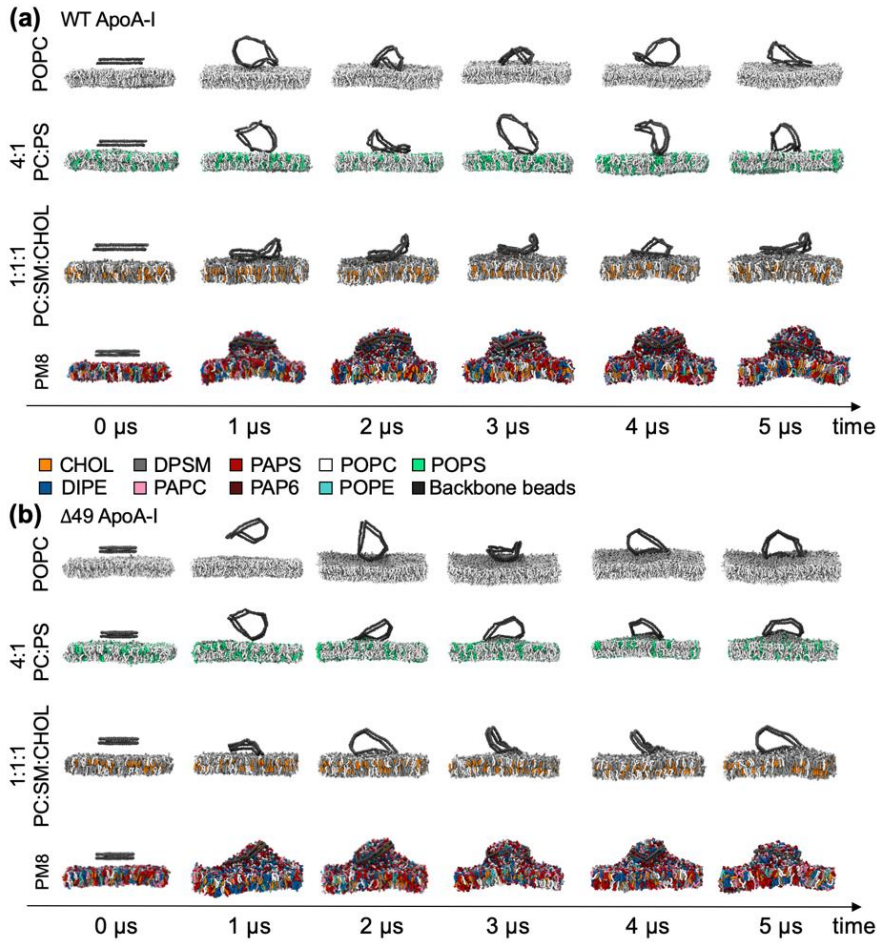

Figure 3.3: *Coarse-grained molecular dynamics simulations of the WT and Δ49 ApoA-I. The snapshots of* ***(a)*** *the WT ApoA-I and* ***(b)*** *Δ49 ApoA-I double-belt proteins in four different membranes are taken at every 1 μs throughout a single representative 5 μs-long simulation trajectory as indicated by the arrow; the first column of each row corresponds to the initial placement of the pre-assembled double-belt protein 4 nm away from the membrane surface. In the panels a and b, each row corresponds to a system containing a different membrane composition: from top to bottom, the systems include a 100% POPC, 4:1 POPC:POPS, 1:1:1 CHOL:DPSM:POPC and PM8 (mammalian plasma membrane model) membrane. The representative simulations shown here are carried out with the restraints ensuring double-belt proteins remain open and flexible. Lipids are color-coded: CHOL in orange, DIPE in blue, DPSM in gray, PAPC in pink, PAPS in red, PAP6 in dark red, POPC in white, POPE in cyan and POPS in green. Water and ions are not shown for clarity. Protein backbone beads are colored in dark gray.*

independent simulations. Particularly in simulations where the protein is restrained to remain flexible and open, the protein causes a bud-like deformation that is the most significant in comparison to the deformations observed in other membrane compositions.

These simulations were repeated with Δ49ApoA-I double-belt (**Fig. 3.3b**). Similar interactions with the POPC, POPC:POPS, POPC:DPSM:Chol and PM8 membranes were observed. The protein induced the most pronounced bud-like deformations in the PM8 membrane (**Fig. S3.5d**), and its interactions were subtly disruptive for 4:1 POPC:POPS membranes (**Fig 3.3b., row 2**) when compared to interactions by WT ApoA-I (**Fig 3.3a., row 2**).

Overall, the computational data show that ApoA-I interactions depend significantly on the lipid composition of the membrane in a way that the presence of negatively charged lipid species may help mediate embedding of the protein into the membrane surface. These MD simulations also show that ApoA-I exhibits long term association with these membrane compositions. Such an association time would be needed for the kinds of deformation we observe, experimentally. However, the simulations reveal only subtle morphological deformation in POPC, a variance with our observations of gross membrane remodeling which ensues upon peptide interaction with POPC GUVs. In contrast, when we substitute the single component membrane for a more complex, PM8, the full scope of morphological changes becomes apparent.

3.3.5 Δ49ApoA-I binding-induced phase separation in cholesterol-containing GUVs

The lipid specificity of ApoA-I interactions witnessed during the molecular simulations above raises some general questions: By sequestering and binding specific sub-classes of lipid molecules,

does Δ49ApoA-I sort the remaining pool of membrane lipids? Can the protein association break symmetry and transform multicomponent, homogeneous membranes into phase-separated states? These questions are not limited to Δ49ApoA-I but arise in broad classes of protein-membrane interactions where the preferential association of proteins with a sub-set of molecules locally can shift the phase space and drive global phase separation. To begin to explore these questions, we incubated a model ternary GUVs composed of an equimolar mixture (1:1:1) of POPC, SM, and Chol, with Δ49ApoA-I. To enable visualization of membrane phases by fluorescence, we doped the lipid mixture with small concentrations of two phase-sensitive lipid probes: (i) 1 mol % of Rho-DOPE (red, Ex/Em 560:583), which preferentially associates with the POPC enriched liquid-disordered phase (L_d), and (ii) 3 mol % NBD-PE (green, Ex/Em 463:536), which selectively partitions within cholesterol- and SM-rich, liquid-ordered (L_o) phase. Previous work has established that the presence of these probe lipids at these concentrations does not influence the phase behaviour of the dominant ternary lipid mixture (76).

A selection of images from the time-lapse movies (**Supplementary Video 4 & 5**) shown in **Fig. 4a** and **Fig. 4b** document how Δ49ApoA-I interaction transforms these multi-component GUVs. The GUV is imaged from a distal plane, capturing a confocal view of the apical hemisphere (away from the substrate), which initially appears homogeneous (**Fig. 4a 5:27**). After a short delay, following the addition of Δ49ApoA-1 (8:54), the uniform intensity along the perimeter of the membrane is abandoned, replaced by a pattern of small domains of high intensity of Rho-DOPE (red). In the subsequent several minutes (12:21), membrane domains elevated in NBD-PE intensity (green) form simultaneously with the complementary domains enriched in Rho-DOPE. These segments of the membrane continue to grow and increase in intensity while traversing to and

aggregating within the distal hemisphere of the vesicle, characterizing the incipient phase separation.

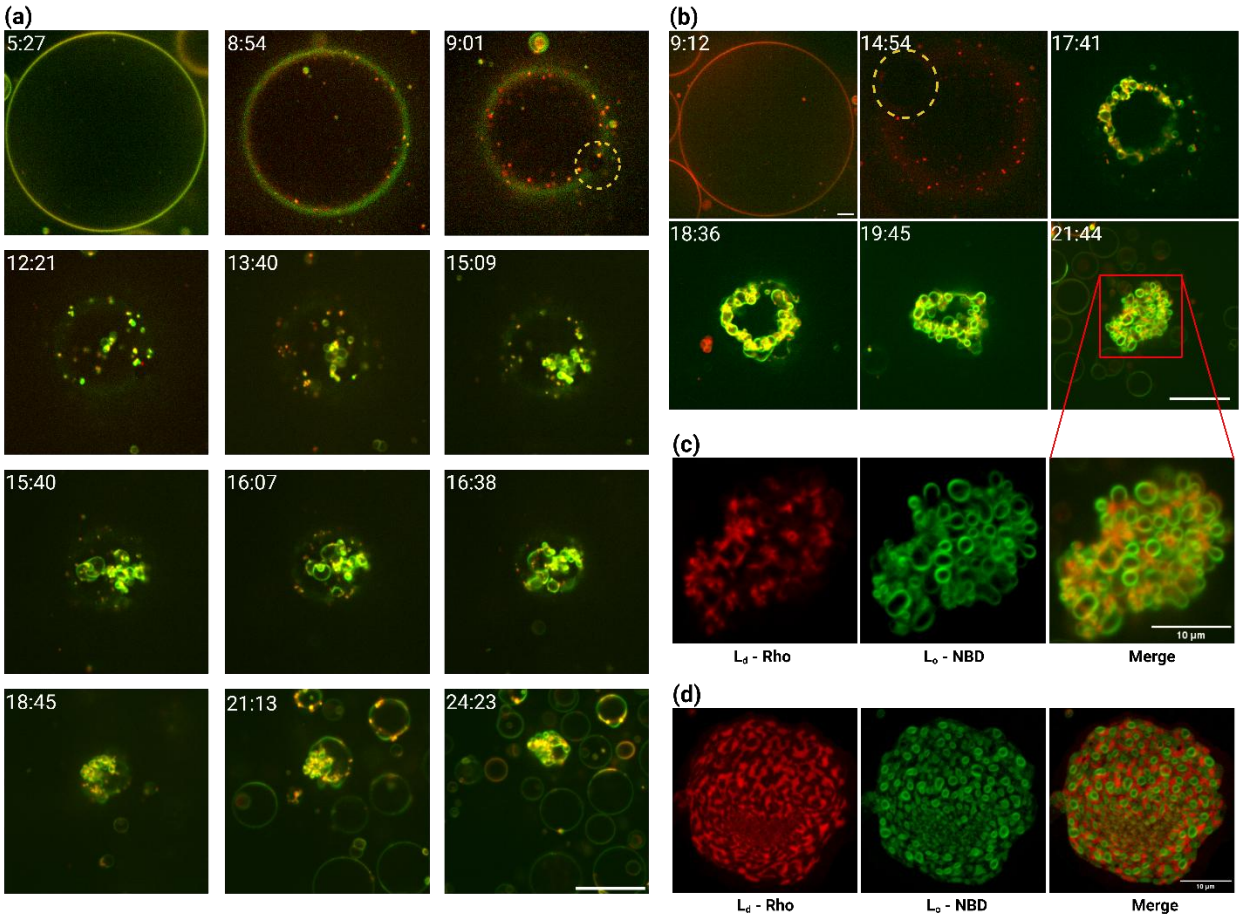

*Figure 3.4: Confocal xy-scans of vesiculation in equimolar GUVs composed of POPC, SM and Chol are doped with 1 mol % Rho-B-DOPE (L_d) **(red)** and 3 mol % NBD-PE (L_o) **(green)**. **(a)** Montage of **Supplementary Video 4** depicting phase separation and vesiculation following the introduction of ~3.5 µM Δ49ApoA-1. A pore can be seen to appear beginning at 9:01. Scale Bar 20 µm. **(b)** Montage of **Supplementary Video 5** viewing the upper hemisphere of the vesicle. Scale bar 20 µm **(c)** Channel split and merge of collection of vesiculated spheres from Figure 1. Clear maintained structure within the cholesterol-rich domain (green). Scale bar 10 µm.*

Instances of phase separation precede large-scale morphological remodeling of the membrane. In the minutes following the appearance of phase-separated domains (12:21), structures of high-

intensity NBD-PE (green) are observed to appear from the membrane. These structures appear circular and folded with an average diameter of ~2 μm. They also seem to colocalize with the smaller Rho-DOPE domains (**Fig. 3.4a (13:40) & Fig. 3.4b (17:41)**). Over the next several minutes, formation continues, transforming the GUV into a tightly associating cluster of spherical features (24:23). These observations are fully reproducible and observed in multiple independent experiments (**Supplementary Videos 3.4, 3.5 & 3.6**). Across these experiments, the size of these folded structures ranges from 0.3-4.6 μm in diameter, with a density average of ~0.2 μm^{-2}.

These localized substructures, which emerge at the membrane boundary (**Fig 3.4a.**), form by folding at the membrane, appear circular, and remain bound at the membrane surface – consistent with localized vesiculation. This vesiculation of multi-component GUVs reveals a striking separation of membrane lipid lipids (**Fig. 3.4c**). This effect is observed most conspicuously for 2:2:1 (POPC:SM:Chol) GUVs (**Fig. 3.4d**). Here, the NBD-PE label (green) indicates that the structured portion of the membrane domain is primarily composed of cholesterol-enriched, sphingomyelin (**Fig. 3.4c (L_o) & 3.4d (L_o)**), while the state of cholesterol-poor, POPC domains reveal no resolvable structure (**Fig. 3.4c (L_d) & 3.4d (L_d)**). Other examples of similar, 'colony-like' formations can be seen in **Figure S3.4**. This segregation of membrane lipids can be attributed to the differences in the bending moduli (*25*, *160*) of the two co-existing phases. For PC:SM:Chol membranes, the difference in bending rigidity between the liquid-ordered (red, κ_{L_o} = 6.4 ± 0.3 (*84*)) and the liquid-disordered (green, κ_{L_d} = 2.6 ± 0.4 (*84*)) membrane domains are reflected in the discrepancy between their structural appearance. The results are the complementary images we observe in **Figures 3.4c & 3.4d**.

It is notable that membrane domains form 1:1:1 POPC:SM:Chol GUVs at room temperature, following the introduction of Δ49ApoA-I. Under these conditions, the phase diagram predicts the absence of phase-separated domains at optical length scales (*75*). The appearance of phase-separated membrane domains can be understood as a consequence of the interaction between Δ49ApoA-I and GUV. Because the latter depletes lipids from the GUV membranes, the residual membranes accumulate lateral tension. It is known that beyond a critical value, lateral membrane tension can give rise to isothermal phase separation and poration (**Figure S3.1c**), occurring transiently during the equilibration of osmotically swollen GUVs (*26*). However, this mechanism produces pulsatory phase separation as a response to dynamic membrane tension – induced by transient poration. Therefore, this mechanism cannot explain the steady state phase separation we observe. Thus, one mechanism likely responsible for inducing membrane phase separation – membrane binding by ApoA-I. As an amphipathic α-helical protein, ApoA-I embeds partially into the outer leaflet of the lipid bilayer at the headgroup-water interface. This then creates localized regions of packing and curvature stress (*161*), which relieve the elastic energy by driving membrane phase separation.

Membrane interaction with amphipathic α-helical adopting peptides have long reported curvature generation in BAR domains (*28*, *29*), GTPases (*30*), annexin B12, α-synuclein (*31*) and clathrin (*32*). Our experiments suggest that Apolipoprotein interaction with a vesicular membrane leads to curvature generation (**Fig. 3.1a & 3.1b**). The physical space of the peptide acts as a wedge within membrane, supported by the presented coarse-grained MD simulations depicting ApoA-I association with the outer leaflet of varying membrane compositions (**Fig. 3.3a & 3.3b**). Insertion by the helical segments of ApoA-I into a mixed lipid membrane induces localized region of altered

lipid curvature, packing and composition (161), reported to create microdomains capable of separating lipid species into CO-EXISTING liquid phases (162). A cooperative effect of ApoA-I peptides could lead to the instances of micro-scale domains, of which we observe.

Alternatively, we must consider that the biological function of HDL and ApoA-I is the removal of cholesterol from the cell through reverse cholesterol transport (RCT) (111). If, in the process of forming HDL-like particles, ApoA-I participates in the preferential removal of cholesterol from GUVs comprised of POPC, egg-SM, and cholesterol in an equimolar ratio, the phase diagram predicts a shift in the membrane state towards a two-domain mixture (163). Either or both the cooperative effect of the α-helical peptide disruption and the selective removal of cholesterol could be responsible for the sorting of the membrane lipids into the observed membrane domains.

3.4 Conclusion

In this work, we monitor the interactions between a truncated isoform of ApoA-1 (Δ49ApoA-I) and lipid bilayers organized as giant unilamellar vesicles. We find that morphological transformations of the parent lipid bilayer *en route* to the reconstitution of HDL-like particles *in vitro* result in gross membrane remodeling, which includes the formation of transient, microscopic pores, solute leakage, and vesiculation. The formation of these pores is typical in instances of membrane tension, likely occurring from the physical removal of lipids from the GUVs membrane by Δ49ApoA-I concomitant with nano lipoprotein particle formation. Subsequently, solute leakage through these physical breaks in the membrane is observed to occur over a timeframe beyond the lifetime of individual instances of pore formation, indicating the presence of a cascade of pore formation events. Furthermore, Δ49ApoA-I interaction results in an energetically driven

restructuring of the vesicle membrane into smaller, more stable daughter vesicles, concomitant with NLP formation. We propose this observed vesiculation phenomenon is a result of the interfacial alpha-helical peptides embedding into the membrane, forming smaller vesicles upon the lysis of the GUV. Wildtype ApoA-I, ApoE-3, and ApoE-4 additionally show these structural changes when introduced to 4:1 DOPC: POPS membranes, showing this behavior is not limited to the ApoA-I isoform or its Δ49 truncated variant. This lipid selective behavior is additionally observed through a series of coarse-grained molecular dynamic simulations. Introducing Δ49ApoA-I to a collection of equimolar GUVs composed of POPC, egg-sphingomyelin, and cholesterol results in the appearance of micro-phase separated domains, likely occurring through either a cooperative effect by ApoA-I in altering local lipid curvature or by the preferential removal of cholesterol from the vesicular membrane *en route* to HDL-like particle formation.

Funding

This work was performed, in part, under the auspices of the U.S. Department of Energy by Lawrence Livermore National Laboratory under Contract DE-AC52-07NA27344. Support for WH, TNO, YW, AN TSC and MAC was provided by the LLNL Laboratory Directed Research and Development program (21-ERD-047). LLNL-JRNL-2001736. Contributions of ANP and CFC were supported by a grant from the National Science Foundation through the award: Biomaterials program, division of materials research, National Science Foundation (2342436).

Acknowledgements

A.N.P & C.F.C acknowledge the preparation of WT ApoA-I, ApoE-3 and ApoE-4 for these experiment by the J.V. lab and graduate student, Maha Al-Habeeb. A.N.P & C.F.C acknowledge the microscopy facilities provided by the UC Davis LMC. T.S.C & T.N.O thank Livermore Computing and the Livermore Computational Grand Challenge for computing time. Figures were assembled, in part, utilizing the online tool Biorender.

Declaration of Interests

The authors declare no competing interests.

3.5 Materials and Methods

Materials

1-palmitoyl-2-oleoyl-sn-glycero-3-phosphocholine (POPC), 1,2-dioleoyl-sn-glycero-3-phosphocholine (DOPC), 1-palmitoyl-2-oleoyl-sn-glycero-3-phospho-L-serine (sodium salt) (POPS), egg-sphingomyelin, Cholesterol, and lissamine rhodamine B 1,2-dioleyl-sn-glycero-3-phosphoethanolamine (Rho-B DOPE) were acquired from Avanti Polar Lipids (Alabaster, AL). Glucose was obtained from Sigma-Aldrich (St. Louis, MO), and 2-deoxy2-[(7-nitro-2,1,3-benzoxadiazol-4-yl) amino]-D-glucose (2-NBDG) was obtained from Cayman Chemical (Ann Arbor, MI). Sucrose was obtained from EMD Chemicals (Philadelphia, PA). Chloroform, head-labeled N-(7-nitrobenz-2-oxa-1,3-diazol-4-yl)-1,2-dihexadecanoyl-sn-glycero-3phosphoethanolamine, triethylammonium salt (NBD-PE) and head labeled Texas Red™ 1,2-dihexadecanoyl-sn-glycero-3-phosphoethanolamine, Triethylammonium Salt (Texas Red™

DHPE) was obtained from Thermo Fisher Scientific (Waltham, MA). Δ49Apolipoprotein A-1 was provided by the Lawrence Livermore National Laboratory (Livermore, CA). Wildtype Apolipoproteins A-1, E-3 and E-4 were provided by the John Voss lab.

Glass-bottom, 96-well plates were obtained from Cellvis (Mountain View, CA). Indium tin oxide (ITO)-coated glass slides (5-25 Ω) were obtained from Delta Technologies, LTD (Loveland, CO). Manual Teflon-tipped syringes were obtained from Agilent Technologies (Santa Clara, CA).

3.5.1 Preparation of synthetic model membranes

GUV preparation via electroformation is a well-established process (*13*, *103*). A lipid stock of a desired composition at a concentration of 2 mg/mL is prepared in chloroform. For single component synthetic membranes, POPC (99 mol %) is dissolved with a Rho-B DOPE label (1 mol %). Cholesterol containing membranes are prepared with a combination of POPC, egg-Sphingomyelin, and Cholesterol with the fluorescent labels of Rho-B DOPE (L_d domain) and NBD-PE (L_o domain) at a molar ratio of either 32:32:32:1:3 or 38.4:38.4:19.2:1:3, respectively. DOPC:POPS or DOPC:DOPS lipid mixtures are doped with prepared with Rho-B DOPE label at a molar ratio of 79:20:1. For all lipid stock, 15 µL is deposited onto the conductive side of two ITO-coated slides and spread evenly on half of the slide as it evaporates. These slides are further dried inside a vacuum desiccator from anywhere from 2 – 24 h. Once dry, a chamber is formed using a 1-mm-thick rubber O ring (Ace Hardware, Davis, CA) and sealed with high-vacuum grease (Dow Corning, Midland, MI). After the O ring is adhered to the conductive side of the ITO-slide, the chamber is hydrated with ~1 mL of a 100 mM Sucrose solution. The chamber is sealed with the second, inward facing lipid cake, ITO-slide ensuring no trapped air bubbles. The two slides

form the chamber in a way that the halves without dried lipid are facing in opposite directions to avoid the alligator clips from the function generator from touching both slides, effectively forming a less resistant pathway for any current. A 2.2 V(pp) AC Sine wave is applied across the two slides at a frequency of 10 Hz for 1 h, followed by another 2.2 V(pp) AC Sine wave at a frequency of 2 Hz for 30 minutes. Vesicles containing egg-SM undergo this step at a temperature of 55 °C. All samples undergo this step covered to protect from light. After GUV formation, the chamber is disassembled, and the solution is pipetted into a small centrifuge tube and stored at 4 °C. Vesicles prepared are either used or discarded within a week of preparation.

3.5.2 Preparation of Δ49ApoA-I and WT Apolipoprotein

Cell-free synthesis of Δ49ApoA-I protein:

Cell-free reactions were set up using RTS 500 ProteoMaster *E. coli* HY Kit (Biotechrabbit GmbH, Hannover, Germany). Reaction components (lysate, reaction mix, feeding mix, amino acid mix, and methionine) were combined as specified by the manufacturer. Each 1 mL reaction contained 15 µg Δ49ApoA-I plasmid DNA and 20 µL FluoroTect™ GreenLys tRNA (Promega, Madison, USA). The reactions were incubated at 30 °C, with shaking at 300 rpm for 18 h in a floor shaker. After the reaction, ApoA-I protein is purified using nickel affinity chromatography. Briefly, 1 mL of 50% slurry complete His-Tag Purification Resin (Roche Molecular Diagnostics, Basel, Switzerland) was equilibrated with equilibration buffer (50 mM NaH_2PO_4, 300 mM NaCl, pH 8.0) with 10 mM imidazole (Sigma-Aldrich, St Louis, MO) in a 10 mL chromatography column. The total cell free reaction was mixed with the equilibrated resin and was incubated/nutated at 4 °C for 1 h. The column was then washed 6 times with 1 mL wash buffer containing (50 mM NaH_2PO_4,

300 mM NaCl, 20 mM imidazole, pH 8.0). ApoA-I is eluted with 6 x 300 µl elution buffer (50 mM NaH_2PO_4, 300 mM NaCl, 250 mM imidazole, pH 8.0). All elutions were analyzed by SDS-PAGE and peak fractions containing labeled protein were combined. Pooled fractions were dialyzed in PBS (pH 7.4) and then stored at 4 °C. Protein levels were quantified using a Qubit protein test according to manufacturer's instruction (Thermo Fisher Scientific, Carlsbad, CA).

Production and Purification of ApoA-I protein

Human ApoA-I was expressed in *Escherichia coli* strain BL21 Star (DE3)pLysS cells (Life Technologies, Carlsbad, CA, USA) from the human ApoA-I gene containing a hexa-His affinity tag at the N-terminus. The ApoA-I gene was cloned into the pEXP-5 plasmid (Novagen, Inc, Madison, WI, USA) and transferred into the bacteria and cultivated at 37^{o}C in LB medium with 50 µg/mL of ampicillin and 34 µg/mL of chloramphenicol. Protein expression was induced for 3-4 h following the addition of 0.5 mM isopropyl-beta-thiogalactopyranoside (Sigma, St Louis, MO, USA). Following cell disruption, ApoA-I was purified from the soluble fraction of the cells using a His-Trap-Nickel-chelating column (GE Healthcare, Uppsala, Sweden) and a mobile phase of phosphate-buffered saline (PBS), pH 7.4 with 3 M guanidine. The protein was washed in PBS (pH 7.4) containing 40 mM imidazole and then eluted with PBS containing 500 mM imidazole. Imidazole was removed from the protein sample by dialysis (10K MWCO Slide-A-Lyzer, ThermoFisher) equilibrated with PBS, pH 7.4. Protein purity was analyzed by SDS-PAGE and concentration was determined using a Nanodrop 2000c spectrophotometer (Thermo scientific, Waltham, MA, USA), which was based on the extension coefficient (32,490 l $mol^{-1}cm^{-1}$) and molecular weight (28,279 Da) of ApoA-I.

Production and purification of ApoE protein

Human ApoE-3 or ApoE-4 protein was expressed in *Escherichia coli* cells and purified as described previously (*164*). Briefly, one liter of cells in LB broth were grown to mid-log phase at 37 °C. These were then induced with 0.1% arabinose, and incubated for an additional 4h at 37°C. The cells were harvested by centrifugation, and inclusions bodies isolated and washed as described previously (*165*). To purify the protein, washed inclusion bodies were dissolved in 8 M urea, 200 mM NaCl, and the sample filtered through a 0.2 µm filter and then chromatographed on a SuperDex 200 (Pharmacia) size exclusion column using a mobile phase of 8M urea, 200 mM NaCl, 10mM TRIS (pH 7.5) and 1 mM EDTA. The fraction was then desalted using a SuperDex 200 column using a mobile phase of 8M urea, 10 mM TRIS (pH 7.5) and 1mM EDTA and then bound to a mono-Q ion exchange column. The column was washed with 8 M urea,10 mM TRIS (pH 7.5) and 1 mM EDTA, and the protein eluted using a gradient of NaCl. The protein was then re-folded by dialysis (Slide-A-Lyzer, ThermoFisher) against 0.1M ammonium bicarbonate and then PBS buffer pH 7.4. The sample was concentrated using centrifugal spin concentrators with a molecular size cutoff of 30 kDa (Millipore), and the protein concentration determined using the Pierce BCA kit (ThermoFisher, USA).

3.5.2 ApoA-I incubation Assays

GUV incubation with Apoprotein

All spinning-disk confocal fluorescence imaging was taken in conjunction with glass-bottom, 96-well plates (Cellvis). Experiments observed in this way have a final volume of 100 µL per well. 2 µL of GUV solution prepared in a 100 mM sucrose solution are added to a bath of osmotically

balanced, 100 mM Glucose solution. The difference in density of the GUVs allows them to settle on the bottom of the well. Control experiments are imaged in these conditions, otherwise 1-5 μM Δ49ApoA-I, WT ApoA-I or ApoE-4 is added by micropipette slowly (3-5 s) and gently to the center of the well.

GUV leakage assay

GUVs containing soluble dye are prepared as described above; Slides are hydrated with a 100 mM Sucrose & 100 μM of 2-NBDG dye before the electroformation step. Both POPC and cholesterol containing GUVs are prepared in this way. When observing the leakage of dye from the inside of GUVs, incubation with ApoA-I follows the above-described method. When observing the leakage of dye from extracellular space, the bath is instead prepared with 100 mM Glucose & 100 μM 2-NBDG followed by the introduction of GUVs prepared in only 100 mM Sucrose. Spinning-disk confocal fluorescence imaging with 488 nm & 561 nm lasers were used simultaneously to observe any ApoA-I-induced leakage between the intra- and extracellular space. The difference in fluorescence intensities between these spaces is used for quantification of the leakage over time.

Coarse-grained molecular dynamics simulations

The sequence of human ApoA-I was taken from Uniprot database (Entry P02647 (*166*)) and used as an input to *Nanodisc Builder* (*167*) in order to generate an atomistic structural model for the ApoA-I double-belt, referred as WT. The mutant sequence where first 49 residues were deleted was also fed into *Nanodisc Builder* to generate a model for the Δ49ApoA-I double-belt, referred as Δ49. Next, the atomistic models were converted to coarse-grained structural models using *martinize2* with Martini 2.2 force field parameters (*168*, *169*). The elastic network was added to the

structures with a force constant of 900 kJ/mol/nm^2 and a lower (upper) distance cutoff of 0.5 nm (1.2 nm). A 30 nm x 30 nm POPC, 4:1 POPC:POPS, 1:1:1 POPC:DPSM:CHOL, or PM8 bilayer was built with *Insane* (170) and solvated with 0.15 M NaCl and 10% antifreeze water (WF) beads; these systems included the coarse-grained WT and Δ49 belt proteins placed 4 nm away from the membrane. PM8 membrane was set as a symmetric bilayer with the lipid composition of the inner leaflet composition of a typical mammalian plasma membrane model used in a previous study (171) and included 13.9% POPC, 7.5% PAPC, 5.4%POPE, 16.1% DIPE, 10.8% DPSM 28% CHOL, 16.1% PAPS and 2.2% PAP6.

For each membrane composition, we carried out three independent simulations for 10 μs, 5 μs and 5 μs using the protocol presented by Ozturk et al. (172). We carried out these simulations twice: the one set with restraints on the ApoA-I belt dimers and the other set without any restraints. The first set had two distance restraints that were only in effect if the distances became smaller than 8 nm in WT ApoA-I and 6 nm Δ49, respectively, with a force constant of 1000 kJ/mol/nm^2. Two distance variables were defined using the geometric centers of the residues (1) 110-112 and 250-252 and (2) 280-282 & 410-412 for the WT ApoA-I model and (1) 80-82 and 190-192 and (2) 300-302 and 410-412 for the Δ49 ApoA-I model. These restraints did not allow for full closing-up of the belt but still allowed for large conformational changes. The temperature and pressure were kept at 310 K and 1 bar with v-rescale thermostat (173) and c-rescale barostat (174) during the production runs as indicated in a previous work (172) and are listed in the Supplementary Table 1. Note that LINCS order and iteration were set to 12 and 2 which are crucial when cholesterol is modeled with Martini 2.2 force field parameters with a time step of 20 fs (175). As suggested in a recent study, to avoid unphysical distortions in the membrane, the outer cutoff and timesteps

between neighbor list updates were set to 1.35 nm and 20 (176). All coarse-grained molecular dynamics simulations were carried out with Gromacs 2024.4 (177) and the restraints were applied using the Colvars module (178). The simulation snapshots were generated with VMD (179).

3.6 Characterization

3.6.1 Fluorescence microscopy

Spinning-disk confocal imaging and measurements were collected on an Intelligent Imaging Innovations Marianas Digital Microscopy Workstation (3i, Denver, CO) with attached CSU-X1 spinning-disk head (Yokogawa; Mushanino-shi, Tokyo, Japan), a Quantem512SC EMCCD camera (Photometrics, Tucson, AZ) and a Flash 4 ORCA-sCMOS camera (Hamamatsu, Hamamatsu-city, Japan). A Zeiss Plan-Fluor 63x (NA 1.4), oil immersion objective (Carl Zeiss, Oberkochen, Germany) was used in the collection of these data. Rho-B DOPE (Ex/Em 560:583) was exposed with a 50 mW 561 nM laser line, while NBD-PE (Ex/Em 463:536) and 2-NBDG (Ex/Em 465:540) were exposed with a 50 mW 488 nM laser line. Image processing was done using Fiji a public-domain software; https://imagej.net/software/fiji/), Slidebook digital microscopy imaging software (3i), and MatLab (The Math Works, Inc. MATLAB Version 2023a).

3.6.2 Size Exclusion Column Purification (SEC)

The NLPs are analyzed and purified via size exclusion chromatography (SEC) with a semi-preparative Superose 6 10/300 column (GE Healthcare). SEC was run on a Shimadzu LC-20 HPLC system (Shimadzu) at flow rate 1mL/min with PBS as running buffer. NLP peak was assessed using absorption at 280 nm and analyzed with instrument software LC Solutions (Shimadzu).

3.6.3 High-Speed AFM characterization of reactant NLPs

A high-speed atomic force microscope (RIBM, Japan) was equipped with a small cantilever (Ultra-Short Cantilevers (USC, NanoWorld): spring constant, $k = 0.15$ N/m, resonance frequency, $f = 1200$ kHz in water) and was operated in tapping mode at room temperature. The free oscillation amplitude was $0.9 \sim 1.3$ nm, and the typical set-point amplitude was 85% of the free oscillation amplitude. For the sample stage, a freshly cleaved mica disk with a diameter of 1.5 mm was fixed on a glass rod with a diameter of 1.5 mm and a height of 2 mm using epoxy glue. The SEC-purified NLPs was diluted 20x in PBS buffer, and 2ul of the diluted solution was deposited onto the freshly cleaved mica and incubated for 10 minutes. The scanner was then mounted above the sample chamber with the cantilever immersed in PBS buffer. HS-AFM images were processed using ImageJ (National Institutes of Health, Bethesda, MD, USA). The height and width dimensions of each nanodisc were analyzed with Gwyddion software (*180*) and the data was plotted with Origin.

Chapter 4

Preliminary results of Engineered Compositional Asymmetry within nascent HDL-like Particles

4.1 Introduction

In previous chapters 1 & 2 we discussed both the ability of mβCD to exchange lipid and sterols from the outer leaflet of synthetic giant vesicles as well as how Apolipoproteins produce nascent, discoidal HDL from the membrane of GUVs. In this chapter, we will discuss the union of these previous chapters. This entails application of mβCD as a means to synthesize artificial, tailor-made membrane asymmetry in synthetic cells, followed by the reconstitution of HDL particles that maintain this engineered asymmetry. These preliminary results serve as a platform for future studies, utilizing compositional membrane asymmetry within nanodiscs as both a proof-of-concept

in addition to a tool for reconstituting complex integral proteins for structural analysis utilizing NMR or EPR techniques.

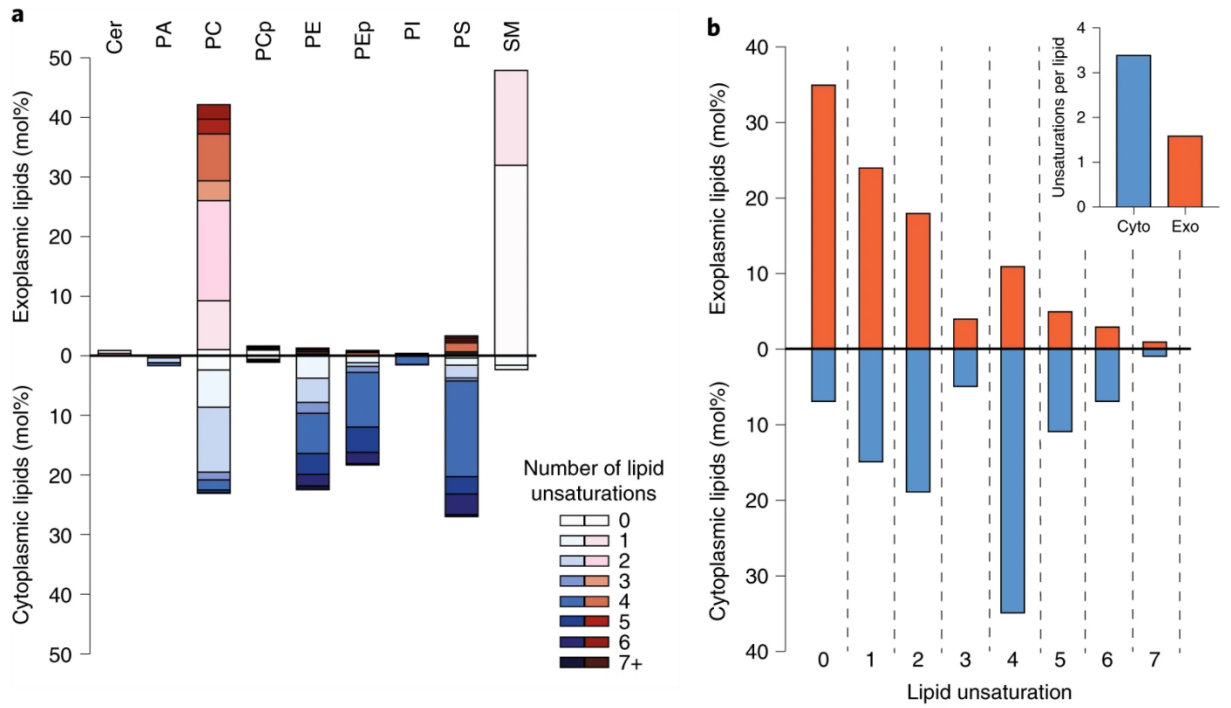

***Figure 4.1**: **a)** Phospholipid compositions of exoplasmic (red) and cytoplasmic (blue) PM leaflets as defined by enzymatic digestion and MS. The exoplasmic leaflet is almost exclusively composed of PC and SM, while the inner leaflet is approximately equimolar between PC, PE, PS and PEp. **b)** Leaflet asymmetry of acyl chain unsaturation. The plurality of phospholipids in the exoplasmic leaflet are fully saturated, whereas the majority of the cytoplasmic leaflet is polyunsaturated. Inset: abundance-weighted average unsaturation is approximately twofold greater for cytoplasmic leaflet phospholipids. Adapted from Ref. (181).*

Compositional membrane asymmetry is the difference in the types of lipid species present between leaflets within the cell membrane (**Fig. 4.1**). Biological membranes are almost universally

asymmetric (182), and some believe to be the simplest requirement to define life. Asymmetry created by differing lipid acyl chain length, saturation state, head and backbone composition, as well as chirality are maintained through ATP-dependent flippases and free energy driven scramblases – a substantial energetic cost to the cell in terms of ATP and protein synthesis is devoted to maintenance of a consistently energetically unfavorable membrane state. This cost is a necessary expenditure for the cell, as membrane asymmetry dictates directionality required for proper integral protein insertion (183) and cell-cell signaling (184).

Integral membrane proteins are one of the most challenging targets in structural biology. Despite making up ~25% of all proteins, less than 150 unique structures of are solved – less than 1% of the Protein Data Bank (PDB) repository represent membrane proteins. The lack of available structures is a result of the difficulties that accompany visualizing nano-scale peptides within their partially hydrophobic environments, while additionally flexible and conformationally diverse. Unraveling the complexities of these peptides is of such importance, many go on to receive Nobel prizes for their work in doing so (185-189).

In recent years, techniques used to decipher three-dimensional structures have evolved – a recent advancement being the usage of nanodiscs as a means to reconstitute integral proteins for structural studies (127, 128). This development in technology has provided an important advantage in deciphering integral protein structure, through improvements to isolation, purification, structural resolution, and functional characterizations. While lipid composition is controllable in the preparation nanodisc particles, reconstituting compositional asymmetry has not yet been achieved

– not to mention the difficulties associated with characterizing membrane asymmetry. Furthermore, synthesis of nanodiscs from natural-occurring cell membranes that maintain asymmetry fall prey to the lipid-specific behavior exhibited by scaffold proteins, as shown in Chapter 3 in regard to Apolipoproteins. These shortcomings limit the range of integral proteins capable of being suspended within the nanodiscs bilayer. In this Chapter, I will share the results of utilizing a known technique to synthesize tailor-made asymmetry in vesicles, and preliminary indications that this asymmetry is maintained when reconstituting HDL-like particles.

4.2 Compositional Asymmetry through mβCD Lipid Exchange

Methyl-β-cyclodextrin (mβCD) is class of oligosaccharide composed of cyclically bound D-glucose molecules. This molecule's unique structure produces a particle capable of solubilization in aqueous environments despite housing a hydrophobic cavity within its lumen. This non-polar cavity has been widely used as a means of solubilizing various hydrophobic molecules, namely sterols (*86*), and at high concentrations, mβCD was observed to bind and solubilize lipids (*87*), modifying the composition of a membrane through a lipidic exchange with individual leaflets within the bilayer (*59*). Observation of this behavior led researchers (such as Erwin Londen, et al.) to utilize cyclodextrin in a creative way – by modulating the lipid composition of a membranes extracellular leaflet to create tailored compositional asymmetry in synthetic vesicles (*55*, *57*). Compositional asymmetry generated in this way is relatively stable, as a result of minimal phospholipid transversal diffusion (flip-flop, 10^{-15} s^{-1} (*88*)). Here, we utilize mβCD in the same manner proposed by Erwin Londen, et al., to both verify and modify preparation of membrane asymmetry in GUVs.

4.2.1 Supported Lipid Bilayer Cholesterol Exchange

The first step in approaching membrane asymmetry involves analysis of mβCD's ability to deposit lipids onto a supported lipid bilayer – as we have already shown that mβCD can selectively remove lipids from the outer leaflet of a bilayer, in Chapter 2. Here, we prepare a single component, supported lipid bilayer from the phospholipid 1-palmitoyl-2-oleoyl-sn-glycero-3-phosphocholine (POPC) doped with 3 mol% Rho-PE, and measure the lipid's fluidity through a diffusion assay by recording fluorescence recovery after photobleaching (FRAP) to determine if mβCD lipid exchange is effective.

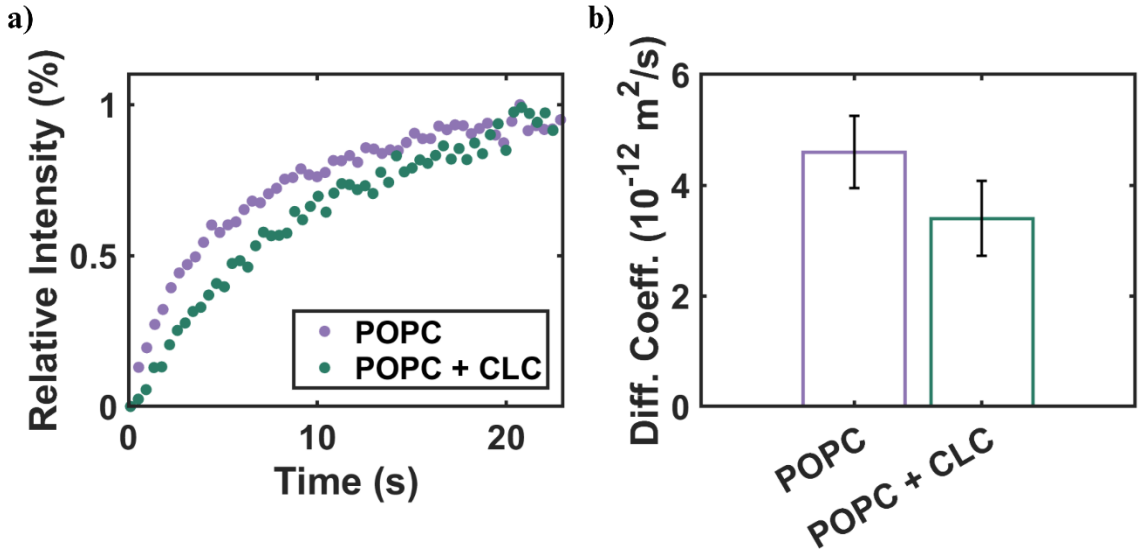

***Figure 4.2**: **a)** Relative fluorescence Intensity recovery after photobleaching a supported lipid bilayer composed of POPC and again in the same bilayer after treatment with cholesterol loaded cyclodextrin. **b)** Diffusion coefficient of POPC GUV before and after treatment with cholesterol loaded cyclodextrin. A significant decrease in fluidity is measured, likely as a result of an increase in cholesterol content within the membrane. Reproduced from Chapter 2, figure 1.2c.*

Following the addition of 1 mM of cholesterol loaded cyclodextrin (CLC), the fluorescence recovery of a supported membrane is substantially slowed (**Fig. 4.2a**). Furthermore, in Chapter 2, we showed that incubation of POPC GUVs with 1 mM CLC results in a decrease in lipid diffusion from a control of $4.5 \pm 0.7 \times 10^{-12}\ m^2/s$, to $2.7 \pm 0.2 \times 10^{-12}\ m^2/s$ (**Fig. 4.2b**) This constitutes a ~40% decrease in lipid diffusion, likely due to an increase cholesterol content within the membrane.

4.2.2 Giant Unilamellar Vesicle Biotin-PE exchange

We have verified mβCD's ability modulate membrane fluidity through the deposition of cholesterol onto both a supported and vesicular membrane. The next step is to determine whether mβCD can effectively exchange more complex lipids species. Here, we incubate POPC GUVs doped with 3 mol% Rho-PE with 1 mM of mβCD preloaded (3:1 = CD:lipid) with a biotinylated lipid, 1,2-dipalmitoyl-sn-glycero-3-phosphoethanolamine-N-(biotinyl) (sodium salt) (biotin-PE) (**Fig. 4.3a**). Interestingly, once incubated, POPC GUVs are observed to exhibit phase domains of complementary membrane arcs of labeled and unlabeled membrane domains. The reason for this separation unknown (potentially related to the biotinylated headgroups) and is not the focus of this report. GUVs are incubated with the mβCD:biotin-PE complex for 1 minute before halting the interaction by exchanging the bath with an isomolar solution.

GUVs prepared this way remained stable throughout an observation period of ~30 minutes. Following this period of observation, 0.05 mg/ml of a FITC-labeled streptavidin (SA) were introduced to the GUV solution. Interaction between biotin and SA is one of the strongest non-

covalent instances of binding found in nature – having an association constant of ~10^{15} (*190*). If biotinylated-PE was effectively introduced into the vesicular membrane, the labeled SA in solution will bind to- and fluoresce from the surface of the membrane. This is what we observe (**Fig. 4.2b**) – FITC labeled domains of the GUV's membrane distinct and complementary with the rhodamine labeled regions of the membrane surface. These observations indicate effective Biotin-PE exchange into the GUV membrane has occurred, and FITC-SA has bound and labeled these domains within the membrane.

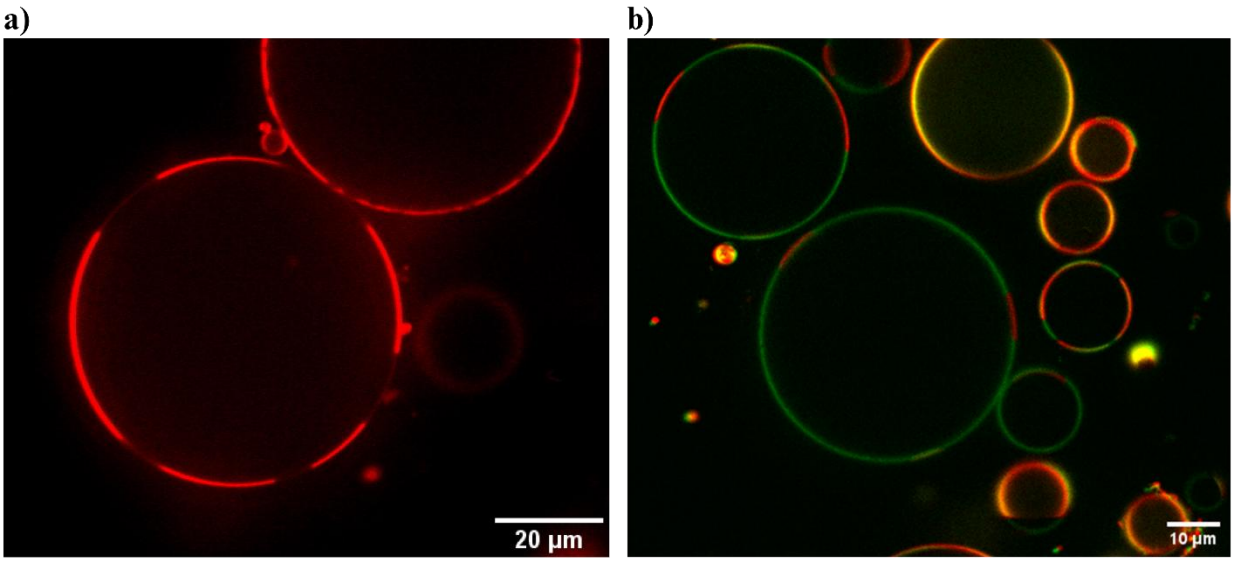

***Figure 4.3**: **a)** Confocal xy-scan of POPC GUVs doped with 3 mol% of Rho-PE following treatment with 1 mM CLC. Reasons for the appearance of domains depleted of rhodamine label are unknown, and not the focus of this manuscript. **b)** GUVs treated with 1 mM CLC following the introduction of 0.05 mg/ml FITC-streptavidin, labeling complementary regions of the GUV labeled with Rho-PE, indicating binding to biotinylated-PE lipids deposited into the vesicular membrane through mβCD lipid exchange.*

4.3 Engineered compositional Asymmetry in nHDL

We have shown preliminary results indicating exchange of biotinylated-PE lipids with POPC GUV through mβCD lipid exchange were successful. In Chapter 3 we showed that nHDL-like particle formation from vascular membranes composed of POPC is possible – here we assay whether nHDL-like particles formed from GUVs treated by mβCD lipid exchange are compositionally asymmetric.

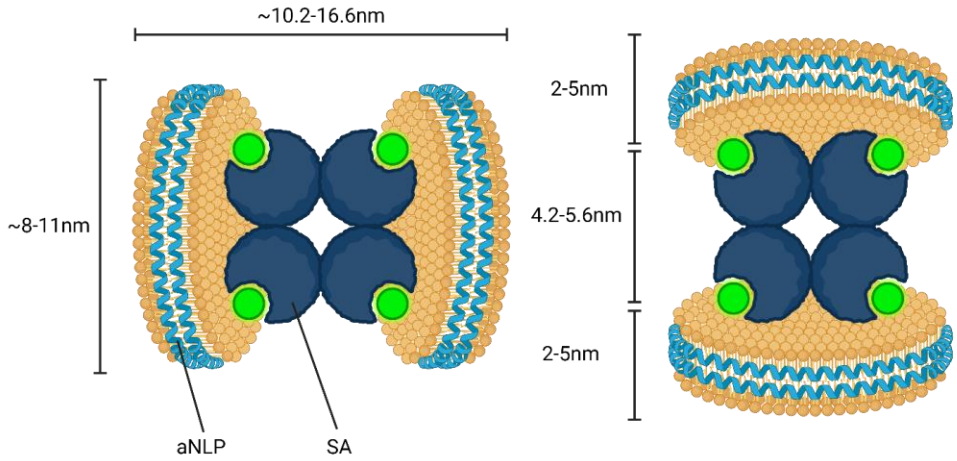

Figure 4.4*: Diagram of streptavidin bound, nHDL dimer complex. Due to the geometry of streptavidin, biotin-PE and nHDL particles, nanodiscs with engineered, asymmetric incorporation of biotinylated-PE lipids into a single leaflet of the bilayer will form a dimer structure when bound to the tetrameric structure of streptavidin's binding sites.*

Lipid exchange of biotin-PE with the outer leaflet of a POPC GUV is difficult to quantify, often requiring highly advanced techniques to confirm membrane asymmetry such as combinations of NMR (*191*), GC-MS (*192*), HPTLC (*193*), or lipid-specific approaches with zeta potential of negatively charged lipids or TMA-DPH. Here, we utilize a geometric approach: Formation of nHDL-like particles that maintain asymmetry prepared in GUVs by exchanging the outer vesicle

leaflet with biotinylated-PE should form dimer-like complexes upon the introduction and binding of free SA in the solution (**Fig 4.4**). Alternatively, if biotin-PE asymmetry is not maintained through the process of nanodisc formation, or was not initially engineered through mβCD exchange, biotin-PE would not be limited to a single leaflet and would form a stacked nHDL complex when binding with SA. Finally, if biotin-PE was not at all exchanged into the vesicular membrane, nHDL's would form no complex structure and simply maintain a singular, discoidal structure.

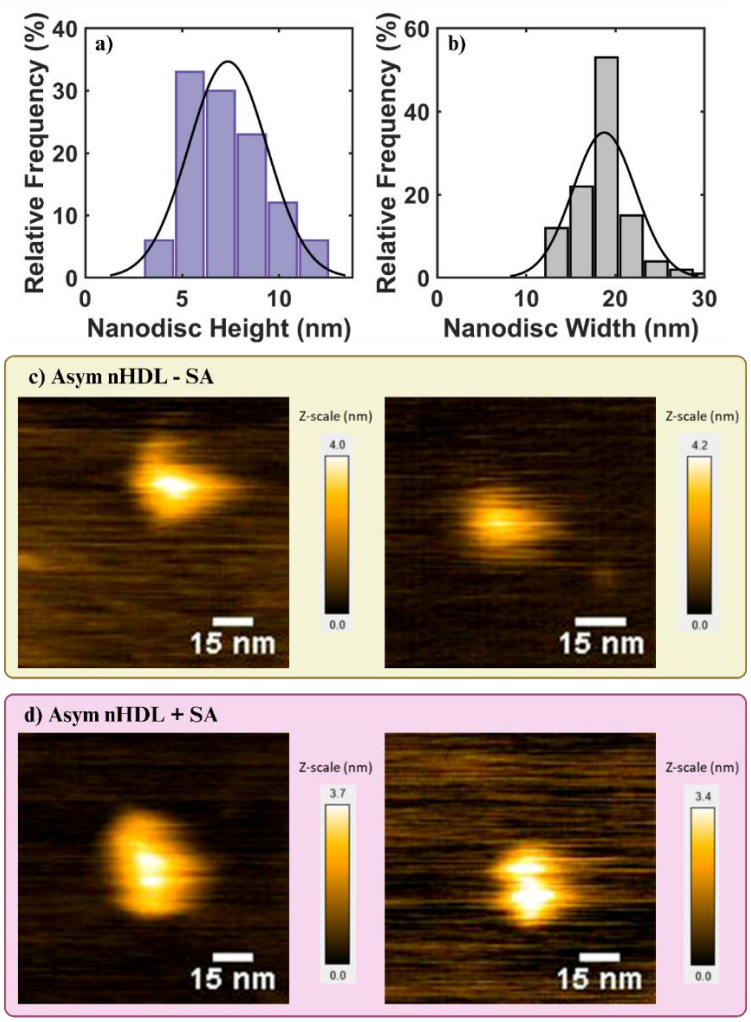

***Figure 4.5**: Relative histogram of discoidal structure **a)** height, and **b)** width formed from GUV's incubated with 1 mM Biotin-PE loaded mβCD (3:1 = CD:Biotin-PE). **c)** AFM images depicting*

single nanodisc appearance, and d) AFM images following the addition of 2.16 μM of SA (~1/4 molar ratio with Δ49ApoA-I) depicting nanodisc-dimer complexes.

GUV's incubated with 1 mM Biotin-PE loaded mβCD (3:1 = CD:Biotin-PE) are isolated through an isomolar bath exchange (GUVs encapsulate 100 mM sucrose, rendering them higher-density than the 100 mM glucose bath, therefore separating from the bulk solution). 100 μM of the vesicle solution is then incubated with 8.325 μM of Δ49ApoA-I for 1.5 hours at 4°C. After incubation, size exclusion chromatography (SEC) is used to purify and fractionate nHDL-like particles from mixture. Isolated nanodiscs are then imaged with high-speed atomic force microscopy (HS-AFM), finding single discoidal structures with height of $7.3 \pm 2.0\,nm$ and width of $18.7 \pm 3.5\,nm$ (**Fig. 4.5a & 4.5b**), within the expected dimensions of nHDL particles (**Fig. 4.5c**). Finally, the fractionated nHDL solution is incubated with 2.16 μM of SA (~1/4 molar ratio with Δ49ApoA-I) for 30 minutes before imaging with HS-AFM. Structures imaged from this solution appear to have dimer structure (**Fig. 4.5d**). Notably, the dimensions of these structures are not what was predicted in figure 4.4. This is likely due to the low lipid:Δ49ApoA-I ratio in this experiment, in which scaffold proteins form a saddle-shaped double belt structure to accommodate smaller lipid concentrations (*194*). In this model, lipids may point outward – bound together by SA, the observed dimer structures are consistent.

The appearance of nHDL-like particles as dimer complexes indicates that compositional asymmetry engineered by leaflet-specific mβCD lipid exchange of biotin-PE lipids in GUVs has been maintained in the formation of nanodisc structures by Δ49ApoA-I. To confirm these results, further experiments are required – and limitations to the technique must be defined. If successful,

the synthesis of tailor-made leaflet asymmetry incorporated into nanodisc particles would serve as a new tool for the reconstitution of compositionally dependent integral membrane proteins for structural analysis.

Acknowledgments

This work performed under the auspices of the U.S. Department of Energy by Lawrence Livermore National Laboratory under Contract DE-AC52-07NA27344 with support from Lawrence Livermore National Laboratory Laboratory-Directed Research and Development Program. The results shared in this chapter were possible thanks to the help of Dr. Daniel Speer for preparation and FRAP measurements of SLBs treated with CLC, Dr. Wei He for SEC purification of HDL-like particles, and Dr. Yaqing Wang for HS-AFM imaging and analysis of nanodiscs structures.

Chapter 5

Summary

5.1 Compositionally dependent tubule generation via asymmetric mβCD lipid exchange

Chapter 2 discussed the membrane remodeling effects of methyl-β-cyclodextrin (mβCD) in giant unilamellar vesicles (GUVs) composed of both single and multi-lipid membrane compositions. The hydrophobic space within this oligosaccharide is capable of housing and solubilizing both lipids and sterols – and exchanging these amphipathic molecules directly with the outer leaflet of organized lipid mesophases. We utilize mβCD's leaflet-specific ability to selectively remove lipids from the outer membrane to induce a differential stress-generating membrane remodeling.

We report that introducing small concentrations (0.5-5 mM) of mβCD to a collection of GUVs composed of 1-palmitoyl-2-oleoyl-sn-glycero-3-phosphocholine (POPC) results in the generation of inward facing membrane tubules (**Fig. 2.1**). These observations of membrane remodeling are consistent with the generation of spontaneous negative curvature induced by a removal of lipids

from the outermost leaflet of the vesicle, and induction of a differential stress across the membrane. The tubules generated by the interaction between mβCD and the vesicular membrane were analyzed, measuring a tubule persistence length of 3.5 ± 0.1 μm, with an estimated radius of ~30 nm.

Multicomponent GUVs are prepared from an equimolar ratio of POPC, egg-sphingomyelin (SM), and cholesterol (1:1:1). These vesicles are introduced to 0.5 mM of a cholesterol pre-loaded mβCD (CLC) (~6:1 = mβCD:Chol) – preloading cyclodextrin in this way is a common approach used to boost mβCD interaction with cholesterol-containing membranes (*56*, *57*). Initially homogeneous, the membrane of 1:1:1 GUVs begin to produce phase domains after incubation of CLC (**Fig. 2.2b**), followed by domain-specific tubule generation isolated within the liquid-disordered phase (POPC & cholesterol-poor).

We propose the following steps to describe phase separation and nanotubule generation seen in multi-component GUVs: (i) CLC is introduced to an initially homogeneous membrane. mβCD participates in the preferential removal of cholesterol (*98*, *99*) from the outer leaflet of the membrane. (ii) Cholesterol undergoes rapid transverse diffusion (10^3-10^4 s^{-1}) (*100*, *101*) acting to counteract the generation of leaflet density asymmetry across the membrane. (iii) The removal of primarily cholesterol from the membrane of the GUV leads to a shift of the membrane composition towards a two-domain state (*75*). (iv) Upon the appearance of phase separation, the L_o domain has transitioned into a gel-like ordering of lipids, suppressing the ability for cholesterol to readily flip-flop. (v) Without cholesterol counteracting differential stress, continued removal of lipid, sphingomyelin (*102*) or cholesterol results in the generation leaflet asymmetry. This asymmetry

generates spontaneous curvature within the fluid domain (L_d), resulting in tubule formation composed of primarily POPC (**Fig. 2.3a & 2.3b**).

5.2 Generation of membrane curvature and selective lipid removal concomitant with nHDL-like particle formation

In Chapter 4, we discussed the complex membrane deformative effects of apolipoproteins, which make up ~70% of the protein mass of high-density lipoprotein (HDL) – a class of lipoprotein responsible for reverse cholesterol transport and commonly referred to as, "good cholesterol". The dynamics of the highly alpha-helical, and amphipathic, secondary structure of apolipoproteins play an essential role to its function, including the recruitment of lipid and stability of the discoidal assembly (nHDL). We identify previously unrecognized biophysical steps – including poration, vesiculation, and phase separation – which mark the ApoA-I-membrane interactions *en route* to the formation of HDL-like particles.

We introduce a collection of single-component, POPC GUVs to 0.88 μM of an N-terminally truncated isoform of ApoA-I in which the first 49 amino acids are removed – Δ49ApoA-I. This modification has been previously shown to preserve the essential lipoprotein lipid interactions (*141*). Following incubation with Δ49ApoA-I, POPC GUVs are observed to form transient-microscopic pores (**Fig. 3.1a**), through which the encapsulated solute and solvent are allowed to mix with the exterior bath (**Fig. 3.1a**). Then, a critical point is reached and the GUV lyses forming

a collection of smaller and more stable daughter vesicles (**Fig. 3.1b**). The increase in the helical segment population then triggers enhanced "interfacial activity (*149*)," which reflects the increased ability of the protein to (i) bind to the membrane; (ii) partition into the membrane–water interface, acting as a wedge altering the packing and organization of the lipids within the membrane (*35*, *36*); and induce an area mismatch (*37*) between the two individual leaflets that make up the phospholipid bilayer. These mechanical deformations synergistically serve to reduce the energy cost for the creation of curvature generation (*38*) and thus promote vesiculation, such as we observe.

We ran a series of coarse-grained molecular dynamics (cg-MD) simulations that study the interaction of apolipoproteins and lipid bilayers (**Fig. 3.3**). These simulations show that Apolipoprotein interactions significantly depend on the lipid composition of the membrane in a way that the presence of negatively charged lipid species may help mediate embedding of the protein into the membrane surface. Furthermore, ApoA-I maintains long term association with membrane compositions used in experimental observations, a necessary interaction for both inducing leaflet area mismatch and the formation of nHDL-like particles. Size exclusion chromatography purification and high-speed atomic force microscopy imaging confirm the formation of discoidal particles **(Fig. 3.2a**).

The appearance of lipid selectivity from the MD simulations motivates an experimental assay of Δ49ApoA-I with GUVs formed from a lipid mixture of POPC, SM and Cholesterol in an equimolar ratio (1:1:1). These vesicles, which initially appear homogeneous, begin to form domains of phase separated lipids, consistent with the removal of cholesterol, shifting the composition of the

remaining lipid into the two-domain regions in the phase diagram (*163*). Additionally, these multi-component GUVs exhibit a stark difference in curvature when breakdown occurs (**Fig. 3.4**) – forming spherical structures of high-intensity NBD-PE (green) are observed to appear from the membrane, while portions of the membrane marked by Rho-PE (red) remain unstructured. This difference can be attributed to the differences in the bending moduli (*25*, *160*) of the two co-existing phases. For PC:SM:Chol membranes, the difference in bending rigidity between the liquid-ordered (red, κ_{L_o} = 6.4 ± 0.3 (*84*)) and the liquid-disordered (green, κ_{L_d} = 2.6 ± 0.4 (*84*)) membrane domains are reflected in the discrepancy between their structural appearance. The results are the complementary images we observe in **Figures 3.4c & 3.4d**.

5.3 Preliminary evidence of compositional asymmetry reconstituted into nHDL-like particles

Finally, in Chapter 4 we discuss the convergence of Chapters 2 & 3 - The application of mβCD in the synthesis of artificial, tailor-made membrane asymmetry in synthetic cells, followed by the reconstitution of HDL particles that maintain this engineered asymmetry. Nascent HDL particles have served as a platform to decipher three-dimension structure of integral proteins. While this advancement has substantially furthered our understanding of protein structures and functions, reconstituting tailored compositional asymmetry into nanodiscs has not yet been achieved – a necessary parameter for effective capture of asymmetry-dependent integral proteins.

In Chapter 2, we showed that mβCD can effectively remove POPC lipids from vesicular membranes. We began by introducing CLC to a supported bilayer to investigate whether cholesterol can additionally be deposited into the membrane. Fluorescence recovery after photobleaching measured the fluidity of the membrane before and after the addition of CLC, exhibiting a ~40% decrease in lipid after incubation – consistent with an increase in membrane cholesterol content.

Next, we assay whether more complex lipid species can also be exchanged. mβCD is preloaded with biotinylated lipids and incubated with POPC GUVs. After the reaction is halted by a bath exchange, a FITC-labeled streptavidin is introduced, selectively labeling the exterior of the GUV membrane (**Fig. 4.3**). This indicates that biotin-PE has been deposited into the outer leaflet of the vesicle, through asymmetric mβCD exchange. These findings set the stage for the selective manipulation of bilayer properties to understand such effects on membrane function, as well as tuning synthetic bilayers for desired physiochemical behavior.

Finally, we showed in Chapter 3 that nHDL-like particles are effectively formed from the membrane of GUVs. We introduced 8.325 μM of Δ49ApoA-I to biotin-PE:mβCD treated GUVs to reconstitute nHDL particles that maintain compositional asymmetry. We characterized this asymmetry through the addition of 2.16 μM of streptavidin, which will bind to the biotin-PE present in the nanodiscs. If the nanodisc-SA complex form dimers, then that indicates asymmetry has effectively been preserved during the formation of the nascent particles. Once purified through SEC and imaged with HS-AFM, we observe dimer-complexes of nHDL particles (**Fig. 4.5d**).

These preliminary findings indicate that compositional asymmetry, engineered via leaflet-specific mβCD lipid exchange in GUVs, can be successfully maintained during the formation of nanodisc structures by Δ49ApoA-I. However, further validation is necessary to confirm these results and to delineate the limitations of the technique. Future experiments should include quantitative analyses of lipid distribution, assessment of asymmetric stability over time, and exploration of additional lipid species and diverse protein targets.

If this approach proves robust, the ability to synthesize nanodiscs with defined leaflet asymmetry will represent a significant advance. Such tailor-made nanodiscs could become a powerful tool for reconstituting and structurally analyzing integral membrane proteins whose functions are modulated by lipid asymmetry—expanding the experimental toolkit for membrane biology, biophysics and structural biochemistry.

Supplementary

Supplementary Table 3.1: Molecular dynamics simulations

Membrane Composition	**WT APOA1**		**D49 APOA1**	
	Without restraints	*With restraints*	*Without restraints*	*With restraints*
POPC	10 µs	5 µs	10 µs	5 µs
POPC	5 µs	5 µs	5 µs	5 µs
POPC	5 µs	5 µs	5 µs	5 µs
POPC:POPS	10 µs	5 µs	10 µs	5 µs
POPC:POPS	5 µs	5 µs	5 µs	5 µs
POPC:POPS	5 µs	5 µs	5 µs	5 µs
CHOL:DPSM:POPC	10 µs	5 µs	10 µs	5 µs
CHOL:DPSM:POPC	5 µs	5 µs	5 µs	5 µs
CHOL:DPSM:POPC	5 µs	5 µs	5 µs	5 µs
PM8	10 µs	5 µs	10 µs	5 µs
PM8	5 µs	5 µs	5 µs	5 µs
PM8	5 µs	5 µs	5 µs	5 µs

Supplementary Table 1: List of 48 coarse-grained MD simulations carried out in this work

Supplementary Figure 3.1: Pore formation events

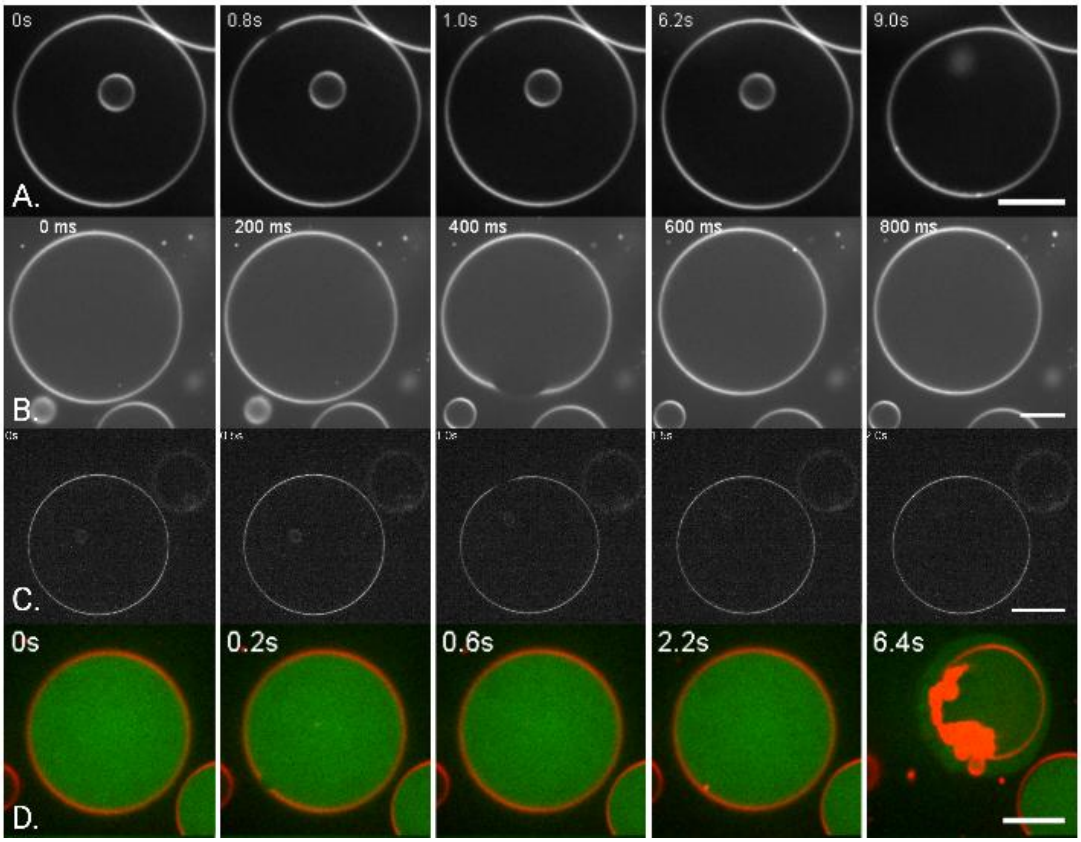

Supplementary Figure 7: Montage of transient pore events in GUV, along with the radius of the pore (R_p) and the lifetime of the pore (L_p). ***(a)*** *POPC GUV introduced to 0.88µM of Δ49ApoA-1. R_p = ~1µm and L_p = ~1.2s.* ***(b)*** *POPC GUV introduced to 0.88µM of Δ49ApoA-1. R_p = 6µm and L_p = ~0.2s.* ***(c)*** *1:1:1 RAFT GUV introduced to 0.44µM of Δ49ApoA-1. R_p = 3.7µm and L_p = ~0.5s.* ***(d)*** *POPC GUV introduced to 0.44µM of Δ49ApoA-1. R_p = 1.1µm and L_p = ~2s. Scale bars are 10 µm.*

Supplementary Figure 3.2: Solute leakage through a cascade of pore formation events

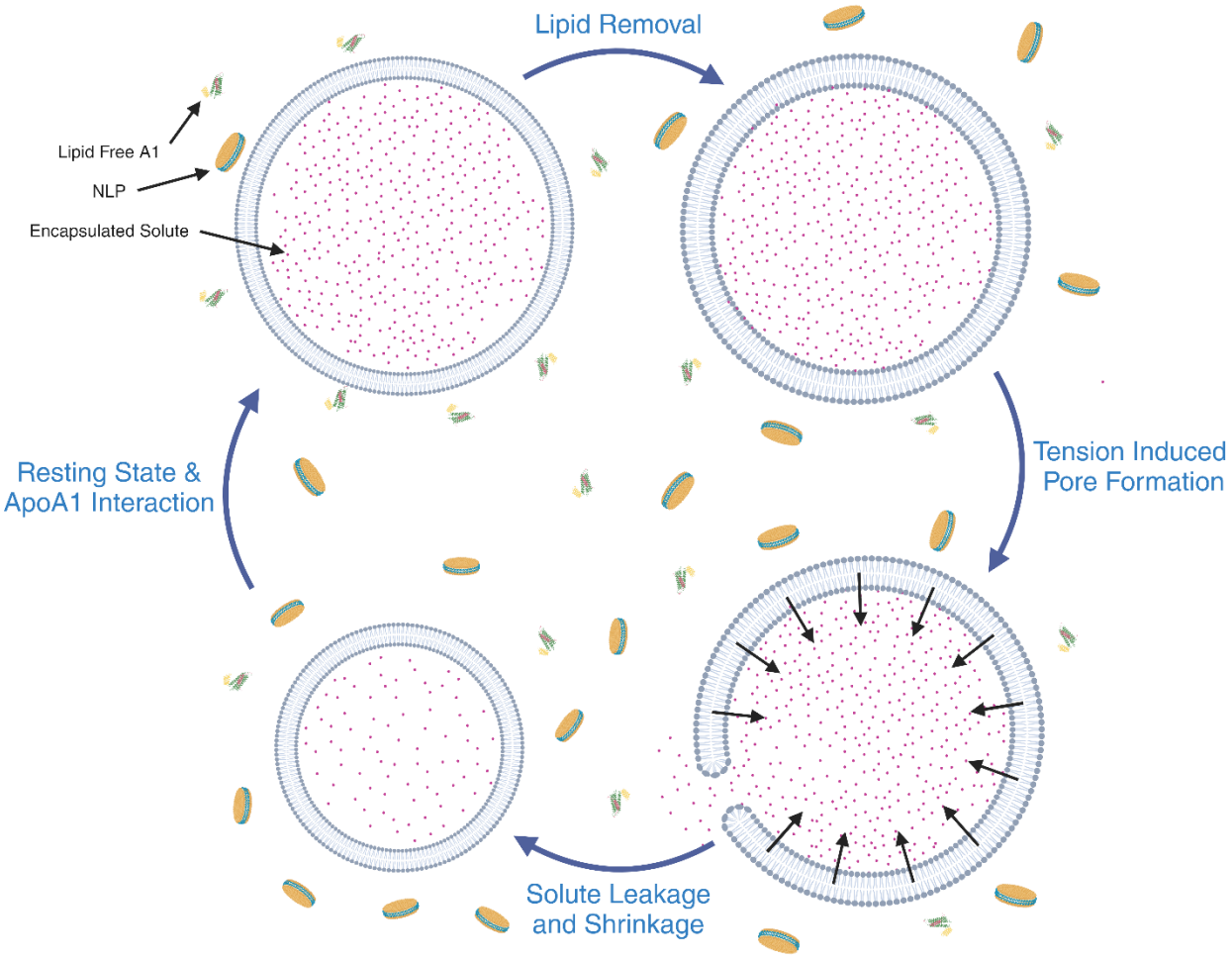

Supplementary Figure 2: Diagram of cyclic behavior of giant unilamellar vesicles (GUVs) in response to apolipoprotein interaction. Starting from the top left, (i) an initially isotonic GUV is introduced to lipid-free apolipoprotein, (ii) upon membrane interaction, NLP formation ensues through the stochastic removal of lipid from the membrane. (iii) The GUV now experiences a reduced lipid density (an initially isotonic condition acts to maintain encapsulated volume, as solute is membrane impermeable) and increasing membrane tension until a critical threshold is reached and a transient pore is formed. This pore allows for the exchange of solute and solvent, while excess Laplace pressure assists in the resealing of the pore around a smaller volume. (iv) The GUV is now at a new equilibrium, in which continued lipid removal may ensue, and repeat this cycle.

Supplementary Figure 3.3: DOPC:POPS (4:1) Vesiculation due to WT ApoE-4

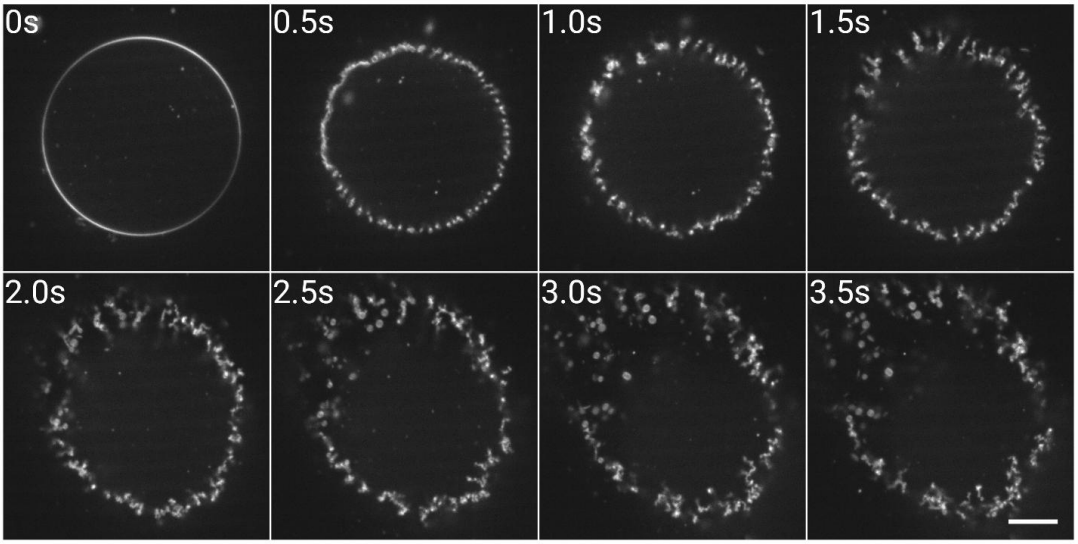

Supplementary Figure 3: Vesiculation montage of DOPC:POPS (4:1) GUV exposed to 3μL of 0.5mg/mL WT ApoE4. Scale bar = 10 μm.

Supplementary Figure 3.4: DOPC:DOPS (4:1) Vesiculation due to ApoE-3

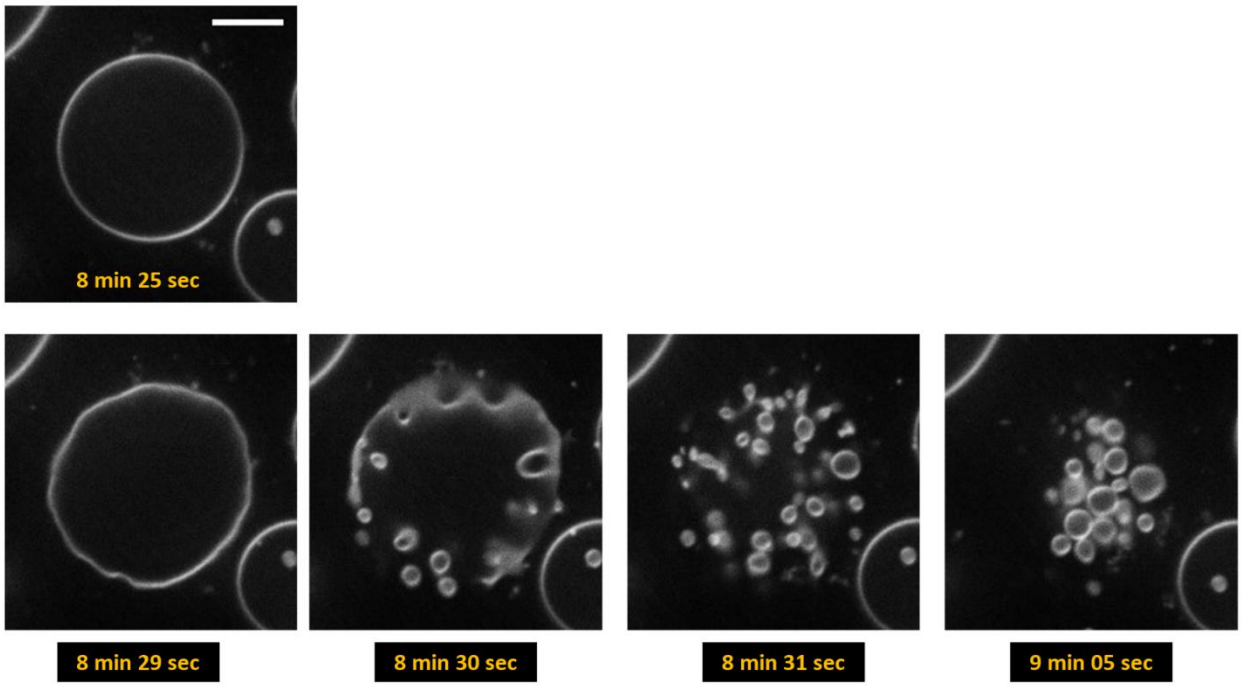

Supplementary Figure 4: Montage of DOPC:DOPS (4:1) GUVs incubated in 7.38 μM ApoE3. Scale Bar is 10um

Supplementary Figure 3.5: Coarse-Grained MD Snapshot of Δ49 & WT ApoA-I

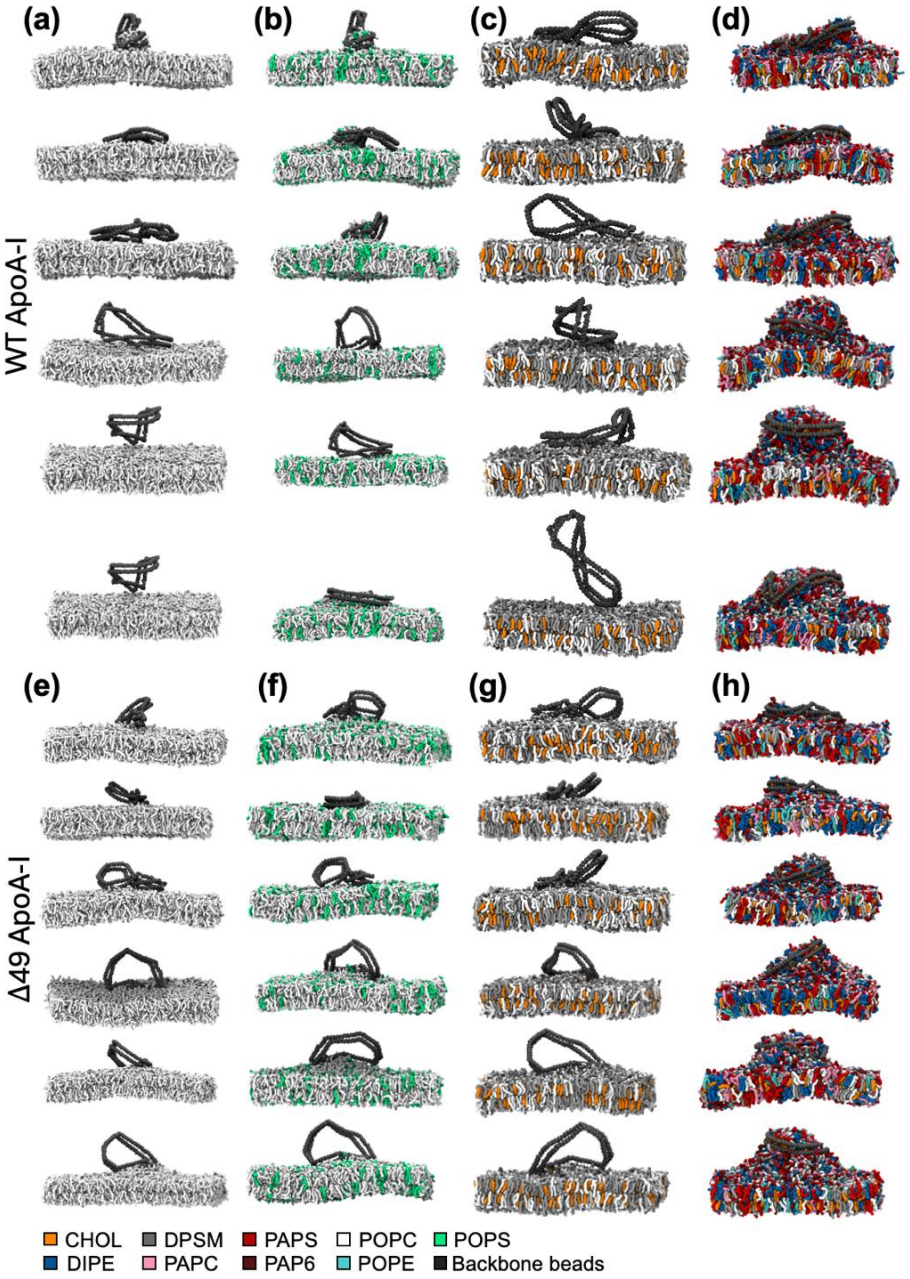

Figure 5: *Last snapshots of all coarse-grained molecular dynamics simulations carried out using a pre-assembled WT or Δ49 ApoA-I double belt protein with different membranes. Panels a-d show the WT ApoA-I double-belt and the* ***(a)*** *POPC,* ***(b)*** *4:1 POPC:POPS,* ***(c)*** *1:1:1 CHOL:DPSM:POPC and* ***(d)*** *PM8 (plasma membrane mimetic model) lipid bilayers at the end of six independent coarse-grained molecular dynamics simulation. Panels e-g represent the Δ49 ApoA-I protein and the* ***(e)*** *POPC,* ***(f)*** *4:1 POPC:POPS,* ***(g)*** *1:1:1 CHOL:DPSM:POPC and* ***(h)*** *PM8 membranes. In each panel, the top row shows the simulated system at the end of 10 μs whereas the rest of the rows show the same system at the end of 5 μs-long independent simulations. The top three rows in each system show simulations are carried out without any restraints in the protein while the last three rows show systems simulated with restraints in the protein as explained in the Methods. Lipids are color-coded: CHOL in orange, DIPE in blue, DPSM in gray, PAPC in pink, PAPS in red, PAP6 in dark red, POPC in white, POPE in cyan and POPS in green. Water and ions are not shown for clarity. Backbone beads of the protein are colored in dark gray.*

Supplementary Figure 3.6: Post-vesiculation of 2:2:1 (POPC:SM:Chol) GUVs

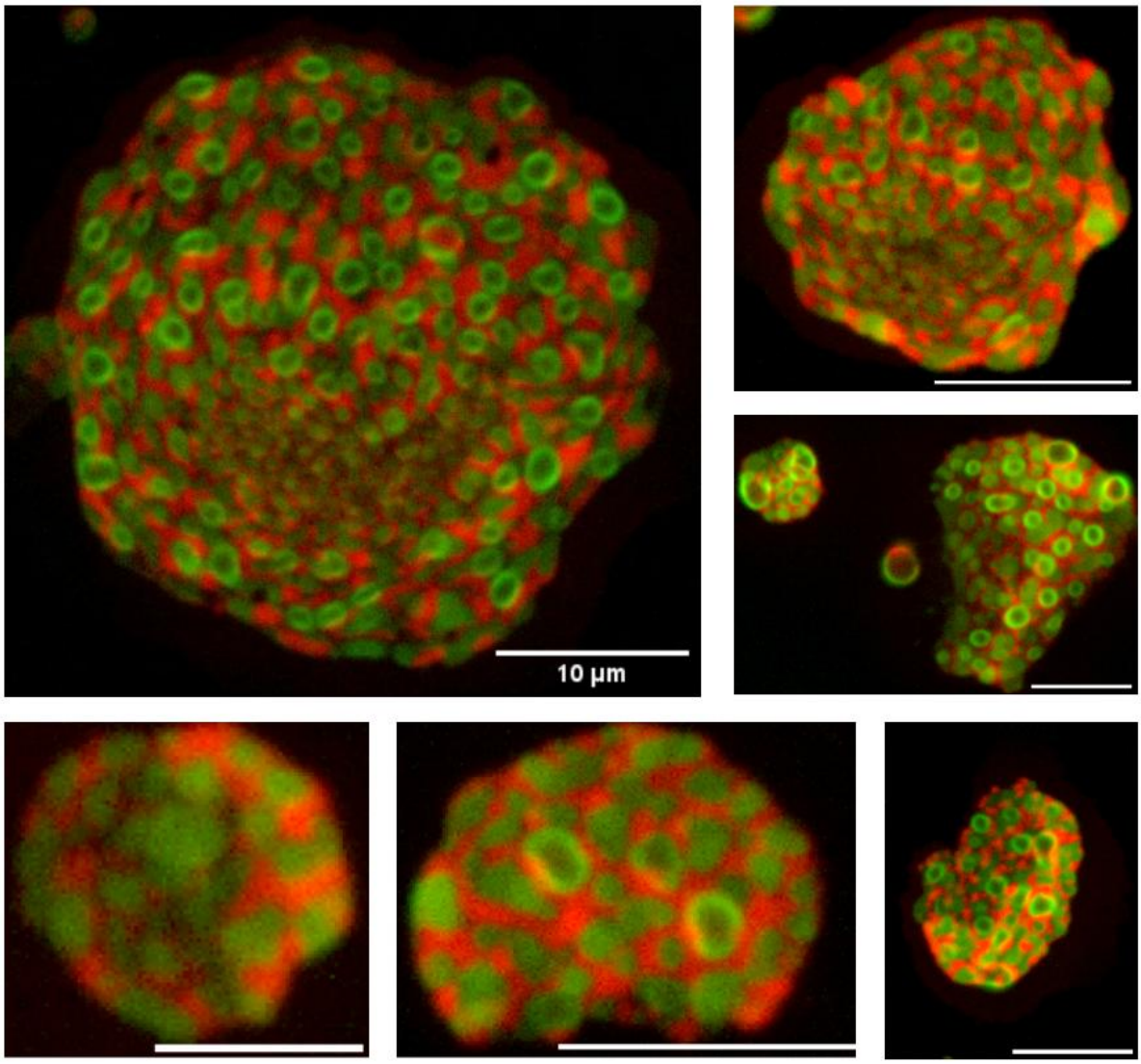

Supplementary Figure 6: Post Vesiculation of 2:2:1 (POPC:SM:Chol) GUVs following the introduction of ~1.7µM of Δ49ApoA-1. These GUVs are doped with 1 mol % of Rho-DOPE (red) and 3 mol % NBD-PE (green). Phase separated GUVs burst rapidly upon interaction with Δ49ApoA-1. Adhered to the glass substrate, a clear distinction between membrane domains is observed. The Chol-rich, SM domain (green) retains spherical structure.

Supplementary Video 3.1: POPC Leakage and Vesiculation

Supplementary Video 1: A collection of POPC GUVs doped with 1 mol % Rho-B-DOPE (red) and encapsulating 100µM of a soluble, membrane impermeable dye NBD-G (green). Upon introducing 0.88uM of Δ49ApoA-1, GUV leakage, transient pore formation and vesiculation are observed.

Supplementary Video 3.2: POPC Leakage and Vesiculation Extended

Supplementary Video 2: A collection of POPC GUVs doped with 1 mol % Rho-B-DOPE (red) and encapsulating 100µM of a soluble, membrane impermeable dye NBD-G (green). Upon introducing 0.88uM of Δ49ApoA-1, GUV leakage, transient pore formation and vesiculation are observed. These effects propagate throughout the sample over the observed time (17 min).

Supplementary Video 3.3: DOPC:DOPS (4:1) GUV Vesiculation

Supplementary Video 3: DOPC:POPS (4:1) GUVs doped with 1 mol % Rho-B-DOPE (red). Tubules within the GUV are a common artifact of the electroformation technique and are unrelated protein interaction. Upon introducing 3uL of 0.078mg/mL of WT ApoA-I, vesiculation of the GUV occurs.

Supplementary Video 3.4: 1:1:1 (POPC:SM:Chol) GUV Phase separation & Vesiculation Ex. 1

*Supplementary Video 4: Equimolar GUVs composed of POPC, egg-SM and cholesterol is doped with 1 mol % Rho-B-DOPE (L_d) (**red**) and 3 mol % NBD-PE (L_o) (**green**). Phase separation and vesiculation following the introduction of ~3.5 µM Δ49ApoA-I. At 8:40, brightness/contrast correction is applied so membrane deformation is clearly visible. A pore can be seen to appear beginning at 9:01. Scale Bar 20µm. Scale bar 10µm.*

Supplementary Video 3.5: 1:1:1 (POPC:SM:Chol) GUV Phase separation & Vesiculation Ex. 2

*Supplementary Video 5: Equimolar GUVs composed of POPC, egg-SM and cholesterol is doped with 1 mol % Rho-B-DOPE (L_d) (**red**) and 3 mol % NBD-PE (L_o) (**green**). Phase separation and vesiculation following the introduction of ~1.76 µM Δ49ApoA-I.*

Supplementary Video 3.6: 1:1:1 (POPC:SM:Chol) GUV Phase separation & Vesiculation Ex. 3

*Supplementary Video 6: Equimolar GUVs composed of POPC, egg-SM and cholesterol is doped with 1 mol % Rho-B-DOPE (L_d) (**red**) and 3 mol % NBD-PE (L_o) (**green**). Phase separation and vesiculation following the introduction of ~1.76 µM Δ49ApoA-I. Scale bar is 10µm.*

Bibliography

1. S. Lahiri, A. Toulmay, W. A. Prinz, Membrane contact sites, gateways for lipid homeostasis. *Current opinion in cell biology* **33**, 82-87 (2015).
2. T. Levine, C. Loewen, Inter-organelle membrane contact sites: through a glass, darkly. *Current opinion in cell biology* **18**, 371-378 (2006).
3. A. Toulmay, W. A. Prinz, Lipid transfer and signaling at organelle contact sites: the tip of the iceberg. *Current opinion in cell biology* **23**, 458-463 (2011).
4. M. R. Wieckowski, C. Giorgi, M. Lebiedzinska, J. Duszynski, P. Pinton, Isolation of mitochondria-associated membranes and mitochondria from animal tissues and cells. *Nat Protoc* **4**, 1582-1590 (2009).
5. D. A. Los, N. Murata, Membrane fluidity and its roles in the perception of environmental signals. *Biochimica et Biophysica Acta (BBA)-Biomembranes* **1666**, 142-157 (2004).
6. H. M. McConnell, Structures and transitions in lipid monolayers at the air-water interface. *Annual Review of Physical Chemistry* **42**, 171-195 (1991).
7. R. Lipowsky, The conformation of membranes. *Nature* **349**, 475-481 (1991).
8. A. Roux, K. Uyhazi, A. Frost, P. De Camilli, GTP-dependent twisting of dynamin implicates constriction and tension in membrane fission. *Nature* **441**, 528-531 (2006).
9. D. S. Goodsell, Escherichia Coli Bacterium. *RCSB Protein Data Bank*, (2021).
10. C. Xu, N. Martin, M. Li, S. Mann, Living material assembly of bacteriogenic protocells. *Nature* **609**, 1029-1037 (2022).

11. T. E. Miller *et al.*, Light-powered CO2 fixation in a chloroplast mimic with natural and synthetic parts. *Science* **368**, 649-654 (2020).

12. J. E. H. Bücher *et al.*, Bottom-up assembly of target-specific cytotoxic synthetic cells. *Biomaterials* **285**, 121522 (2022).

13. N. F. Morales-Penningston *et al.*, GUV preparation and imaging: minimizing artifacts. *Biochim Biophys Acta* **1798**, 1324-1332 (2010).

14. M. I. Angelova, D. S. Dimitrov, Liposome electroformation. *Faraday discussions of the Chemical Society* **81**, 303-311 (1986).

15. M. Angelova, D. S. Dimitrov, A mechanism of liposome electroformation. *Trends in colloid and interface science II*, 59-67 (1988).

16. E. M. Schmid, D. L. Richmond, D. A. Fletcher, in *Methods in cell biology*. (Elsevier, 2015), vol. 128, pp. 319-338.

17. Q. Li, X. Wang, S. Ma, Y. Zhang, X. Han, Electroformation of giant unilamellar vesicles in saline solution. *Colloids and Surfaces B: Biointerfaces* **147**, 368-375 (2016).

18. S. Deshpande, Y. Caspi, A. E. Meijering, C. Dekker, Octanol-assisted liposome assembly on chip. *Nat Commun* **7**, 10447 (2016).

19. C. Chen *et al.*, Regulating biocondensates within synthetic cells via segregative phase separation. *ACS Nano*, (2025).

20. Y. Huang *et al.*, A New Means to Generate Liposomes by Rehydrating Engineered Lipid Nanoconstructs. *Micromachines* **16**, 138 (2025).

21. K. Farsad, P. De Camilli, Mechanisms of membrane deformation. *Current opinion in cell biology* **15**, 372-381 (2003).

22. A. M. Robertson, V. J. Allan, Brefeldin a-dependent membrane tubule formation reconstituted in vitro is driven by a cell cycle–regulated microtubule motor. *Molecular Biology of the Cell* **11**, 941-955 (2000).

23. N. Sperelakis, *Cell physiology source book: essentials of membrane biophysics*. (Elsevier, 2012).

24. F. Sachs, Stretch-activated ion channels: what are they? *Physiology* **25**, 50-56 (2010).

25. P. D. Sambre, J. C. S. Ho, A. N. Parikh, Intravesicular Solute Delivery and Surface Area Regulation in Giant Unilamellar Vesicles Driven by Cycles of Osmotic Stresses. *J. Am. Chem. Soc.* **146**, 3250-3261 (2024).

26. K. Oglęcka, P. Rangamani, B. Liedberg, R. S. Kraut, A. N. Parikh, Oscillatory phase separation in giant lipid vesicles induced by transmembrane osmotic differentials. *eLife* **3**, e03695 (2014).

27. S. Al-Mosleh, A. Gopinathan, C. D. Santangelo, K. C. Huang, E. R. Rojas, Feedback linking cell envelope stiffness, curvature, and synthesis enables robust rod-shaped bacterial growth. *Proc. Natl. Acad. Sci. U.S.A.* **119**, e2200728119 (2022).

28. A. Mahapatra, C. Uysalel, P. Rangamani, The Mechanics and Thermodynamics of Tubule Formation in Biological Membranes. *J Membrane Biol* **254**, 273-291 (2021).

29. B. J. Peter *et al.*, BAR Domains as Sensors of Membrane Curvature: The Amphiphysin BAR Structure. *Science* **303**, 495-499 (2004).

30. M. C. S. Lee *et al.*, Sar1p N-Terminal Helix Initiates Membrane Curvature and Completes the Fission of a COPII Vesicle. *Cell* **122**, 605-617 (2005).

31. G. Drin, B. Antonny, Amphipathic helices and membrane curvature. *FEBS Letters* **584**, 1840-1847 (2010).

32. H. T. McMahon, E. Boucrot, Molecular mechanism and physiological functions of clathrin-mediated endocytosis. *Nat Rev Mol Cell Biol* **12**, 517-533 (2011).

33. K. Farsad *et al.*, Generation of high curvature membranes mediated by direct endophilin bilayer interactions. *The Journal of cell biology* **155**, 193-200 (2001).

34. K. Takei, V. I. Slepnev, V. Haucke, P. De Camilli, Functional partnership between amphiphysin and dynamin in clathrin-mediated endocytosis. *Nature cell biology* **1**, 33-39 (1999).

35. K. Hristova, C. E. Dempsey, S. H. White, Structure, Location, and Lipid Perturbations of Melittin at the Membrane Interface. *Biophysical Journal* **80**, 801-811 (2001).

36. J.-H. Lee *et al.*, Thermal Fluctuation and Elasticity of Lipid Vesicles Interacting with Pore-Forming Peptides. *Phys. Rev. Lett.* **105**, 038101 (2010).

37. M. P. Sheetz, S. J. Singer, Biological Membranes as Bilayer Couples. A Molecular Mechanism of Drug-Erythrocyte Interactions. *Proc. Natl. Acad. Sci. U.S.A.* **71**, 4457-4461 (1974).

38. H. Bouvrais *et al.*, Softening of POPC membranes by magainin. *Biophysical Chemistry* **137**, 7-12 (2008).

39. E. A. Evans, Bending resistance and chemically induced moments in membrane bilayers. *Biophysical Journal* **14**, 923-931 (1974).

40. E. Farge, P. F. Devaux, Shape changes of giant liposomes induced by an asymmetric transmembrane distribution of phospholipids. *Biophysical Journal* **61**, 347-357 (1992).

41. A. Hossein, M. Deserno, Spontaneous curvature, differential stress, and bending modulus of asymmetric lipid membranes. *Biophysical Journal* **118**, 624-642 (2020).

42. A. Hossein, M. Deserno, Stiffening transition in asymmetric lipid bilayers: the role of highly-ordered domains and the effect of temperature and size. *Biophysical Journal* **120**, 146a-147a (2021).

43. S. Shukla, T. Baumgart, Enzymatic trans-bilayer lipid transport: Mechanisms, efficiencies, slippage, and membrane curvature. *Biochimica et Biophysica Acta (BBA)-Biomembranes* **1863**, 183534 (2021).

44. M. A. Idiart, Y. Levin, Rupture of a liposomal vesicle. *Physical Review E* **69**, 061922 (2004).

45. A. S. Reddy, D. T. Warshaviak, M. Chachisvilis, Effect of membrane tension on the physical properties of DOPC lipid bilayer membrane. *Biochimica et Biophysica Acta (BBA) - Biomembranes* **1818**, 2271-2281 (2012).

46. S. U. Alam Shibly, C. Ghatak, M. A. Sayem Karal, M. Moniruzzaman, M. Yamazaki, Experimental Estimation of Membrane Tension Induced by Osmotic Pressure. *Biophys J* **111**, 2190-2201 (2016).

47. J. Li, X. J. Loh, Cyclodextrin-based supramolecular architectures: syntheses, structures, and applications for drug and gene delivery. *Advanced drug delivery reviews* **60**, 1000-1017 (2008).

48. J. Wankar *et al.*, Recent advances in host–guest self-assembled cyclodextrin carriers: Implications for responsive drug delivery and biomedical engineering. *Advanced Functional Materials* **30**, 1909049 (2020).

49. Z. Liu, L. Ye, J. Xi, J. Wang, Z.-g. Feng, Cyclodextrin polymers: Structure, synthesis, and use as drug carriers. *Progress in Polymer Science* **118**, 101408 (2021).

50. H. Dodziuk, *Cyclodextrins and their complexes: chemistry, analytical methods, applications*. (John Wiley & Sons, 2006).

51. K. Nishida, A. Tamura, N. Yui, pH-Responsive Coacervate Droplets Formed from Acid-Labile Methylated Polyrotaxanes as an Injectable Protein Carrier. *Biomacromolecules* **19**, 2238-2247 (2018).

52. Y. Yamada *et al.*, Enhanced autophagy induction via the mitochondrial delivery of methylated β-cyclodextrin-threaded polyrotaxanes using a MITO-Porter. *Chemical Communications* **55**, 7203-7206 (2019).

53. K. Tanhuanpää, P. Somerharju, γ-Cyclodextrins greatly enhance translocation of hydrophobic fluorescent phospholipids from vesicles to cells in culture: importance of molecular hydrophobicity in phospholipid trafficking studies. *Journal of Biological Chemistry* **274**, 35359-35366 (1999).

54. V. Kainu, M. Hermansson, P. Somerharju, Introduction of phospholipids to cultured cells with cyclodextrin. *Journal of Lipid Research* **51**, 3533-3541 (2010).

55. H.-T. Cheng, E. London, Preparation and Properties of Asymmetric Large Unilamellar Vesicles: Interleaflet Coupling in Asymmetric Vesicles Is Dependent on Temperature but Not Curvature. *Biophysical Journal* **100**, 2671-2678 (2011).

56. M. Doktorova *et al.*, Preparation of asymmetric phospholipid vesicles for use as cell membrane models. *Nat Protoc* **13**, 2086-2101 (2018).

57. H.-T. Cheng, E. London, Preparation and properties of asymmetric vesicles that mimic cell membranes. *Journal of Biological Chemistry* **284**, 6079-6092 (2009).

58. G. Li *et al.*, Efficient replacement of plasma membrane outer leaflet phospholipids and sphingolipids in cells with exogenous lipids. *Proc. Natl. Acad. Sci. U.S.A.* **113**, 14025-14030 (2016).

59. Q. Lin, E. London, Preparation of artificial plasma membrane mimicking vesicles with lipid asymmetry. *PLoS One* **9**, e87903 (2014).

60. H. Archontaki, M. Vertzoni, M. Athanassiou-Malaki, Study on the inclusion complexes of bromazepam with β-and β-hydroxypropyl-cyclodextrins. *Journal of pharmaceutical and biomedical analysis* **28**, 761-769 (2002).

61. H. Arima, T. Miyaji, T. Irie, F. Hirayama, K. Uekama, Enhancing effect of hydroxypropyl-β-cyclodextrin on cutaneous penetration and activation of ethyl 4-biphenylyl acetate in hairless mouse skin. *European journal of pharmaceutical sciences* **6**, 53-59 (1998).

62. H. Arima *et al.*, Comparative studies of the enhancing effects of cyclodextrins on the solubility and oral bioavailability of tacrolimus in rats. *Journal of pharmaceutical sciences* **90**, 690-701 (2001).

63. S. Baboota, S. Agarwal, Meloxicam complexation with β-cyclodextrin: Influence on the anti-inflammatory and ulcerogenic activity. *Die Pharmazie-An International Journal of Pharmaceutical Sciences* **58**, 73-74 (2003).

64. L. Ferreira, J. Campos, F. Veiga, C. Cardoso, A. C. Paiva-Santos, Cyclodextrin-based delivery systems in parenteral formulations: A critical update review. *European Journal of Pharmaceutics and Biopharmaceutics* **178**, 35-52 (2022).

65. A. T. N. Doan, N. Kojima, K. Sakurai, Reduced nephrotoxicity of epichlorohydrin-crosslinked β-cyclodextrin nanoparticles (βCDNPs) and its enhanced binding with

hydrophobic compounds. *Journal of Bioactive and Compatible Polymers* **39**, 522-535 (2024).

66. H. T. McMahon, J. L. Gallop, Membrane curvature and mechanisms of dynamic cell membrane remodelling. *Nature* **438**, 590-596 (2005).

67. J. Zimmerberg, M. M. Kozlov, How proteins produce cellular membrane curvature. *Nat Rev Mol Cell Biol* **7**, 9-19 (2006).

68. R. Phillips, T. Ursell, P. Wiggins, P. Sens, Emerging roles for lipids in shaping membrane-protein function. *Nature* **459**, 379-385 (2009).

69. B. Antonny, Mechanisms of membrane curvature sensing. *Annual review of biochemistry* **80**, 101-123 (2011).

70. Y. Yang *et al.*, Sorting sub-150-nm liposomes of distinct sizes by DNA-brick-assisted centrifugation. *Nat. Chem.* **13**, 335-342 (2021).

71. S. Taniguchi, M. Toyoshima, T. Takamatsu, J. Mima, Curvature-sensitive trans-assembly of human Atg8-family proteins in autophagy-related membrane tethering. *Protein Science* **29**, 1387-1400 (2020).

72. D. J. James, C. Khodthong, J. A. Kowalchyk, T. F. Martin, Phosphatidylinositol 4, 5-bisphosphate regulates SNARE-dependent membrane fusion. *The Journal of cell biology* **182**, 355-366 (2008).

73. H. Alimohamadi, P. Rangamani, Modeling membrane curvature generation due to membrane–protein interactions. *Biomolecules* **8**, 120 (2018).

74. F. Yuan *et al.*, Membrane bending by protein phase separation. *Proc. Natl. Acad. Sci. U.S.A.* **118**, e2017435118 (2021).

75. S. L. Veatch, S. L. Keller, Miscibility Phase Diagrams of Giant Vesicles Containing Sphingomyelin. *Phys. Rev. Lett.* **94**, 148101 (2005).

76. T. Baumgart, G. Hunt, E. R. Farkas, W. W. Webb, G. W. Feigenson, Fluorescence probe partitioning between L-o/L-d phases in lipid membranes. *Biochimica Et Biophysica Acta-Biomembranes* **1768**, 2182-2194 (2007).

77. F. A. Heberle, J. Wu, S. L. Goh, R. S. Petruzielo, G. W. Feigenson, Comparison of Three Ternary Lipid Bilayer Mixtures: FRET and ESR Reveal Nanodomains. *Biophysical Journal* **99**, 3309-3318 (2010).

78. J. Schindelin *et al.*, Fiji: an open-source platform for biological-image analysis. *Nature methods* **9**, 676-682 (2012).

79. P. A. Sokolov, M. V. Belousov, S. A. Bondarev, G. A. Zhouravleva, N. A. Kasyanenko, FibrilJ: ImageJ plugin for fibrils' diameter and persistence length determination. *Computer Physics Communications* **214**, 199-206 (2017).

80. D. M. E. SF. (Clarendon Press, Oxford, 1986).

81. J. F. Nagle, S. Tristram-Nagle, Structure of lipid bilayers. *Biochimica et Biophysica Acta (BBA)-Reviews on Biomembranes* **1469**, 159-195 (2000).

82. I. Derényi, F. Jülicher, J. Prost, Formation and interaction of membrane tubes. *Phys. Rev. Lett.* **88**, 238101 (2002).

83. M. A. S. Karal *et al.*, Effects of cholesterol on the size distribution and bending modulus of lipid vesicles. *Plos one* **17**, e0263119 (2022).

84. R. D. Usery *et al.*, Membrane bending moduli of coexisting liquid phases containing transmembrane peptide. *Biophysical Journal* **114**, 2152-2164 (2018).

85. T. Baumgart, S. T. Hess, W. W. Webb, Imaging coexisting fluid domains in biomembrane models coupling curvature and line tension. *Nature* **425**, 821-824 (2003).

86. R. Zidovetzki, I. Levitan, Use of cyclodextrins to manipulate plasma membrane cholesterol content: evidence, misconceptions and control strategies. *Biochimica et Biophysica Acta (BBA)-Biomembranes* **1768**, 1311-1324 (2007).

87. E. Ottico *et al.*, Dynamics of membrane lipid domains in neuronal cells differentiated in culture1. *Journal of Lipid Research* **44**, 2142-2151 (2003).

88. V. A. Fadok *et al.*, A receptor for phosphatidylserine-specific clearance of apoptotic cells. *Nature* **405**, 85-90 (2000).

89. R. Lipowsky *et al.*, Leaflet tensions control the spatio-temporal remodeling of lipid bilayers and nanovesicles. *Biomolecules* **13**, 926 (2023).

90. P. K. Mattila, P. Lappalainen, Filopodia: molecular architecture and cellular functions. *Nat Rev Mol Cell Biol* **9**, 446-454 (2008).

91. J. Derganc, A. Čopič, Membrane bending by protein crowding is affected by protein lateral confinement. *Biochimica et Biophysica Acta (BBA)-Biomembranes* **1858**, 1152-1159 (2016).

92. S. Leibler, Curvature instability in membranes. *Journal de Physique* **47**, 507-516 (1986).

93. P. Sens, M. S. Turner, Budded membrane microdomains as tension regulators. *Physical Review E* **73**, 031918 (2006).

94. L. Miao, U. Seifert, M. Wortis, H.-G. Döbereiner, Budding transitions of fluid-bilayer vesicles: The effect of area-difference elasticity. *Physical Review E* **49**, 5389 (1994).

95. P. B. Canham, The minimum energy of bending as a possible explanation of the biconcave shape of the human red blood cell. *Journal of theoretical biology* **26**, 61-81 (1970).

96. W. Helfrich, Elastic properties of lipid bilayers: theory and possible experiments. *Zeitschrift für Naturforschung c* **28**, 693-703 (1973).

97. E. Falck, M. Patra, M. Karttunen, M. T. Hyvönen, I. Vattulainen, Lessons of slicing membranes: interplay of packing, free area, and lateral diffusion in phospholipid/cholesterol bilayers. *Biophysical Journal* **87**, 1076-1091 (2004).

98. S.-L. Niu, B. J. Litman, Determination of membrane cholesterol partition coefficient using a lipid vesicle–cyclodextrin binary system: effect of phospholipid acyl chain unsaturation and headgroup composition. *Biophysical Journal* **83**, 3408-3415 (2002).

99. R. Leventis, J. R. Silvius, Use of cyclodextrins to monitor transbilayer movement and differential lipid affinities of cholesterol. *Biophysical Journal* **81**, 2257-2267 (2001).

100. S. Baral, I. Levental, E. Lyman, Composition dependence of cholesterol flip-flop rates in physiological mixtures. *Chemistry and physics of lipids* **232**, 104967 (2020).

101. R.-X. Gu, S. Baoukina, D. P. Tieleman, Cholesterol flip-flop in heterogeneous membranes. *Journal of chemical theory and computation* **15**, 2064-2070 (2019).

102. A. Tsamaloukas, H. Szadkowska, P. J. Slotte, H. Heerklotz, Interactions of cholesterol with lipid membranes and cyclodextrin characterized by calorimetry. *Biophysical Journal* **89**, 1109-1119 (2005).

103. M. I. Angelova, D. S. Dimitrov, Liposome Electroformation.

104. R. A. Davis, Evolution of processes and regulators of lipoprotein synthesis: From birds to mammals. *Journal of Nutrition* **127**, S795-S800 (1997).

105. R. W. Mahley, T. L. Innerarity, S. C. Rall, K. H. Weisgraber, PLASMA-LIPOPROTEINS - APOLIPOPROTEIN STRUCTURE AND FUNCTION. *Journal of Lipid Research* **25**, 1277-1294 (1984).

106. R. Huang *et al.*, Apolipoprotein A-I structural organization in high-density lipoproteins isolated from human plasma. *Nature Structural & Molecular Biology* **18**, 416-U444 (2011).

107. R. J. Havel, H. A. Eder, J. H. Bragdon, DISTRIBUTION AND CHEMICAL COMPOSITION OF ULTRACENTRIFUGALLY SEPARATED LIPOPROTEINS IN HUMAN SERUM. *J. Clin. Invest.* **34**, 1345-1353 (1955).

108. C. J. Packard, J. Shepherd, Lipoprotein heterogeneity and apolipoprotein B metabolism. *Arteriosclerosis Thrombosis and Vascular Biology* **17**, 3542-3556 (1997).

109. R. I. Levy, D. S. Fredrickson, HETEROGENEITY OF PLASMA HIGH DENSITY LIPOPROTEINS. *J. Clin. Invest.* **44**, 426-+ (1965).

110. A. Kontush *et al.*, in *High Density Lipoproteins: From Biological Understanding to Clinical Exploitation*, A. VonEckardstein, D. Kardassis, Eds. (2015), vol. 224, pp. 3-51.

111. G. H. Rothblat, M. C. Phillips, High-density lipoprotein heterogeneity and function in reverse cholesterol transport:. *Current Opinion in Lipidology* **21**, 229-238 (2010).

112. C. J. Fielding, P. E. Fielding, MOLECULAR PHYSIOLOGY OF REVERSE CHOLESTEROL TRANSPORT. *Journal of Lipid Research* **36**, 211-228 (1995).

113. A. R. Tall, Cholesterol efflux pathways and other potential mechanisms involved in the athero-protective effect of high density lipoproteins. *Journal of Internal Medicine* **263**, 256-273 (2008).

114. A. V. Khera *et al.*, Cholesterol Efflux Capacity, High-Density Lipoprotein Function, and Atherosclerosis. *N Engl J Med* **364**, 127-135 (2011).

115. S. K. Karathanasis, V. I. Zannis, J. L. Breslow, ISOLATION AND CHARACTERIZATION OF THE HUMAN APOLIPOPROTEIN-A-I GENE. *Proceedings of the National Academy of Sciences of the United States of America-Biological Sciences* **80**, 6147-6151 (1983).

116. V. I. Zannis, F. S. Cole, C. L. Jackson, D. M. Kurnit, S. K. Karathanasis, DISTRIBUTION OF APOLIPOPROTEIN-A-I, APOLIPOPROTEIN-C-II, APOLIPOPROTEIN-C-III, AND APOLIPOPROTEIN-E MESSENGER-RNA IN FETAL HUMAN-TISSUES - TIME-DEPENDENT INDUCTION OF APOLIPOPROTEIN-E MESSENGER-RNA BY CULTURES OF HUMAN MONOCYTE-MACROPHAGES. *Biochemistry* **24**, 4450-4455 (1985).

117. F. Quazi, R. S. Molday, Differential Phospholipid Substrates and Directional Transport by ATP-binding Cassette Proteins ABCA1, ABCA7, and ABCA4 and Disease-causing Mutants. *Journal of Biological Chemistry* **288**, 34414-34426 (2013).

118. J. P. Segrest, W. S. Davidson, J. W. Heinecke, Phospholipid transport by ABCA1: the extracellular translocase or alternating access model? *Current Opinion in Lipidology* **34**, 208-213 (2023).

119. R. S. Rosenson *et al.*, Cholesterol Efflux and Atheroprotection Advancing the Concept of Reverse Cholesterol Transport. *Circulation* **125**, 1905-1919 (2012).

120. D. A. Bricarello, J. T. Smilowitz, A. M. Zivkovic, J. B. German, A. N. Parikh, Reconstituted Lipoprotein: A Versatile Class of Biologically-Inspired Nanostructures. *ACS Nano* **5**, 42-57 (2011).

121. T. H. Bayburt, Y. V. Grinkova, S. G. Sligar, Self-assembly of discoidal phospholipid bilayer nanoparticles with membrane scaffold proteins. *Nano Letters* **2**, 853-856 (2002).

122. I. G. Denisov, Y. V. Grinkova, A. A. Lazarides, S. G. Sligar, Directed self-assembly of monodisperse phospholipid bilayer nanodiscs with controlled size. *J. Am. Chem. Soc.* **126**, 3477-3487 (2004).

123. R. O. Ryan, Nanobiotechnology applications of reconstituted high density lipoprotein. *Journal of Nanobiotechnology* **8**, 1-10 (2010).

124. D. A. Bricarello, E. J. Mills, J. Petrlova, J. C. Voss, A. N. Parikh, Ganglioside embedded in reconstituted lipoprotein binds cholera toxin with elevated affinity. *Journal of Lipid Research* **51**, 2731-2738 (2010).

125. D. A. Bricarello, M. A. Patel, A. N. Parikh, Inhibiting host-pathogen interactions using membrane-based nanostructures. *Trends in Biotechnology* **30**, 323-330 (2012).

126. L. Rao, R. Tian, X. Y. Chen, Cell-Membrane-Mimicking Nanodecoys against Infectious Diseases. *ACS Nano* **14**, 2569-2574 (2020).

127. I. G. Denisov, S. G. Sligar, Nanodiscs for structural and functional studies of membrane proteins. *Nature Structural & Molecular Biology* **23**, 481-486 (2016).

128. I. G. Denisov, S. G. Sligari, Nanodiscs in Membrane Biochemistry and Biophysics. *Chem. Rev.* **117**, 4669-4713 (2017).

129. K. O. Baskakova, P. K. Kuzmichev, M. S. Karbyshev, Advanced applications of Nanodiscs-based platforms for antibodies discovery. *Biophysical Chemistry* **313**, (2024).

130. E. K. Makowski, J. S. Schardt, P. M. Tessier, Improving antibody drug development using bionanotechnology. *Current Opinion in Biotechnology* **74**, (2022).

131. J. H. Wald, E. Goormaghtigh, J. Demeutter, J. M. Ruysschaert, A. Jonas, INVESTIGATION OF THE LIPID DOMAINS AND APOLIPOPROTEIN ORIENTATION IN RECONSTITUTED HIGH-DENSITY-LIPOPROTEINS BY FLUORESCENCE AND IR METHODS. *Journal of Biological Chemistry* **265**, 20044-20050 (1990).

132. A. Jonas, K. E. Kezdy, J. H. Wald, DEFINED APOLIPOPROTEIN A-I CONFORMATIONS IN RECONSTITUTED HIGH-DENSITY LIPOPROTEIN DISKS. *Journal of Biological Chemistry* **264**, 4818-4824 (1989).

133. J. P. Segrest *et al.*, A Detailed Molecular Belt Model for Apolipoprotein A-I in Discoidal High Density Lipoprotein. *Journal of Biological Chemistry* **274**, 31755-31758 (1999).

134. P. S. Chetty *et al.*, Helical structure and stability in human apolipoprotein A-I by hydrogen exchange and mass spectrometry. *Proc. Natl. Acad. Sci. U.S.A.* **106**, 19005-19010 (2009).

135. H. Saito, S. Lund-Katz, M. C. Phillips, Contributions of domain structure and lipid interaction to the functionality of exchangeable human apolipoproteins. *Progress in Lipid Research* **43**, 350-380 (2004).

136. H. Saito *et al.*, α-Helix Formation Is Required for High Affinity Binding of Human Apolipoprotein A-I to Lipids. *Journal of Biological Chemistry* **279**, 20974-20981 (2004).

137. C. G. Brouillette *et al.*, Forster resonance energy transfer measurements are consistent with a helical bundle model for lipid-free apolipoprotein A-I. *Biochemistry* **44**, 16413-16425 (2005).

138. L. Chièze *et al.*, Difference in lipid packing sensitivity of exchangeable apolipoproteins apoA-I and apoA-II: An important determinant for their distinctive role in lipid metabolism. *Biochimica Et Biophysica Acta-Biomembranes* **1818**, 2732-2741 (2012).

139. C. P. L. Wan *et al.*, Apolipoprotein-induced conversion of phosphatidylcholine bilayer vesicles into nanodisks. *Biochimica Et Biophysica Acta-Biomembranes* **1808**, 606-613 (2011).

140. J. Varkey *et al.*, Membrane Curvature Induction and Tubulation Are Common Features of Synucleins and Apolipoproteins. *Journal of Biological Chemistry* **285**, 32486-32493 (2010).

141. J. A. Cappuccio *et al.*, Cell-free Co-expression of Functional Membrane Proteins and Apolipoprotein, Forming Soluble Nanolipoprotein Particles. *Molecular & Cellular Proteomics* **7**, 2246-2253 (2008).

142. L. Kristanc, B. Božič, G. Gomišček, The role of sterols in the lipid vesicle response induced by the pore-forming agent nystatin. *Biochimica et Biophysica Acta (BBA) - Biomembranes* **1838**, 2635-2645 (2014).

143. M. Mally, J. Majhenc, S. Svetina, B. Žekš, Mechanisms of Equinatoxin II-Induced Transport through the Membrane of a Giant Phospholipid Vesicle. *Biophysical Journal* **83**, 944-953 (2002).

144. M. Zasloff, Antimicrobial peptides of multicellular organisms. *Nature* **415**, 389-395 (2002).

145. A. S. Ladokhin, M. E. Selsted, S. H. White, Sizing membrane pores in lipid vesicles by leakage of co-encapsulated markers: pore formation by melittin. *Biophysical Journal* **72**, 1762-1766 (1997).

146. K. He, S. J. Ludtke, W. T. Heller, H. W. Huang, Mechanism of alamethicin insertion into lipid bilayers. *Biophysical Journal* **71**, 2669-2679 (1996).

147. S. J. Ludtke *et al.*, Membrane Pores Induced by Magainin. *Biochemistry* **35**, 13723-13728 (1996).

148. M.-T. Lee, T.-L. Sun, W.-C. Hung, H. W. Huang, Process of inducing pores in membranes by melittin. *Proc. Natl. Acad. Sci. U.S.A.* **110**, 14243-14248 (2013).

149. W. C. Wimley, Describing the Mechanism of Antimicrobial Peptide Action with the Interfacial Activity Model. *Acs Chemical Biology* **5**, 905-917 (2010).

150. K. A. Brogden, Antimicrobial peptides: pore formers or metabolic inhibitors in bacteria? *Nature Reviews Microbiology* **3**, 238-250 (2005).

151. K. Matsuzaki, O. Murase, N. Fujii, K. Miyajima, An Antimicrobial Peptide, Magainin 2, Induced Rapid Flip-Flop of Phospholipids Coupled with Pore Formation and Peptide Translocation. *Biochemistry* **35**, 11361-11368 (1996).

152. T. E. Cleveland IV *et al.*, Small-angle X-ray and neutron scattering demonstrates that cell-free expression produces properly formed disc-shaped nanolipoprotein particles. *Protein science* **27**, 780-789 (2018).

153. M. A. Coleman *et al.*, Expression and association of the Yersinia pestis translocon proteins, YopB and YopD, are facilitated by nanolipoprotein particles. *PloS one* **11**, e0150166 (2016).

154. A. T. Dang, W. He, D. B. Ivey, M. A. Coleman, T. L. Kuhl, Lipid and Protein Transfer between Nanolipoprotein Particles and Supported Lipid Bilayers. *Langmuir* **35**, 12071-12078 (2019).

155. B. Deryagin, Y. V. Gutop, Theory of the breakdown (rupture) of free films. *Kolloidn. Zh* **24**, 374 (1962).

156. C. Taupin, M. Dvolaitzky, C. Sauterey, Osmotic pressure-induced pores in phospholipid vesicles. *Biochemistry* **14**, 4771-4775 (1975).

157. E. Karatekin *et al.*, Cascades of Transient Pores in Giant Vesicles: Line Tension and Transport. *Biophysical Journal* **84**, 1734-1749 (2003).

158. C. Faure *et al.*, Modeling leakage kinetics from multilamellar vesicles for membrane permeability determination: Application to glucose. *Biophysical Journal* **91**, 4340-4349 (2006).

159. M. Fukuda *et al.*, Spontaneous reconstitution of discoidal HDL from sphingomyelin-containing model membranes by apolipoprotein A-I. *Journal of Lipid Research* **48**, 882-889 (2007).

160. Y. Liu, J. Agudo-Canalejo, A. Grafmüller, R. Dimova, R. Lipowsky, Patterns of Flexible Nanotubes Formed by Liquid-Ordered and Liquid-Disordered Membranes. *ACS Nano* **10**, 463-474 (2016).

161. M. A. Zhukovsky, A. Filograna, A. Luini, D. Corda, C. Valente, Protein amphipathic helix insertion: A mechanism to induce membrane fission. *Frontiers in cell and developmental biology* **7**, 291 (2019).

162. K. V. Pinigin, T. R. Galimzyanov, S. A. Akimov, Amphipathic peptides impede lipid domain fusion in phase-separated membranes. *Membranes* **11**, 797 (2021).

163. D. Marsh, Cholesterol-induced fluid membrane domains: A compendium of lipid-raft ternary phase diagrams. *Biochimica et Biophysica Acta (BBA) - Biomembranes* **1788**, 2114-2123 (2009).

164. J. Petrlova *et al.*, A differential association of Apolipoprotein E isoforms with the amyloid-beta oligomer in solution. *Proteins* **79**, 402-416 (2011).

165. J. F. Hess, J. C. Voss, P. G. FitzGerald, Real-time observation of coiled-coil domains and subunit assembly in intermediate filaments. *J Biol Chem* **277**, 35516-35522 (2002).

166. T. U. Consortium, UniProt: a worldwide hub of protein knowledge. *Nucleic Acids Research* **47**, D506-D515 (2018).

167. L. R. Kjølbye *et al.*, General Protocol for Constructing Molecular Models of Nanodiscs. *Journal of Chemical Information and Modeling* **61**, 2869-2883 (2021).

168. P. C. Kroon *et al.*, Martinize2 and Vermouth: Unified Framework for Topology Generation. *arXiv* **2212.01191v3**, (2024).

169. D. H. de Jong *et al.*, Improved Parameters for the Martini Coarse-Grained Protein Force Field. *Journal of Chemical Theory and Computation* **9**, 687-697 (2013).

170. T. A. Wassenaar, H. I. Ingólfsson, R. A. Böckmann, D. P. Tieleman, S. J. Marrink, Computational Lipidomics with insane: A Versatile Tool for Generating Custom Membranes for Molecular Simulations. *Journal of Chemical Theory and Computation* **11**, 2144-2155 (2015).

171. H. I. Ingólfsson *et al.*, Capturing Biologically Complex Tissue-Specific Membranes at Different Levels of Compositional Complexity. *J. Phys. Chem. B* **124**, 7819-7829 (2020).

172. T. N. Ozturk *et al.*, in *Methods in Enzymology*. (Academic Press, 2024).

173. G. Bussi, D. Donadio, M. Parrinello, Canonical sampling through velocity rescaling. *The Journal of Chemical Physics* **126**, (2007).

174. M. Bernetti, G. Bussi, Pressure control using stochastic cell rescaling. *The Journal of Chemical Physics* **153**, (2020).

175. S. Thallmair, M. Javanainen, B. Fábián, H. Martinez-Seara, S. J. Marrink, Nonconverged Constraints Cause Artificial Temperature Gradients in Lipid Bilayer Simulations. *J. Phys. Chem. B* **125**, 9537-9546 (2021).

176. H. Kim, B. Fábián, G. Hummer, Neighbor List Artifacts in Molecular Dynamics Simulations. *Journal of Chemical Theory and Computation* **19**, 8919-8929 (2023).

177. D. Van Der Spoel *et al.*, GROMACS: Fast, flexible, and free. *Journal of Computational Chemistry* **26**, 1701-1718 (2005).

178. G. Fiorin *et al.*, Expanded Functionality and Portability for the Colvars Library. *J. Phys. Chem. B* **128**, 11108-11123 (2024).

179. W. Humphrey, A. Dalke, K. Schulten, VMD: Visual molecular dynamics. *Journal of Molecular Graphics* **14**, 33-38 (1996).

180. D. Nečas, P. Klapetek, Gwyddion: an open-source software for SPM data analysis. *Open Physics* **10**, 181-188 (2012).

181. J. H. Lorent *et al.*, Plasma membranes are asymmetric in lipid unsaturation, packing and protein shape. *Nat Chem Biol* **16**, 644-652 (2020).

182. G. C. Roberts, A. Watts, E. B. S. Association, *Encyclopedia of biophysics*. (Springer Berlin Heidelberg, 2013).

183. Q. Lin, E. London, The influence of natural lipid asymmetry upon the conformation of a membrane-inserted protein (perfringolysin O). *Journal of Biological Chemistry* **289**, 5467-5478 (2014).

184. M. Chopra, D. Schrenk, Dioxin toxicity, aryl hydrocarbon receptor signaling, and apoptosis—Persistent pollutants affect programmed cell death. *Critical reviews in toxicology* **41**, 292-320 (2011).

185. J. L. Watson *et al.*, De novo design of protein structure and function with RFdiffusion. *Nature* **620**, 1089-1100 (2023).

186. J. Jumper, D. Hassabis, Protein structure predictions to atomic accuracy with AlphaFold. *Nature methods* **19**, 11-12 (2022).

187. A. K. Shukla *et al.*, Structure of active β-arrestin-1 bound to a G-protein-coupled receptor phosphopeptide. *Nature* **497**, 137-141 (2013).

188. J. Deisenhofer, W. Steigemann, Crystallographic refinement of the structure of bovine pancreatic trypsin inhibitor at l. 5 Å resolution. *Structural Science* **31**, 238-250 (1975).

189. K. Wüthrich, The way to NMR structures of proteins. *Nature structural biology* **8**, 923-925 (2001).

190. M. Wilchek, E. A. Bayer, The avidin-biotin complex in immunology. *Immunology today* **5**, 39-43 (1984).

191. B. W. Rickeard *et al.*, Transverse lipid organization dictates bending fluctuations in model plasma membranes. *Nanoscale* **12**, 1438-1447 (2020).

192. F. A. Heberle *et al.*, Subnanometer structure of an asymmetric model membrane: interleaflet coupling influences domain properties. *Langmuir* **32**, 5195-5200 (2016).

193. B. Li, E. London, Preparation and drug entrapment properties of asymmetric liposomes containing cationic and anionic lipids. *Langmuir* **36**, 12521-12531 (2020).

194. L. Pan, J. P. Segrest, Computational studies of plasma lipoprotein lipids. *Biochimica et Biophysica Acta (BBA) - Biomembranes* **1858**, 2401-2420 (2016).